

**INVESTIGATING TROPICAL CYCLONE CLOUDS,
THERMODYNAMICS AND DYNAMICS VIA NOVEL
REMOTE SENSING AND MODELING TECHNIQUES**

by

Ethan Murray

B.A., Vassar College, 2021

M.S., University of Colorado Boulder, 2023

A thesis submitted to the

Faculty of the Graduate School of the

University of Colorado in partial fulfillment

of the requirements for the degree of

Doctor of Philosophy

Department of Atmospheric and Oceanic Sciences

2025

Committee Members:

Zhien Wang, Co-Chair

Kris Karnauskas, Co-Chair

Dr. Gijs de Boer

Dr. Andrew Winters

Dr. Jun Zhang

Murray, Ethan (Ph.D., Atmospheric and Oceanic Sciences)

INVESTIGATING TROPICAL CYCLONE CLOUDS, THERMODYNAMICS AND DYNAMICS
VIA NOVEL REMOTE SENSING AND MODELING TECHNIQUES

Thesis directed by Dr. Kris Karnauskas and Dr. Zhien Wang

Abstract

Tropical cyclones (TCs) are among the most damaging weather disasters to impact the United States. To mitigate the impacts of these storms, improving forecasts of TC sustained wind speed, rainfall rate, and structural characteristics, including cloud distributions, is of the upmost importance. To do so, this thesis analyzes multiple TC observational datasets to better understand storm structure, and it develops a framework to verify model forecasts using these measurements. This work uses traditional aircraft observations and data from the Compact Raman Lidar (CRL), a novel remote sensing instrument deployed on the NOAA P-3 aircraft.

First, we explore the convective nature of clouds in the TC eye, as the CRL is the first instrument to consistently resolve these features. Statistics reveal a diversity of eye cloud structures and enhanced low level vertical mixing, providing a pathway towards TC intensity change. Next, the properties of convection, shallow clouds, and stratiform precipitation in the TC rainbands are explored using CRL observations. Here, we characterize convective cloud region widths for the first time, find that active convection has different properties than stratiform rain and clear air regions, and that TC asymmetries generated by environmental shear influence rainband properties. Finally, using a new model evaluation framework, aircraft observations are compared to individual forecasts of TC Sam (2021), identifying impactful biases in the model's horizontal temperature gradient and boundary layer moisture. This thesis fills important gaps in our understanding of TC clouds, thermodynamics, and dynamics, and it opens new avenues towards TC model improvement.

Dedication

To Susan Murray, my mom, who sparked my joy for science and supported me at every step.

Acknowledgements

I am very grateful for the friendship and mentorship I received throughout my graduate studies. None of this would have been possible without the support of the colleagues, peers, friends and family listed below:

- I greatly appreciate the support from my co-advisor Zhien Wang, especially over the past few months as my dissertation began to take shape. You fostered my scientific curiosity and helped guide my research projects towards polished final states. I am also grateful for the trust you had in me during the TORUS Field Campaign in Summer 2022 and the MAGPIE Field Campaign in Summer 2023. Thank you for helping me grow as a scientist and person.
- I deeply value the mentorship I received from my co-advisor Kris Karnauskas. You guided my thinking and greatly improved my scientific communication over the past two years. Your open door policy was very welcoming, and I appreciate the strong community you built through your research group.
- I am grateful for the support of my exceptional committee members: Gijs de Boer, Andrew Winters, and Jun Zhang. Our collaboration always opened up new research avenues, changed my mind, and improved my work.
- I am thankful for the help from my collaborators at the Naval Research Laboratory, especially from my NREIP advisor Jon Moskaitis during Summer 2024. I would not have been able to complete my PhD without your guidance on my third research project.

- I deeply value all the friendships I made during my time in ATOC. You had my back during the silly times and the serious ones, making me excited to go to the office every day. I'm so glad that such a supportive community exists here. Finishing my PhD would not have been possible without all of you!
- I would like to thank my undergraduate advisor Brian Daly at Vassar College, who first introduced me to research through the URSI Summer Program and strived to continue our collaboration through the COVID-19 pandemic. I would also like to thank Kirsten Menking at Vassar College for introducing me to the intersection of earth science, computer science, and physics, inspiring me to pursue my PhD research.
- Finally, I am grateful for having such an incredible family. My mom, cousins, aunts, and uncles have all been so supportive during my graduate studies. While I've been further from home and can't see you all as frequently, you're always in my heart.

Contents

Chapter

1	Introduction	1
1.1	Tropical Cyclones: Overview and Hazards	1
1.2	Tropical Cyclone Structure	1
1.2.1	Overview	1
1.2.2	TC Eye	4
1.2.3	TC Rainbands	5
1.3	Methods of Understanding Tropical Cyclones	5
1.3.1	TC Models	5
1.3.2	Satellites	6
1.3.3	Aircraft Observations	7
1.3.4	The Compact Raman Lidar	9
1.4	Dissertation Outline	10
2	CLOUD HEIGHT DISTRIBUTIONS AND THE ROLE OF VERTICAL MIXING IN THE TROPICAL CYCLONE EYE DERIVED FROM COMPACT RAMAN LIDAR OBSERVATIONS	11
2.1	Introduction	12
2.2	Methods	14
2.3	Results	18

2.3.1	Hurricane Sam Case Study	18
2.3.2	Statistical Analysis Results from All Cases	21
2.4	Conclusions	25
2.5	Acknowledgments	27
2.6	Open Research	27
3	NOVEL OBSERVATIONS OF CONVECTIVE-SCALE CLOUD AND PRECIPITATION DISTRIBUTIONS IN THE TROPICAL CYCLONE RAINBANDS	28
3.1	Introduction	29
3.2	Methods	32
3.2.1	Observational Datasets	32
3.2.2	Classifying CRL Backscattered Power	34
3.2.3	Analysis Methods	35
3.2.4	Cases Sampled by the CRL	36
3.3	Case Study	39
3.3.1	TC Sam (2021) Rainbands: Plan View	39
3.3.2	TC Sam (2021) Rainbands: Profile View	40
3.3.3	TC Sam (2021) Rainbands: Cloud and Rainfall Classifications	40
3.4	Rainband Cloud, Rainfall, and Kinematic Properties	43
3.4.1	Flight Level Vertical Motion Differences by CRL Classification	43
3.4.2	Surface SFMR Rainfall Differences by CRL Classification	43
3.4.3	TDR Differences by CRL Classification	44
3.4.4	CRL Cloud Classification Statistics	46
3.5	TC Rainband Asymmetries	50
3.5.1	Differences between Flight Legs	50
3.5.2	Differences by Distance from the TC Center	52
3.5.3	Kinematic Drivers of Rainband Asymmetries	54

3.5.4	Rainband Asymmetries: Example Flight Legs	57
3.6	Conclusion	60
4	AN OBSERVATION-MODEL COMPARISON FRAMEWORK FOR DIAGNOSING TROPICAL CYCLONE THERMODYNAMIC CHANGE: APPLICATION TO HURRICANE SAM (2021)	62
4.1	Introduction	63
4.2	Datasets	67
4.2.1	COAMPS-TC Model Configuration	67
4.2.2	Compact Raman Lidar (CRL)	68
4.2.3	Tail Doppler Radar (TDR)	69
4.2.4	Dropsondes	70
4.2.5	Comparison of Thermodynamic Data Coverage	70
4.3	Analysis Methods	73
4.3.1	CRL Bias Correction	73
4.3.2	Observation and Model Matching Techniques	75
4.3.3	Single Day Compositing Methods	76
4.4	Case Study: Hurricane Sam	76
4.5	Results	78
4.5.1	Kinematic Variability	78
4.5.2	Thermodynamic Vertical Profiles	84
4.5.3	Thermodynamic 2D Composites	86
4.5.4	Kinematic and Thermodynamic Asymmetries	91
4.6	Conclusions	94
5	CONCLUSIONS AND FUTURE WORK	99
5.1	Conclusions	99
5.2	Future Work	101

Bibliography	104
---------------------	------------

Appendix

A SUPPLEMENTAL INFORMATION FOR CHAPTER 2	138
B SUPPLEMENTAL INFORMATION FOR CHAPTER 3	142

Tables**Table**

A.1	Table of P-3 Flights Used for Eye Cloud Analysis	141
B.1	Table of P-3 Flights Used for Rainband Cloud Analysis	143

Figures

Figure

1.1	Conceptual Diagram of an Intense TC's Cloud Structure	3
2.1	TC Eye Clouds: Example Cross Section	16
2.2	TC Sam: Eye Cloud Case Study	19
2.3	Distributions of Eye Cloud Height and w	22
2.4	Eye Cloud Statistics Across Horizontal Scales	24
3.1	CRL Flight Leg Vortex and Environmental Properties	38
3.2	TC Sam: Rainband Cloud Case Study	42
3.3	Distributions of In Situ w and SFMR Rain Rate	44
3.4	Distributions of TDR w and Reflectivity	46
3.5	Rainband Cloud Width, Spacing, and Height Statistics	49
3.6	Rainband Cloud Statistics by Shear Quadrant	52
3.7	Rainband Cloud Statistics by Shear Quadrant and Radial Distance	54
3.8	Shear Quadrant Differences in TDR Wind and Reflectivity Composites	56
3.9	Example TC Sam Flight Legs from Each Shear Quadrant	59
4.1	TC Sam: CRL, Dropsonde, and COAMPS-TC Cross Sections	72
4.2	Comparison of CRL and Dropsonde Thermodynamic Profile Statistics	75
4.3	TC Sam: Track and Intensity Errors	78
4.4	TDR Tangential Wind Speed Composite Plots	80

4.5	TDR Radial Wind Speed Composite Plots	82
4.6	TDR Vertical Wind Speed Composite Plots	83
4.7	Vertical Profiles of CRL θ	85
4.8	Vertical Profiles of CRL Moisture	86
4.9	Radius-Height Composite Plots of θ	87
4.10	Radius-Height Composite Plots of Moisture	89
4.11	Radius-Height Composite Plots of θ_e	91
4.12	Low-Level Moisture Asymmetries	93
4.13	Low-Level Radial Wind Asymmetries	94
A.1	TC Sustained Wind Speeds for Eye Cloud Statistics	138
A.2	Flight Paths used for TC Eye Cloud Analysis	139
A.3	Eye Cloud Heights: Error Analysis	140
B.1	Distributions of TDR W and Reflectivity, Rainfall Regions Only	142

Chapter 1

Introduction

1.1 Tropical Cyclones: Overview and Hazards

Due to their strong winds, heavy rainfall, and storm surge, tropical cyclones (TCs) are the most economically impactful weather disasters to affect North America, East Asia, and other regions [Dinan, 2017, Geiger et al., 2016, Hu et al., 2023, Iglesias et al., 2021, Klotzbach et al., 2018, 2022, Mendelsohn et al., 2012, Muller et al., 2025, Pielke and Landsea, 1998]. Enhanced winds, strongest in the TC eyewall and rainbands, cause extensive damage during TC landfall [Aberson et al., 2006b, Wakimoto and Black, 1994, Wurman and Kosiba, 2018]. TC storm surge inundates typically dry areas along the US Atlantic and Gulf coasts, and intense rainfall during and after landfall produces significant freshwater flooding [Adams et al., 2024, Bilskie and Luettich Jr., 2024, Gori et al., 2023, Needham et al., 2015, Tonn and Czajkowski, 2022, Wahl et al., 2015]. The combined effects of wind, rainfall, and storm surge can damage critical infrastructure, disrupt the economy, and negatively impact health outcomes among affected populations [Anderson et al., 2020, Chang, 2016, Rappaport, 2014, Worsnop et al., 2017, Young and Hsiang, 2024]. Recent increases in vulnerable coastal populations, TC intensification rates, rainfall totals, and storm surge along the US Atlantic and Gulf coasts have created heightened interest in understanding the processes driving these impacts [Balaguru et al., 2023, 2022, Gori et al., 2022, Little et al., 2015, Ting et al., 2019, Yin, 2023]. To best prepare for TC impacts, a thorough understanding of their structure is required.

1.2 Tropical Cyclone Structure

1.2.1 Overview

TCs are cyclonically rotating low pressure systems that generate some of the strongest sustained wind speeds on Earth [Cione et al., 2020]. After forming in the tropics through a cyclogenesis process that involves local and synoptic influences [Houze, 2010], TCs strengthen and migrate polewards [Emanuel, 2018a]. TCs strengthen through enthalpy fluxes from the warm sea surface into the atmosphere [Emanuel, 1995]. This generates deep convection and a secondary circulation essential to intensity maintenance [Emanuel, 1986]. TC secondary circulation involves an inflow branch at low-levels, rising motion through rainband and eyewall convection, an outflow branch at upper levels, and subsidence in the outer environment. Sea surface enthalpy fluxes and TC secondary circulation combine to fuel deep convection, heavy rainfall, and dangerous winds. [Houze, 2010]

Intense TCs are typically composed of five distinct regions: the eye, eyewall, inner core rainbands, distant rainbands, and environment (Figure 1.1). These regions are described radially outward from the TC center in the following paragraphs. The TC eye is a region of relatively calm tangential winds, a strong temperature inversion, and clear air aloft [Houze, 2010, Jordan, 1961, Willoughby, 1998]. No moderate or intense rainfall sectors are shown for the TC eye in the conceptual diagram, as relatively few deep convective cells and no stratiform regions exist here [Hirano et al., 2022, Kossin and Schubert, 2004, Schubert et al., 2007b].

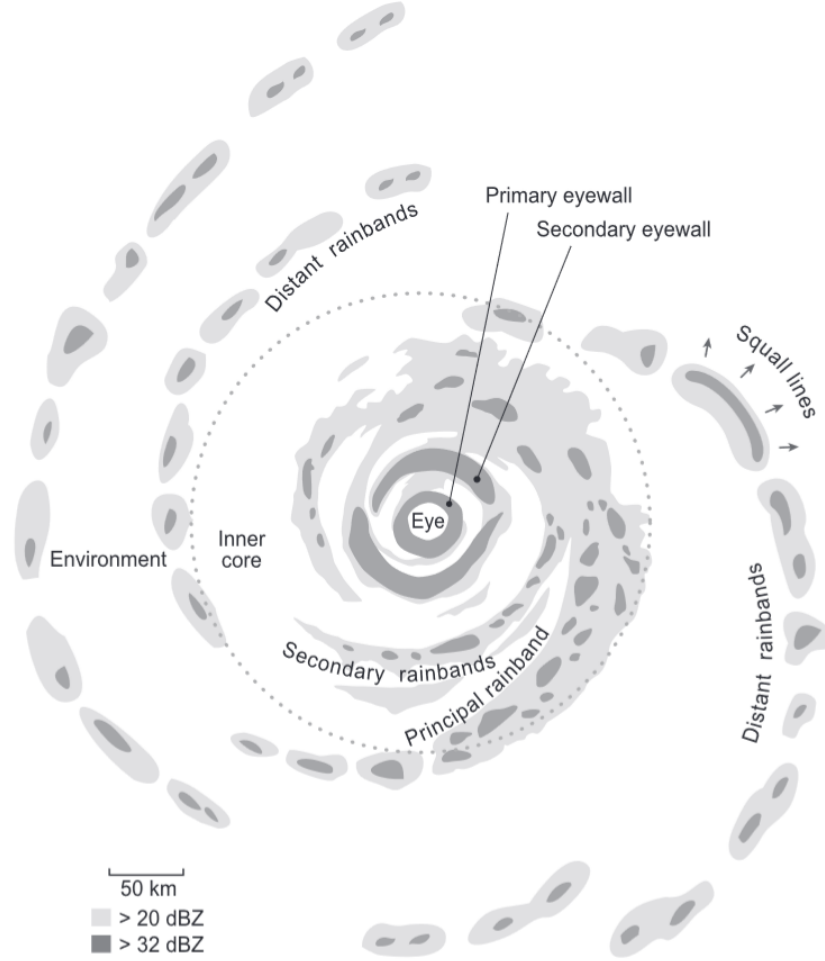


Figure 1.1: Plan view of the rainfall structures commonly found in an intense North Atlantic tropical cyclone. Regions of moderate (light grey) and strong (dark grey) precipitation are visualized using typical radar reflectivity return values. Adapted from Houze [2010].

The TC eyewall, in contrast, exists just outside of the eye, contains the largest rainfall rates, deepest convection, and strongest tangential winds [Aberson et al., 2006a, Barnes and Barnes, 2014, Emanuel, 2018a, Fischer et al., 2020, Marks et al., 2008, Shimada et al., 2024]. The eyewall cloud of an intense TC slopes radially outwards and is associated with strong upwards motion and outflow [Hazelton et al., 2015, Rogers et al., 2012]. Most often, only one eyewall exists at a time in an intense TC, but secondary eyewalls regularly occur and can replace the primary eyewall [Didlake et al., 2017, 2018, Houze et al., 2007, Sitkowski et al., 2011], as shown in the conceptual figure.

Outside of the eyewall, a variety of TC rainband structures are encountered. The rainbands

are composed of both convective and stratiform precipitation, often form distinct complexes like principal and secondary rainbands, and have unique dynamic properties [Barron et al., 2022, Didlake and Houze, 2009, 2013b, Houze, 2010]. The inner core rainbands differ greatly from the outer core rainbands, as they experience different effects from the TC vortex and the outer environment [Bogner et al., 2000, Dai et al., 2022, Tang et al., 2018, Yu et al., 2018].

Finally, the TC environment plays a critical role in vortex development and maintenance, either positively or negatively impacting inner core convective development [Chen et al., 2021b, Fischer et al., 2019, Hendricks et al., 2010, Hill and Lackmann, 2009, Kaplan and DeMaria, 2003, Kaplan et al., 2010, Majumdar et al., 2023b, Mercer et al., 2021, Rios-Berrios et al., 2024, Wadler et al., 2022, 2023b]. The TC eye and rainbands are described in detail below, as these regions are the focus of this dissertation.

1.2.2 TC Eye

The TC eye is a region of calm winds, shallower clouds, and enhanced subsidence that forms at the center of intense TCs [Emanuel, 2018a, Houze, 2010, Willoughby, 1998]. TC eyes form in slightly more than half of all storms, take about 36h to develop, and they usually form soon after reaching tropical storm strength [Knapp et al., 2018, Vigh et al., 2012]. Different eye formation mechanisms are proposed [Chen and Wu, 2022, Schubert et al., 2007b, Vigh and Schubert, 2009], and TC eyes range in size from around 10 km to 100 km [Barnes and Barnes, 2014, Knapp et al., 2018]. TC intensity, intensification rate, and if the TC has undergone an eyewall replacement cycle all influence the size of the eye [Barnes and Barnes, 2014, Chen and Wu, 2025, Houze et al., 2007, Kossin et al., 2007, Wadler et al., 2018a].

The TC eye contains a strong temperature inversion around 500-850 hPa; this inversion divides the typically hot, drier upper eye from the warm, moist lower eye [Halverson et al., 2006, Houze, 2010, Willoughby, 1998]. This inversion creates the eye's distinct cloud and dynamic properties. The eye is typically filled with clear air or shallow stratocumulus clouds just below the inversion height [Willoughby, 1998]. Taller hub clouds at the TC center surrounded by moats of

clear air occasionally form due to enhanced subsidence along the eye-eyewall interface [Barnes and Fuentes, 2010, Jordan, 1961, Schubert et al., 2007b, Simpson and Starrett, 1955]. Other structures, such as eye-eyewall mesovortices and deep clouds, can generate significantly more vertical and horizontal mixing, locally changing the thermodynamic properties of the eye [Aberson et al., 2006a, Fletcher et al., 1961, Hirano et al., 2022, Kossin and Eastin, 2001, Kossin and Schubert, 2004].

The effect of the TC eye on the eyewall and storm intensity is debated. Model trajectory analysis reveals that while air mixes between the eye and the eyewall at most heights [Cram et al., 2007, Hioki and Tsuboki, 2021], this mixing has been found to be minor and doesn't impact TC intensity [Bryan and Rotunno, 2009, Zhou et al., 2020]. Nevertheless, the lower eye is a potentially large source of high θ_e air that can fuel deep convective bursts, enhancing TC intensification [Barnes and Fuentes, 2010, Braun, 2002, Eastin et al., 2005, Guimond et al., 2016, Hazelton et al., 2017, Persing and Montgomery, 2003]. Other eye-eyewall interactions are theorized to impact TC intensification rates through enhanced inner eyewall convection [Wang and Heng, 2016] or turbulent diffusion of radial momentum along the eye-eyewall interface [Emanuel, 1997]. Novel observations of TC eye clouds and thermodynamics are presented in Chapter 2. They add context to this debate and update our understanding of this often overlooked TC region.

1.2.3 TC Rainbands

The TC rainbands, which form outside the eyewall, often contain a principal rainband, secondary rainbands, and distant rainbands [Houze, 2010]. The principal rainband is radially closest to the TC center and has distinct structural asymmetries [Barnes et al., 1983, Willoughby et al., 1984]. A wavenumber-1 asymmetry in the principal rainband is generated by the environmental shear vector. It usually leads to convective development in the downshear right quadrant of the TC, convective maturity downshear left, a transition from convection to stratiform precipitation upshear left, and sparse convection upshear right [Barron et al., 2022, Chen et al., 2021b, Corbosiero and Molinari, 2003, Didlake and Houze, 2013b, Hence and Houze, 2012, Rogers et al., 2003, Wingo and Cecil, 2010]. These rainband cloud asymmetries are correlated to tangential wind [Didlake and

Houze, 2009, Gu et al., 2016, Rogers et al., 2015, Zhang et al., 2013] and thermodynamic asymmetries [Chen et al., 2021b, Zhang et al., 2013]. All of these factors can impact eyewall structure and vortex strength.

Secondary rainbands are smaller precipitation features that form within the TC inner core. These bands propagate radially outwards as vortex Rossby waves [Corbosiero et al., 2006, Montgomery and Kallenbach, 1997]. Secondary rainbands impact TC intensity by cutting off the inward advection of high θ_e air towards the TC center, which can lead to an eyewall replacement cycle [Didlake et al., 2018, Houze et al., 2007, Powell, 1990, Sitkowski et al., 2011]. The distant TC rainbands are located in the TC outer core (or environment), have a more limited radial extent, and tend to display squall-line properties like strong convective cells, a low-level cold pool, and enhanced total CAPE [Bogner et al., 2000, Yu et al., 2018, 2019]. A more thorough literature review on the TC rainbands, along with novel CRL rainband observations, is found in Chapter 3 of this dissertation.

1.3 Methods of Understanding Tropical Cyclones

1.3.1 TC Models

High resolution TC observations and models synergize to create the best depictions of the TC features discussed above. Observations are used to explore theorized processes and validate model output, while dynamical models can provide dynamic, thermodynamic, and microphysical fields with spatial and temporal coverages impossible to observe. Therefore, with a properly constrained TC model, significant advances towards understanding TC intensity, intensity change, and structure can be made [Cangialosi et al., 2020, DeMaria et al., 2021].

A variety of model types are used operationally and for research to better understand TCs. Statistical models use combinations of TC climatological factors to predict current storm track, intensity, and rapid intensification likelihood [DeMaria et al., 2021, 2022, Kaplan et al., 2010], while dynamical models fully simulate the TCs 3D wind, thermodynamic, and microphysics fields

to predict TC impacts [Wang et al., 2023b]. As a result of finer model resolution, improved vortex initialization and parameterization schemes, and increased observational data assimilation, dynamic models have recently seen a large improvement in TC track, intensity, and structural predictions [Alaka et al., 2024, Cangialosi et al., 2020, DeMaria et al., 2021, Heming et al., 2019, Wang et al., 2023a, 2024, Zhang et al., 2015, 2020]. Dynamic model ensembles help elucidate model spread and provide probabilistic intensification statistics [Komaromi et al., 2021, Zhang et al., 2014, 2023]. A simple or weighted average of statistical and dynamic model outputs is often used operationally in consensus models, providing the most skillful track and intensity predictions possible [Zhang et al., 2023]. Machine learning TC models, many of which provide statistical guidance [Boussioux et al., 2022, Griffin et al., 2022, Kim et al., 2024a], speed up a parameterization scheme (such as an atmospheric boundary layer parameterization scheme) in a dynamical model [Wang and Tan, 2023], or improve the pre-processing of TC observations [DesRosiers and Bell, 2024], have become increasingly popular in the research community and can outperform traditional forecasts in some cases [Kim et al., 2024b, Liu et al., 2023, Su et al., 2020, Wang et al., 2022]. Yet, it is challenging to transition these novel machine learning models to operations, and few are currently considered in operational settings [DeMaria et al., 2022, Wang et al., 2023b].

1.3.2 Satellites

Satellites are a useful tool for observationally characterizing TC properties, especially for regions not typically sampled by aircraft reconnaissance [Kidder and Haar, 1995, Ricciardulli et al., 2023]. Depending on the type of satellite used, they provide refreshed views of the TC on the order of minutes to days. Geostationary satellites like GOES and Himawari 8 provide consistent temporal and spatial coverage of the Atlantic and Pacific Oceans, but their infrared channels cannot see past the deep cloud tops that often characterize TC inner cores and obscure the low-level cloud structure [Fischer et al., 2018, Knapp et al., 2011, 2018]. Nevertheless, TC intensity can be estimated from infrared satellite images using algorithmic methods like the Dvorak technique [Dvorak, 1975, Liu et al., 2019, Mueller et al., 2006, Pineros et al., 2008] or through machine learning

methods [Lee et al., 2021, May et al., 2024, Tong et al., 2023, Zhang et al., 2024]. Meanwhile, microwave satellite data have less frequent refresh rates and often only sample sections of the TC [Fischer et al., 2018], but they can peer through overshooting tops to reveal lower-level features. For instance, climatologies based on microwave data have revealed properties of TC rainfall [Lavender and McBride, 2021, Lonfat et al., 2004, Tao et al., 2017, Yang et al., 2020], wind and cloud structure [Jiang et al., 2019, Knapp et al., 2018], moisture, and warm core height [Blackwell et al., 2018, Wang and Jiang, 2019, Yang et al., 2023]. Finally, synthetic aperture radars remotely sense TC surface winds at the highest spatial resolution possible and can peer through the dense clouds that typically block infrared retrievals, but they also have temporally limited overpasses and suffer from signal interference from rainfall [Combot et al., 2020, Ikuta and Shimada, 2024, Li, 2017, Zhang et al., 2024, Zhang and Perrie, 2024]

1.3.3 Aircraft Observations

While satellite data greatly enhance our understanding of TC structure, aircraft observations fill impactful knowledge gaps. In particular, aircraft data provide high resolution sampling of TCs on convective and vortex scales [Rogers, 2021]. These observations are at spatial and temporal scales unattainable using reanalysis or satellite data, and they allow for the improvement of model forecasts through direct data assimilation [Aberson et al., 2015, Aksoy et al., 2012, Christophersen et al., 2022, Ditchek et al., 2023, Sippel et al., 2022] and modifying model parameterizations [Gopalakrishnan et al., 2021, Zhang et al., 2012]. TC aircraft reconnaissance in the North Atlantic is mainly conducted by the Air Force and NOAA [Holbach et al., 2023, Zawislak et al., 2022]. The U.S. Air Force conducts hurricane reconnaissance with their WC-130J aircraft and collects dropsonde and stepped frequency microwave radiometer (SFMR) data along the flight track. NOAA uses the G IV aircraft for TC synoptic surveillance primarily through upper level dropsondes [Aberson, 2010, Ryan et al., 2019, Sippel et al., 2024], while the two NOAA P-3 aircraft penetrate the TC inner core and collect radar, dropsonde, in situ, SFMR, and other operational and research data depending on the payloads aboard the aircraft [Kossin and Eastin, 2001, Martinez et al., 2017,

Rogers et al., 2013a, Zhang et al., 2013].

Dropsondes are small payloads that are launched from reconnaissance aircraft and transmit wind and thermodynamic data back to the aircraft, with their fall to the sea surface slowed via parachute [Hock and Franklin, 1999]. Dropsondes are a trusted measurement technique, contributing to about 400 research papers since their operational introduction in 1997 [Aberson et al., 2023]. The NOAA G IV and P-3 aircraft both utilize dropsondes to sample TC properties, with the G IV sampling nearly the entire troposphere and the P-3 usually sampling the lowest 3 km of the storm. Improvements to TC forecasts have been made by directly assimilating dropsonde data into models [Christophersen et al., 2017, Ditchek and Sippel, 2023, Ditchek et al., 2023, Piper and Torn, 2025]. Dropsondes are also an invaluable research tool, illuminating TC properties and asymmetries through case studies [Bell and Montgomery, 2008, Tang et al., 2024, Zawislak et al., 2016] and composite analysis [Ahern et al., 2019, Kopelman et al., 2024, Wadler et al., 2022, Zawislak and Zipser, 2014, Zhang et al., 2013]. Observational limitations exist for dropsondes, however. They can only sample single atmospheric columns, which creates gaps in data coverage, particularly in the TC rainbands [Carstens and Wing, 2022, Ditchek and Sippel, 2023, Rogers et al., 2015, Stern and Bryan, 2018]. They can also be advected cyclonically by the strong TC winds as they fall to the surface, unintentionally sampling different regions of the storm [Aberson et al., 2017, Nguyen et al., 2019].

In situ thermodynamic and dynamic data are collected by sensors placed directly on reconnaissance aircraft and unmanned aircraft systems (UASs) [Holbach et al., 2023]. As for dropsondes, assimilating in situ data into TC models is a proven technique to enhance track and intensity forecasts [Aksoy et al., 2022, Sellwood et al., 2023, Weng and Zhang, 2016]. Due to their high resolution, in situ aircraft data are an excellent method for studying convective scale TC processes [Bell and Montgomery, 2008, Kossin and Eastin, 2001, Martinez et al., 2017]. In situ data have similar limitations as dropsondes; since data are only collected at flight height, wide swaths of the TC are missed, including data from the atmospheric boundary layer. UASs are able to probe the most extreme TC environments, such as the atmospheric boundary layer and the high wind eye-eyewall

interface [Chen et al., 2021a, Cione et al., 2020, Sellwood et al., 2023], but data coverage from this instrument remains limited.

Radar data heavily contribute to our understanding of TC dynamics and rainfall structure. The Tail Doppler Radar (TDR) instrument is operated on both NOAA P-3s during all operational flights, providing 3D wind and reflectivity fields for assimilation into real-time TC forecasts [Xu et al., 2024, Wang and Pu, 2021, Zhang et al., 2011a] and for research purposes. TDR case studies have historically been the primary avenue for exploring fine scale TC structure [Barnes et al., 1983, Jorgensen, 1984, Rogers and Zhang, 2023]. The TDR also allows for composite studies, elucidating TC axisymmetric and asymmetric differences depending on TC intensity, intensification rate, vortex tilt, and environmental shear [DesRosiers et al., 2023, Fischer et al., 2023, Hazelton et al., 2015, Rogers et al., 2012, Shimada et al., 2024, Zhang et al., 2022a]. Data from other aircraft, satellite, and ground based doppler radars (like the NOAA P-3 lower fuselage radar, the global precipitation measurement mission's dual-frequency precipitation radar, and the weather surveillance radar) have been harnessed to study TC dynamic structure [Barnes and Barnes, 2014, Didlake and Houze, 2009, Guimond et al., 2016, Matyas et al., 2025, Tang et al., 2018, Wang and Pu, 2021]. Benefits of using radar data include 3D coverage of TC winds and reflectivity, remote sampling of dangerous features like intense updrafts, and standardized data resolution [Fischer et al., 2022]. Drawbacks include poor sampling of precipitation free regions, spatial averaging of many radar swaths, and overlooking key surface features [Lorsolo et al., 2010, Rogers et al., 2012].

1.3.4 The Compact Raman Lidar

Now that current TC observing platforms and model configurations have been described, we turn our attention to identifying gaps in our knowledge of TC structure. For this dissertation, we focus on the sparse observations of cloud structure and thermodynamics in the TC eye and rainbands. Most current measurements of the TC eye come from satellites [Knapp et al., 2018, Vigh et al., 2012], from flight in situ measurements [Kossin and Eastin, 2001], or from dropsondes [Barnes and Fuentes, 2010, Hirano et al., 2022, Willoughby, 1998]. While each of these measurements have

benefits and drawbacks, none are able to directly measure the variation in low-level eye clouds. Similarly, while many studies have investigated TC rainband convective and stratiform structure via satellites [Hence and Houze, 2012, Wingo and Cecil, 2010] and radar [Barnes et al., 1983, Barron et al., 2022, Didlake and Houze, 2009], they struggle to differentiate between active, low-level convective clouds and entrained stratiform rainfall, obscuring our view into important rainband features. Filling this knowledge gap would illuminate key TC eye and rainband kinematic and thermodynamic processes that can impact the storm's intensity. Better observing these regions would also allow us to make more detailed observation-model comparisons for individual storms, helping us improve operational TC forecasts.

In this thesis, the compact Raman lidar (CRL) is used to fill these significant knowledge gaps. The CRL is a downwards pointing remote sensing instrument deployed on the NOAA P-3 aircraft. It creates cross sections of low-level backscattered power, temperature, and moisture in non-cloudy regions below the flight track. Due to unique backscatter properties, return signals to the CRL are not attenuated by rainfall, but they are attenuated by clouds. This allows the instrument to differentiate between cloud tops, entrained rainfall from above the aircraft, clear air, and boundary layer aerosols. CRL temperature and moisture returns also provide extensive low-level thermodynamic data, filling measurement gaps between typically sparse dropsondes.

1.4 Dissertation Outline

Chapter 1 of this dissertation summarized the literature and presented an overview of the tools used to investigate TC structure. The next three chapters all use CRL observations along with other methods to gain new insight into particular TC processes. In Chapter 2, the CRL backscattered power channel is used to determine cloud heights in the TC eye, finding that there is greater cloud top variability than previously expected, including from shallow convective cells. In Chapter 3, CRL backscattered power data from the TC rainbands are analyzed, identifying shallow convection and boundary layer clouds for the first time and finding that low-level TC structure is dependent upon environmental shear strength and direction. In Chapter 4, CRL thermodynamic

data and TDR wind observations are compared to COAMPS-TC model output for TC Sam (2021), finding important differences in Sam's simulated low-level thermodynamics. Chapter 5 elucidates how these results provide an updated view of TC cloud and thermodynamic processes, and it suggests avenues for future work.

Chapter 2

CLOUD HEIGHT DISTRIBUTIONS AND THE ROLE OF VERTICAL MIXING IN THE TROPICAL CYCLONE EYE DERIVED FROM COMPACT RAMAN LIDAR OBSERVATIONS

Preface

This chapter is published as cited below:

Ethan J. Murray, Jason Dunion, Kristopher B. Karnauskas, Zhien Wang, and Jun A. Zhang. Cloud height distributions and the role of vertical mixing in the tropical cyclone eye derived from compact raman lidar observations. **Geophysical Research Letters**, 51(14):e2024GL108515, 2024. doi: 10.1029/2024GL108515. URL <https://onlinelibrary.wiley.com/doi/abs/10.1029/2024GL108515>

Abstract

The distribution of tropical cyclone (TC) eye cloud heights is documented for the first time using compact Raman lidar (CRL) measurements with high spatial resolution. These cloud heights act as tracers for low-level vertical mixing in the eye region. Cloud height distributions using all available data from nine Atlantic TCs in 2021 and 2022 show significant vertical variance, dispelling the notion of a flat stratiform eye cloud deck. Eye cloud widths are multiscale, with shallow convective clouds dominating CRL returns. Data from Hurricane Sam (2021) highlight the evolution of shallow convective clouds in the TC eye and their associated temperature inversions. The frequent appearance of convective eye clouds, along with observed vertical wind fluctuations,

suggests that vertical mixing from the boundary layer frequently occurs in the TC eye, even beneath strong inversions. This strong vertical mixing should be accurately portrayed by TC simulations and forecasts.

Plain Language Summary

While the temperature inversion and associated clouds within the tropical cyclone (TC) eye region are essential elements of storm structure, observing eye cloud heights remains a challenge, and the vertical distribution of these clouds is poorly constrained. This study documents TC eye cloud characteristics using a new aircraft-based remote sensing technique for the first time, with a focus on cloud height distributions. Both case study and statistical approaches confirm that most of these clouds are convective in nature, not stratiform. The formation of shallow convective clouds within TC eyes is driven by shallow upward mixing as documented by aircraft flight level vertical wind measurements. Vertical mixing across the eye inversion layer changes inner core thermodynamics, highlights a potential pathway for intensity change, and emphasizes why this process must be captured in high resolution TC forecast models.

Key Points

- New, aircraft-based compact Raman lidar cloud, temperature, and water vapor measurements detail tropical cyclone inner core structure.
- Case studies and statistics demonstrate how shallow convective clouds with high spatial variability are the most common eye cloud type.
- Vertical velocity and cloud height analyses suggest that low level vertical mixing drives shallow convective eye cloud formation.

2.1 Introduction

The increased difficulty in forecasting tropical cyclone (TC) intensity change elevates risks along the US Atlantic and Gulf coasts [Cangialosi et al., 2020, Emanuel, 2017, Klotzbach et al., 2022,

Pielke and Landsea, 1998]. To better forecast and prepare for rapidly intensifying TCs [Kaplan et al., 2010], an improved understanding of multi-scale dynamic and thermodynamic interactions are needed, especially within the TC inner core [Hendricks, 2012, Rogers, 2021, Zawislak et al., 2022]. For instance, enthalpy and momentum exchange near the air-sea interface and turbulent mixing in the boundary layer are key processes for a storm to undergo intensity change [Emanuel, 2012, 2018b, Smith et al., 2017, Zhang and Rogers, 2019, Zhang et al., 2017a].

The TC eye is an essential part of the multi-scale interactions that occur within the TC inner core. The eye is generally viewed as a warm, upper level airmass resting above a cool, moist airmass, with a strong temperature inversion separating the two around 500-850 hPa [Houze, 2010, Willoughby, 1998]. Trajectory analysis suggests that air mixes between the eye and eyewall at most heights, but the importance of this mixing on hurricane intensity is still debated [Persing and Montgomery, 2003, Cram et al., 2007, Hioki and Tsuboki, 2021]. While increased equivalent potential temperature (θ_e), a measure of the entropy of moist air, in the lower eye does not seem to impact TC intensity [Bryan and Rotunno, 2009, Zhou et al., 2020], high θ_e air can indirectly affect a TC's intensification rate through enhanced inner eyewall convection [Wang and Heng, 2016], or through eye inversion strength changes related to turbulent diffusion of radial momentum along the eye-eyewall interface [Emanuel, 1997]. Furthermore, high θ_e eye air can mix with low level eyewall air to generate deep convective bursts, enhancing TC intensity [Barnes and Fuentes, 2010, Braun, 2002, Eastin et al., 2005, Guimond et al., 2016, Hazelton et al., 2017]. Meanwhile, other mixing processes like the exchange of air between the moist lower eye and dry mid-level eye remain poorly observed. The aforementioned interactions contribute to shifting intensification rates, thus better understanding how atmospheric processes in the TC eye couple with eyewall convection and boundary layer inflow can improve intensity change forecasts.

TC eye dynamics and thermodynamics are related to its cloud field. Pioneering early research used aircraft-deployed dropsondes and photographs to summarize eye cloud variability [Jordan, 1961, 1952, Malkus, 1958, Simpson, 1952, Simpson and Starrett, 1955]. These studies argue that the atmosphere below strong eye inversions typically contains a flat deck of stratocumulus clouds, while

more unique structures like hub clouds, ventilation regions, and deep eye clouds are sporadically observed [Aberson et al., 2006a, Barnes and Fuentes, 2010, Fletcher et al., 1961, Hirano et al., 2022, Houze, 2010, Schubert et al., 2007a]. Eye-eyewall mesovortex circulations also form distinct cloud patterns and mix air between these two regions [Kossin et al., 2002, Kossin and Schubert, 2004]. Nevertheless, previous eye cloud studies were limited by the observational capabilities available at the time. For instance, while satellite observations view some TC eye clouds, they offer little insight into their vertical distribution, and their infrared channels are often obscured by central dense overcast (CDO), especially for developing systems [Blackwell et al., 2018, Hirano et al., 2022, Knapp et al., 2018, Vigh et al., 2012].

Aircraft reconnaissance offers critical insights on many aspects of TC dynamics, but its current contributions towards understanding TC eye clouds are limited [Rogers, 2021, Zawislak et al., 2022]. Dropsondes precisely identify inversions, but their small sample volumes miss important components of heterogeneous eye cloud structures [Ahern et al., 2019, Hirano et al., 2022, Jordan, 1961, Willoughby, 1998, Zhang et al., 2013]. In-situ measurements provide detailed records at flight height but miss important boundary layer changes [Bell and Montgomery, 2008, Kossin and Eastin, 2001, Martinez et al., 2017]. The tail Doppler radar (TDR) equipped on NOAA's P-3 Hurricane Hunter aircraft deliver the most spatially detailed depictions of TC rainfall distributions and dynamics, but these radars' detection sensitivities are too low to observe most TC eye clouds [Boehm and Bell, 2021, DesRosiers et al., 2022, Rogers et al., 2013b, 2015, Zhang et al., 2022b], stressing the need to utilize a new measurement technique.

Here, we fill many gaps in our understanding of TC eye cloud structure using airborne lidar measurements. The compact Raman lidar (CRL) was deployed on NOAA's P-3 aircraft during the 2021 and 2022 Atlantic hurricane seasons. For the first time, detailed cloud height and thermodynamic profiles have been collected from 91 eye passes in 9 TCs. The characteristics of CRL and other P-3 based instruments are discussed in Section 2. These aircraft measurements use newly developed algorithms to examine the relationship between features like eye clouds and thermodynamic anomalies. Section 3 employs case study and statistical approaches to map eye

cloud heights and their variability. Concluding remarks are provided in Section 4.

2.2 Methods

The CRL provides 2D curtains of temperature, water vapor, rainfall, and cloud top data along the P-3 flight path. This downward pointing lidar samples the atmosphere below the plane at 6 m vertical and 260 m horizontal resolution. While the CRL's elastic channel signals can penetrate through dense rainfall, these signals are quickly attenuated by optically thick clouds, allowing for the precise determination of cloud top heights. CRL water vapor is derived by taking the ratio nitrogen and water vapor Raman scattering channel signals, and temperature is calculated using the ratio of signals from high J and low J Raman rotational channels [Liu et al., 2014, Wu et al., 2016]. All CRL datasets are height corrected and account for molecular backscattering.

To separate rainfall regions from clouds, a cloud top detection algorithm is applied to CRL profiles from all available aircraft eye passes. This objective algorithm searches downward from the flight level for the first prominent and narrow power peak above a -25 dB threshold, representing the nearest cloud top return signal. This newly developed algorithm, inspired by previous research [Wang and Sassen, 2001], was tested on all available TC eye passes, and results were deemed favorable after visual inspection. A demonstration of this algorithm is provided, and two vertical power profiles are selected to show how the cloud height algorithm handles different CRL returns (Figure 2.1a). Profile 1 depicts how rainfall has uniform but elevated backscattered power signals, while cloud tops lead to intense, jagged backscatter returns (Figure 2.1b). The first layer of intense backscatter detected by the CRL is defined as the cloud top. Profile 2 shows how clear air has a uniform, low power signal, while aerosols have sharp yet less well pronounced peaks starting at 250 m above the ocean surface (Figure 2.1c). Aerosols differ from cloud returns mainly by weak signal attenuation after the initial signal increase due to significantly lower aerosol extinction coefficients than cloud extinction. 24218 vertical profiles in the TC eye region were collected by the CRL, 20255 of which detected clouds, while the rest detected the sea surface through clear air.

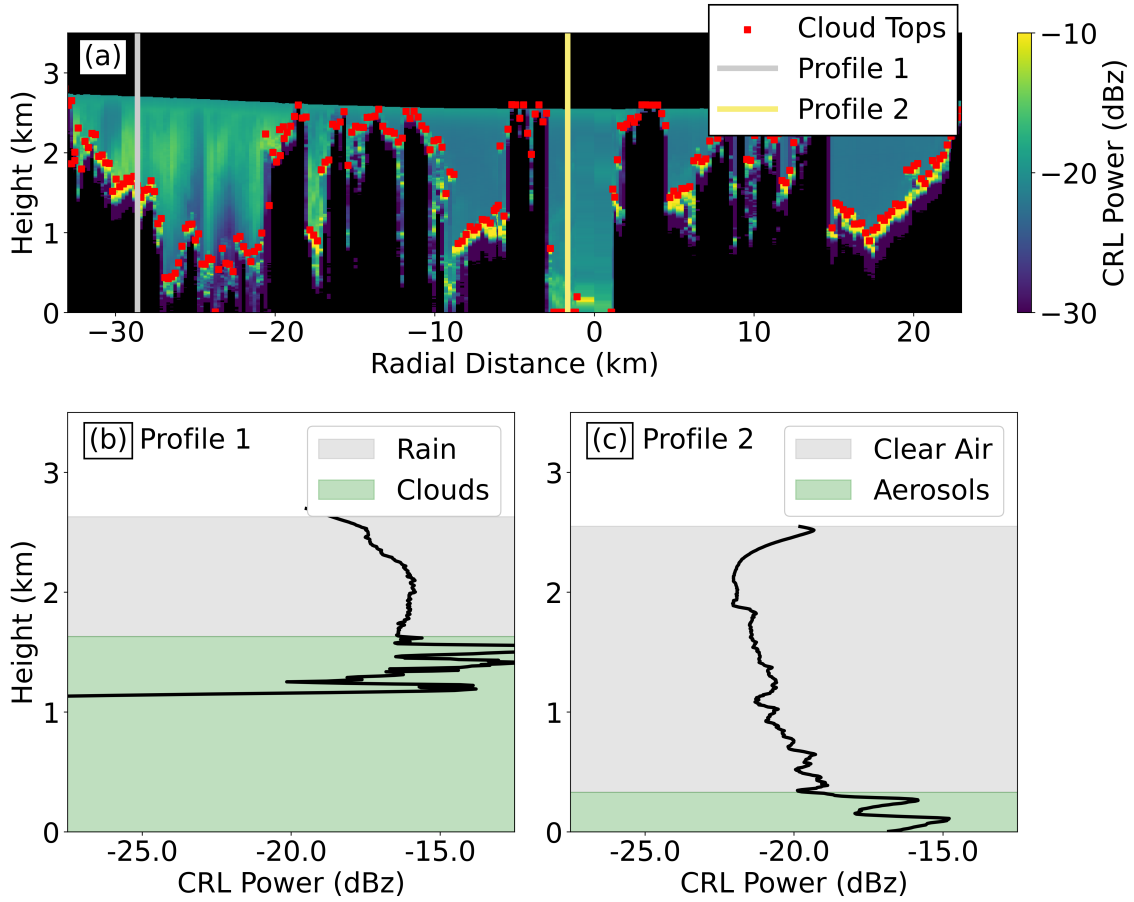


Figure 2.1: (a) Cloud top heights (red squares) derived from the downward pointing CRL backscattered power channel in the eye of TC Sam on 29 September 2021, recorded from 21:35 UTC to 21:41 UTC. Derived cloud top heights are shown as red squares and regions of total attenuation from clouds in black. Regions of high backscatter from cloud tops have values around -10 dB, precipitation and boundary layer aerosols are between -12.5 dB and -17.5 dB, and clear air has return strengths around -20 dB. The locations of profile 1 and profile 2 are shown by the gray and yellow lines respectively. (b) Power profile 1 showing precipitation and cloud backscatter signals. (c) Power profile 2 showing clear air and aerosol backscatter.

CRL cloud height and thermodynamic data synergize well with other P-3 measurements. First, TDR reflectivity and wind profile data, with 150 m vertical and 1500 m horizontal resolution, provide information on TC precipitation and wind structure. 1 Hz flight-level data provide thermodynamics and winds along the flight path [Murray and Wang, 2024]. Using intensity (Vmax) estimates from the National Hurricane Center, we composite cloud heights based on the following four categories: tropical depression (TD, $20 \text{ kt} \leq \text{Vmax} < 34 \text{ kt}$), tropical storm (TS, $34 \text{ kt} \leq$

$V_{max} < 64$ kt), weak hurricane (WH, $64 \text{ kt} \leq V_{max} < 96$ kt), and strong hurricane (SH, $96 \text{ kt} \leq V_{max}$). The TC intensity associated with each flight is summarized in the appendix (Figure A.1, Table A.1), and intensity parameters are derived from the Statistical Hurricane Intensity Prediction Scheme (SHIPS) dataset [DeMaria et al., 2005].

To prepare for statistical analysis, eye limits are established for each pass using one of two methods, depending on the intensity of the TC. For mature TCs, the eyewall is first identified using collocated TDR reflectivity and winds, flight level winds, and CRL cloud heights. Then, only CRL heights proximal to the eyewall base are used. This narrow definition of the TC eye prevents eyewall clouds from being counted and serves as a conservative estimate of low-level eye size. For weak TCs without defined eyewalls, data within 50 km of the storm's low-level circulation center are retained to sample these systems' inner cores. Sensitivity tests were conducted with other distance limits, and the results were similar across tests. The distance to the circulation center is found by comparing aircraft locations to NOAA Hurricane Research Division 2 minute track files. Figure A.2 shows all shear-relative P-3 eye flight paths. There is ample spatial coverage of the TC eye for subsequent statistical tests.

TC inner core clouds are statistically investigated by compositing flight legs and finding eye cloud top distributions. Cloud heights are grouped into 125m vertical bins, and a 5-point boxcar function smooths final distributions to remove noise while preserving distribution shape. Eye passes are then separated by the aforementioned TC intensity categories, with all intensity composites producing unique cloud height distributions. Monte Carlo and Jackknife tests confirm the statistical significance of the different cloud height peaks within these distributions (Figure A.3). The only test that introduces uncertainty is the Jackknife test for the TD distribution's lower peak, as one eye pass accounts for over half that peak's cloud height probability. This peak does not influence the final analysis, and all other eye passes have limited individual effects on their distributions. Eye vertical velocity distributions recorded at flight level and collected within CRL eye limits are similarly composited by intensity.

To better determine optimal model resolutions for representing TC eye clouds, the dominant

eye cloud widths are found using CRL cloud detections. Sliding bin widths ranging from 0.5 km to 10 km separate cloud heights horizontally, and the cloud height mean, standard deviation, and range are calculated at each scale, where the range for each bin is defined as the difference between the cloud height maximum and minimum.

2.3 Results

2.3.1 Hurricane Sam Case Study

P-3 aircraft observations from Hurricane Sam on 27 and 29 September 2021 provided unique views into TC inner core structural change (Figure 2.2). Category 4 Sam was slowly intensifying, experiencing moderate shear, and underwent an eyewall replacement cycle during both passes (Table A.1). P-3 TDR reflectivity measurements highlight Sam's eyewall and rainband precipitation structure, but they crucially miss the highly variable cloud tops filling the region (Figure 2.2a, 2.2f), demonstrating that clouds present in the TC eye produce little precipitation and that a new measurement technique to detect the cloud top is required.

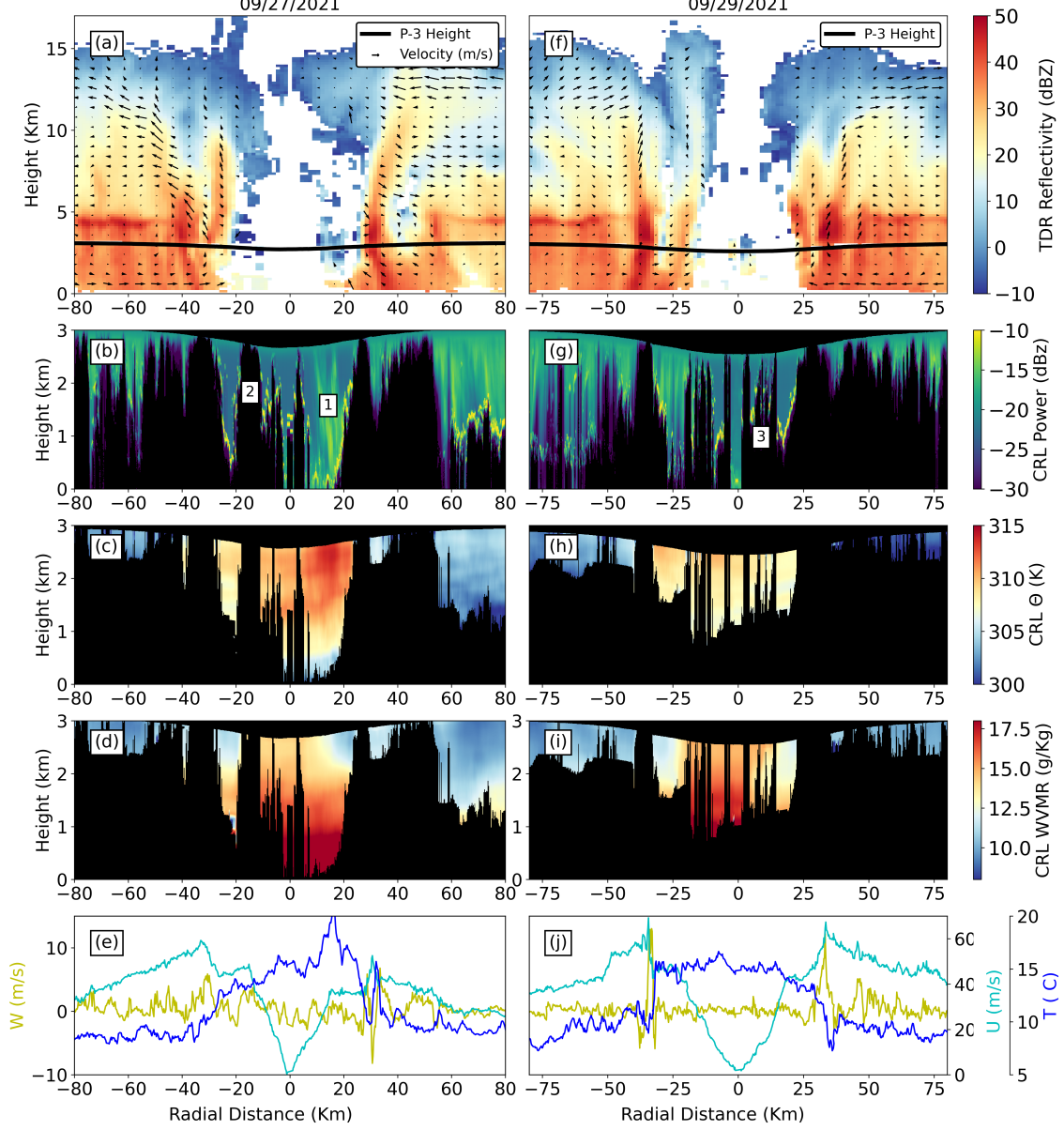


Figure 2.2: (a, f) TDR profile view of TC Sam’s wind field (arrows) and reflectivity (shading) on 27 and 29 September 2021. The legend arrow matches 15 m/s radial wind, and vertical winds have been tripled for circulation clarity. CRL measurements of backscattered power (b, g), potential temperature (c, h) and water vapor mixing ratio (WVMR) (d, i) within TC Sam’s inner core. Black regions denote total signal attenuation from clouds. Numbered features (1 and 2 in (b), 3 in (g)), are discussed in the main text. CRL data are collected below flight height at 700 hPa (black line in a, f). (e, j) Flight level measurements of total wind speed U , vertical velocity W , and temperature T .

CRL backscattered power measurements showed important differences in Sam’s low level

cloud field missed by the TDR (Figure 2.2b, 2.2g). On 27 September, a highly asymmetric cloud field was present in Hurricane Sam's eye. Rain entrained on the right side of Sam's eye reached the sea surface along its sloping eyewall (Feature 1), while the left side of the eye remained cloud free. A large (7 km wide) convective cell reached P-3 flight-level height on the left side of the eye (Feature 2), and smaller (1-3 km wide) convective clouds appeared throughout the TC center. Cloud sizes are calculated by finding the horizontal edges of CRL detected clouds, and these cloud top heights have irregular convective features, rather than flat stratiform characteristics. The presence of these clouds suggests strong mixing is occurring within the TC eye than previously expected. On 29 September, the sloping eyewall clouds were still present, but Sam's eye was more uniformly filled with 1-2 km wide convective cells reaching flight level (Feature 3). The left side of the eye was shrouded in rainfall while the right remained cloud free. Overall, TC Sam's eye cloud field shifted from an asymmetric convective state to one more uniformly filled with smaller convective cells.

The spatial variability in CRL derived potential temperature and water vapor mixing ratio (WVMR) explained Sam's changing eye cloud field (Figure 2.2c-2.2d, 2.2h-2.2i). On 27 September, Sam's eye was approximately 5 K warmer than its environment with a mean potential temperature of 309.9 K, and the temperature was higher on the right side of the eye. For all temperature and water vapor mean values found throughout the TC eye, all calculations are limited to the atmosphere above cloud tops due to signal attenuation within and below clouds. The mean WVMR of 14.6 g/kg suggested that Sam had a fairly moist eye. The strong temperature inversion on the right side of Sam's eye indicated that active subsidence prevented cloud formation. The entrained rainfall and lower moisture in this region also suggested that subsidence was occurring, as airmasses were pulled downwards from mid-levels into the lower eye. Meanwhile, the weaker temperature inversion on the left side favored convection (Figure 2.2b). By 29 September, the mean WVMR rose to 15.2 g/kg and the eye cooled by 1.9 K. The elevated moisture and weaker temperature inversion measured by the CRL across the eye provided a more favorable environment for widespread lower eye convection, consistent with [Hirano et al., 2022]. Cloud free moats of air along the sloping eyewalls persisted during both sampling periods due to enhanced subsidence in this region,

explaining the lower mixing ratios near the eyewalls [Schubert et al., 2007a].

P-3 flight level data provided additional insight into Hurricane Sam's evolution (Figure 2.2e, 2.2j). Flight-level temperature measurements matched the asymmetries found in the CRL data. Flight-level tangential winds peaked around 60 m s⁻¹ on both days and exhibited secondary flight-level wind peaks, suggesting the occurrence of an eyewall replacement cycle [Martinez et al., 2017, Sitkowski et al., 2011]. Vertical winds peaked in the strong eyewall updrafts, while the downdrafts flanking the eye-eyewall boundary were consistent with the cloud free air in these regions.

Strong vertical velocity fluctuations in TC Sam's eye suggest that for intense TCs, vertical mixing is important at flight level, despite vertical stratification. This indicates that Sam's convective eye clouds are partially associated with boundary layer mixing. While other processes like fluctuations from gravity waves impact the vertical velocity at 700 hPa, vertical mixing from the boundary layer plays an important role in convective cloud development. Shallow convective cell formation is widespread, as similar clouds are seen in CRL passes from other TCs. These clouds moisten the TC warm core in the lower troposphere, promoting further eye convective development. Previous observational studies linked TC intensification to entrainment of high entropy eye air into the eyewall [Barnes and Fuentes, 2010, Guimond et al., 2016], but our study is the first to point out the important role of warm, moist eye air in eye cloud development. This case study emphasizes how shallow convective cloud formation driven by strong vertical mixing is an essential component of intense TC eyes.

2.3.2 Statistical Analysis Results from All Cases

TC eye clouds are vertically distributed differently for each TC intensity category. TDs have the most elevated cloud peaks, suggesting that the weakest TCs often have convection filling their circulation centers (Figure 2.3a). The predominantly tall TD cloud heights are explained by their vertical velocity distribution (Figure 2.3b). Vertical velocity is positively skewed for TD cases and has a mean value of 0.19 m s⁻¹. As the TD's low pressure system establishes itself, deep convection builds near the circulation center, resulting in taller clouds and upward motion. These convective

updrafts lift high θ_e air into the middle troposphere, making the TC environment more supportive for additional development, like in Simpson et al. (1998). Weaker TSs also exhibit this tall cloud height peak for similar reasons. These central, taller convective clouds differ from the clouds found in high intensity cases.

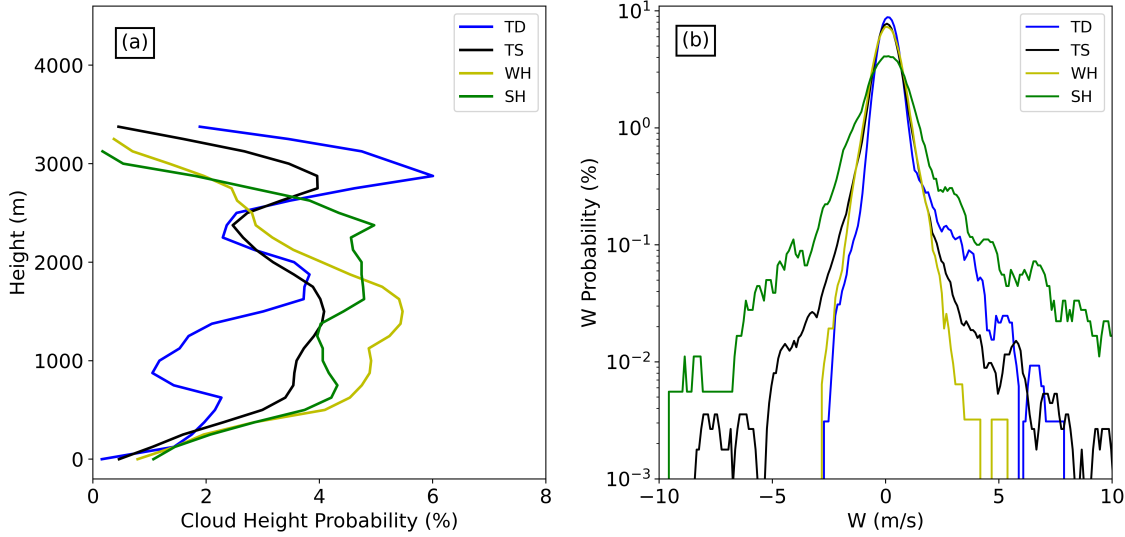


Figure 2.3: Cloud height (a) and its associated vertical velocity (b) distributions for different TC intensity categories. For cloud distributions, heights are shown on the y axis and the percent probability of falling within a given height bin is plotted on the x axis. A larger x value corresponds to a more common cloud height. For velocity distributions, probabilities are plotted along the y axis. Percentages sum to 100 for all distributions.

Besides the aforementioned elevated TS peak, most TS and WH cloud tops are below 2 km, differing from TD cases and suggesting that shallow convective clouds are less common in these storms' eyes (Figure 2.3a). When at TS or WH intensity, the low level TC eye is often just beginning to form [Vigh et al., 2012]. Unlike the TD case, TS and WH flight level vertical velocities have a mean value around 0.0 m/s. These more normal distributions, which have fewer updrafts and downdrafts at flight level compared to the SH case, are associated with less convective cloud development (Figure 2.3b). The lack of large upward motion and intense eye mixing combine to limit TS and WH cloud heights.

Finally, SHs have elevated eye cloud heights due to unique physical processes (Figure 2.3a).

These shallow convective clouds are supported by eye vertical velocity distributions with greater variance, meaning that stronger, more frequent updrafts and downdrafts occur (Figure 2.3b). A new pathway for eye dynamic evolution, where moist boundary layer air mixes vertically past the TC eye inversion through convectively driven updrafts and downdrafts, supports an elevated cloud height distribution. While this vertical mixing process works in tandem with horizontal eye-eyewall mixing driven by mesovortices [Cram et al., 2007, Guimond et al., 2016, Kossin et al., 2002], vertical mixing within the eye remains important but unquantified. TC eye clouds are controlled by both buoyancy and stability. These results show that air parcels with strong buoyancy could overcome the eye temperature inversion to form deeper eye clouds and mix high θ_e air upwards. The transition from WH to SH eye clouds indicates that low-level buoyancy enhancement outpaces the stability increase within the eye as storm intensity increases.

Horizontal cloud analysis shows that over half of all eye cloud tops are found 0.75 km to 2 km above the sea surface at 4 km bin widths, with similar relationships existing for other widths (Figure 2.4a). Since mean cloud heights do not change significantly, bin size has little effect on this quantity. Note that there is a wider spread in mean heights at small bin scales, shown by the wider interquartile range (IQR). This is because smaller bins capture more fine scale cloud top height variations than larger bins, increasing the distribution's variance.

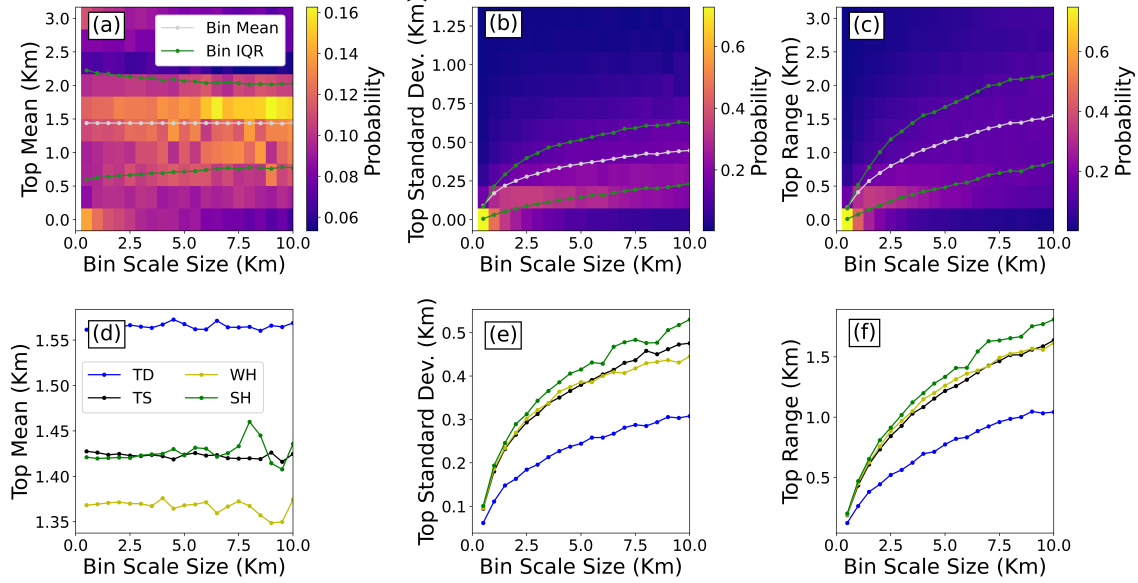


Figure 2.4: Cloud height mean (a), standard deviation (b), and range (c) heat maps for horizontal bin sizes between 0.5 km and 10 km using all CRL derived cloud heights. Bin widths are always shown along the x axis, and statistics are shown on the y axis. Normalized probabilities sum to 1 along columns, and higher normalized probabilities represent more common occurrences for a given bin. The mean and interquartile range for each bin is shown by grey and green lines, respectively. Average bin means (d), standard deviations (e), and ranges (f) for different TC categories. Each line is calculated in the same manner as the grey lines shown in (4a-4c).

As bin sizes increase, the standard deviation and range of cloud heights increase (Figure 2.4b, 2.4c). At the smallest observed bin size of 0.5 km, the average standard deviation is 0.21 km and the average range is 0.26 km. These small values suggest that the cloud top height spread within small bins is minimal. If we expand bin sizes to 5 km, however, the average standard deviation and range increase to 0.37 km and 1.27 km, respectively. The widening IQR further emphasizes this spreading feature. This analysis demonstrates that small horizontal bins are required to accurately capture eye cloud top variations. As bin sizes increase, the cloud height spread quickly increases before its rate of increase tapers off. This highlights the need to use the lowest bin size possible for research and operational purposes to capture a realistic eye cloud field. The importance of horizontal resolution in depicting changes in eyewall convection is known [Gentry and Lackmann, 2010, Jin et al., 2014, Xu and Wang, 2021], but this is the first study to consider dominant observational eye cloud scales.

Our results suggest that it is important to depict TC eye clouds in fine scale simulations to properly capture eye-eyewall mixing processes.

Furthermore, the large amount of cloud height variation is typical of cumulus type clouds, which have rough, variable cloud tops. In comparison, stratocumulus clouds show little vertical variation over many kilometers, even within intense TCs [Houze, 2010]. These results indicate that shallow, irregular cumulus clouds fill the TC eye, rather than the uniform stratocumulus decks presented in past literature [Houze, 2010, Willoughby, 1998].

Tropical depressions (TDs) have the tallest mean cloud heights, followed by SH, TS, and WH cases, respectively (Figure 2.4d), matching previous cloud height results. Standard deviation and range plots for each intensity confirm our earlier findings that TC cloud height spread increases at large bin sizes (Figures 2.4e-f). TDs are unique, as they show significantly less standard deviation and range variance at all bin sizes, suggesting that neighboring clouds have similar heights. The deeper convection seen at the center of TDs (Figure 2.3a) raises this case's mean cloud heights, and since so many clouds reach flight height at around 3 km, which is the maximum possible CRL observed height, the spread in cloud heights is lowered.

2.4 Conclusions

High resolution TC cloud heights are documented for the first time, linking convective cloud formation to enhanced vertical mixing within the eye. A case study viewing TC Sam's inner core synergizes novel CRL observations with existing measurements. Convective eye clouds form during both observation periods and are likely created by strong vertical mixing. This mixing that is initiated in the eye boundary layer helps enhance the moist entropy, and when this high θ_e air overcomes the eye's strong temperature inversion, shallow convective cells form. This case study complements previous conceptual models of the TC eye [Willoughby, 1998] by revealing the prevalence of rough-topped, shallow convective eye clouds. By displaying quantitative observations of cloud heights, this study builds upon previous research on non-stratiform eye clouds and asymmetric eye subsidence [Hirano et al., 2022, Schubert et al., 2007a, Simpson and Starrett, 1955]. Our

results suggest that low-level vertical eye mixing is an important factor in TC development.

Statistical results highlight how shallow convection within the eye plays different roles in different TC intensities. Eye vertical velocity distributions reveal how tropical depressions have enhanced mean vertical motion throughout their circulation centers, while strong hurricanes have more turbulent vertical motion. Tropical depressions and some tropical storms experience more central convective lift and cloud formation, like in Simpson et al. (1998), leading to mid-level center moistening and a more favorable environment for further development. Meanwhile, turbulent vertical mixing in the TC eye drives convective cloud formation in strong hurricanes, supplementing the horizontal mixing processes proposed by [Schubert et al., 1999]. Weak hurricanes don't display strong vertical mixing processes, explaining the limited convective cloud growth seen at the center of these systems.

Cloud height standard deviations and ranges increase significantly for large horizontal grid sizes, as 2 km grid statistics have more than double the cloud height standard deviations compared to the 0.5 km grids. Therefore, operational models with coarser resolution may incorrectly parameterize TC eye clouds and miss important sub-grid inner core processes. The importance of model resolution on TC intensity forecasts is well known [Gentry and Lackmann, 2010, Gopalakrishnan et al., 2011], but how the horizontal model resolution affects eye cloud representation is recommended to be explored in the future.

Our results suggest that convective clouds can fill TC eyes at all intensities, contradicting previous studies depicting only stratocumulus clouds forming beneath an impermeable inversion layer [Houze, 2010]. Although stratocumulus clouds occur within the TC eye, these cloud top height statistics indicate that most TC eye clouds are convective in nature. Importantly, our results show that asymmetric subsidence and vertical mass flux exchange provide pathways for mixing between the lower and mid-levels of the TC eye. Investigation into the effects of vertically mixing high θ_e boundary layer air into the mid-level eye, along with associated changes to TC intensity, is an interesting avenue of research. This study underscores the importance of collecting aircraft measurements with new instruments such as the CRL, to better understand TC inner

core structure and dynamics. If deployed more routinely alongside other novel instruments, such measurements hold great potential to improve our understanding of TC intensity change.

2.5 Acknowledgments

This research is supported by ONR Grant N00014-21-1-2606 through the TCRI Departmental Research Initiative. Jun Zhang is supported by NOAA Grant NA22OAR4590178 and NSF Grant 2211308. The authors further acknowledge the exceptional support from Jonathan Zawislak, Lisa Bucci, and all the scientists and employees of NOAA/AOML Hurricane Research Division who facilitated the deployment of the CRL and operated the instrument.

2.6 Open Research

Level 2 TDR and unprocessed in situ observations were obtained from NOAA AOML's website. Processed CRL and TDR data for the TC Sam case study used above, along with cloud heights from all CRL datasets, are available online via the link: <https://doi.org/10.5281/zenodo.10570351> [Murray and Wang, 2024].

Chapter 3

NOVEL OBSERVATIONS OF CONVECTIVE-SCALE CLOUD AND PRECIPITATION DISTRIBUTIONS IN THE TROPICAL CYCLONE RAINBANDS

Preface

This chapter is in preparation for review as cited below:

Ethan J. Murray, Kristopher B. Karnauskas, Zhien Wang, and Jun A. Zhang. Novel observations of convective-scale cloud and precipitation distributions in the tropical cyclone rainbands.

In Preparation, 2025a

Abstract

Tropical cyclone (TC) rainbands pose wind, rainfall, and storm surge threats to coastal and inland communities, yet diagnosing rainband cloud structures remains a challenge. While radar reflectivity data can estimate the presence of convective and stratiform precipitation, cloud signals cannot be separated from rainfall signals. In this work, compact Raman lidar (CRL) backscattered power data collected by the NOAA P-3 are used alongside traditional radar, stepped frequency microwave radiometer, and in situ measurements to separate low-level convective clouds, shallow clouds, stratiform precipitation, and clear air. This partitioning algorithm is demonstrated in a case study of TC Sam (2021), and it allows for the observation of cloud structures with unprecedented horizontal detail.

The classifications created by the CRL have unique kinematic and precipitation properties, and the widths of convective and boundary layer cloud structures are determined for the first time.

Shear quadrant-based tests reveal that the downshear left (upshear right) quadrant contains the most (least) coverage of low-level convection and the least (most) coverage of clear air. Shifting from low to moderate shear increases these TC shear induced asymmetries. This study agrees with previous work studying TC asymmetries while using robust cloud height information collected by the CRL, and the low-level cloud scale statistics presented here fill a meaningful gap in our knowledge of the TC rainbands.

Significance Statement

Tropical cyclone rainbands form outside the eyewall in strong storms, and their large spatial coverage increases hazards during landfall. Despite the major risks to communities posed by these features, detailed cloud and rainfall structures have not been documented. In this work, we use new cloud height and rainfall measurements from an atmospheric lidar deployed on one of NOAA's hurricane hunter aircraft to fill this research gap. Our results show that in many rainbands, small convective clouds are often separated by narrow gaps of stratiform rain and clear air. This differs from previous work, which observed more uniform convection and stratiform clouds in the tropical cyclone rainbands. We also investigate how rainbands vary in different storm regions, finding that certain rainband areas have more convection and less clear air than others. Overall, this work uses a new remote sensing instrument to provide new insight into tropical cyclone rainband clouds and precipitation.

3.1 Introduction

Tropical cyclones (TCs) cause the most annual economic damage in the United States [Klotzbach et al., 2018, 2022, Muller et al., 2025], and these impacts are expected to increase [Anderson et al., 2020, Dinan, 2017, Iglesias et al., 2021, Mendelsohn et al., 2012]. While the TC eyewall contains the strongest winds and rainfall rates, its narrow width limits the most extreme damage to a smaller path along the storm track [Muller et al., 2025, Wakimoto and Black, 1994]. In contrast, TC rainbands have weaker winds and rainfall, but their risks extend across a much

wider area, linking larger TC size to increased economic damage [Guzman and Jiang, 2021, Zhai and Jiang, 2014].

TC rainbands pose multiple threats to coastal and inland communities. Rainbands are comprised of large stratiform and convective precipitation regions that significantly contribute to freshwater flooding hazards, especially during and after TC landfall [Guzman and Jiang, 2023, Hagen et al., 2025, Jaffrés and Gray, 2023, Zhou and Matyas, 2017]. Rainband winds generate strong storm surges, especially for systems undergoing extratropical transition [Jones et al., 2003, Kunz et al., 2013, Rappaport, 2014, Wahl et al., 2015]. TC supercells and tornadoes are found in landfalling and inland rainbands, which create localized wind and precipitation damages [Alford et al., 2024, Edwards, 2012, Nowotarski et al., 2021, Schenkel et al., 2023]. Rainbands often impact communities hours before and after the storm's official landfall, making it challenging to communicate the many risks posed by the TC rainbands with the public in a timely manner [Bosma et al., 2020, Cosgrove, 2023, Jones et al., 2019]. By observing the structure and distribution of TC rainband clouds with unprecedented detail, we aim to provide the information necessary to improve TC models and reduce the societal risks posed by these storms.

TC rainbands are typically composed of a principal rainband, secondary rainbands, and distant rainbands [Emanuel, 2018a, Houze, 2010]. The principal rainband is a broad region of stratiform and convective precipitation in the inner core [Willoughby et al., 1984], and they are most common in strong TCs. The inward advection of low θ_e air from principal rainband convective downdrafts limits TC intensity by cutting off the eyewall's primary energy source [Powell, 1990, Wadler et al., 2018b, 2021], which makes properly modeling the principal rainband essential for TC intensity prediction.

Principal rainbands display a wavenumber-1 rainfall asymmetry mainly forced by environmental shear [Barnes et al., 1983, Corbosiero and Molinari, 2002, Rogers et al., 2003]. Our work uses the environmental shear vector to partition the TC rainband into four quadrants: upshear right (UR), downshear right (DR), downshear left (DL), and upshear left (UL).

UR rainbands have the least rainfall and experience sporadic, isolated convection, as this

region is just starting to regain high surface θ_e values [Chen et al., 2021b, Hence and Houze, 2012, Wadler et al., 2022]. Updrafts spread and strengthen in the DR quadrant, which support vigorous convection and increased precipitation [Barron et al., 2022, Didlake and Houze, 2013a]. Convection matures in the DL quadrant and creates the highest rainfall totals, but cells begin to weaken and transition into stratiform precipitation [Houze, 1997]. Finally, rainband convection fully collapses and transitions into stratiform rain in the UL quadrant, flushing the boundary layer with low θ_e air through strong downdrafts [Didlake and Houze, 2013b].

Secondary rainbands are smaller features that typically propagate outwards from the TC inner core as vortex Rossby waves [Corbosiero et al., 2006, Li and Wang, 2012, Montgomery and Kallenbach, 1997, Reasor et al., 2000]. Inner core secondary rainbands can also cut off supplies of high θ_e air to the eyewall, resulting in vortex weakening, an expansion of the wind field, and an eyewall replacement cycle (ERC) [Cheung et al., 2023, Black and Willoughby, 1992, Didlake et al., 2017, 2018, Fischer et al., 2020, Houze et al., 2006, 2007, Sitkowski et al., 2011].

The distant TC rainbands display markedly different properties than their inner core counterparts. These rainbands are located roughly 100 km to 250 km from the TC center, have a more limited radial extent, and tend to possess more squall-line like properties such as strong convective cells, a clear convergence zone, a strong low-level cold pool, and enhanced total CAPE [Bogner et al., 2000, Yu and Tsai, 2013, Yu et al., 2018, 2019]. This study uses observational data from all three of these rainband features.

While observations helped create this conceptual model of TC rainbands, direct observations of low-level clouds are nonexistent using traditional radar, dropsonde, and flight level methods. The benefits and drawbacks of these traditional measurement platforms are discussed below before introducing a new, innovative measurement technique. Liquid water content measurements at flight level can approximate cloud boundaries, but these observations provide no cloud height variation information and the immersion thermometers used on the NOAA P-3 aircraft suffer from detector wetting issues [Eastin et al., 2002]. Dropsondes can detect cloud tops through changes in moisture and temperature, but these measurements are isolated to single vertical columns [Willoughby, 1998].

Radar data from research aircraft and satellites account for most TC rainband wind and precipitation observations [Barnes et al., 1983, Didlake and Houze, 2009, Hence and Houze, 2012]. Radars provide 3D wind fields essential for studying rainband updrafts and downdrafts [Barron et al., 2022, Didlake and Houze, 2013b], and their reflectivity fields show the areas of heaviest precipitation [Tang et al., 2014, Yu et al., 2018]. Radar data are also used to classify rainfall regions as convective, stratiform, or clear air [Fritz et al., 2016, Houze, 1997, Rogers et al., 2007, 2020, Tao and Jiang, 2015, Wadler et al., 2023a, Yuter and Houze, 1995]. This is possible because strong convective cells are associated with deep updrafts, downdrafts, and increased low-level reflectivity values [Aberson et al., 2006b, Houze, 1997], while stratiform rainfall more often displays mid-level convergence, aggregation of ice particles above the melting layer, and weak low-level downdrafts [Houze, 1997, Yuter and Houze, 1995].

While radar data illuminate many aspects of TC structure, they don't allow for the separation of cloud signals from entrained rainfall. For instance, while radar data can be used to estimate rainband updraft and precipitation region widths [Barron et al., 2022, Didlake and Houze, 2009, Houze, 1997], they cannot be used to directly observe cloud boundaries when cells are embedded within precipitation. Obtaining these convective scale cloud observations is essential to improving TC simulations, as the TC cloud field is intrinsically tied to its thermodynamics and kinematics [Alland et al., 2021a, Houze, 2010]. This knowledge gap in TC cloud structure must be addressed using novel observations, as inaccurately simulated cloud fields could impact vortex structure, rainfall and intensity forecasts [Zhang et al., 2023].

The goal of this research paper is to accurately separate rainband cloud tops from entrained rainfall and calculate the cloud property statistics necessary for model verification. Measurements from the compact Raman lidar (CRL) are used to fill this knowledge gap by characterizing boundary layer and convective cloud widths for the first time. CRL measurements are synergized with flight level and tail Doppler radar (TDR) observations along the same flight track to reveal the essential properties of rainband sectors. After thoroughly observing TC cloud properties, research and operational model forecasts can be verified and improved in future work through parameterization

changes focused on modifying cloud structure [Alaka et al., 2024, Nolan et al., 2009b, Zhang et al., 2012].

In Section 2, the observational datasets, statistical methods, and CRL analysis algorithms are described in detail. A case study of TC Sam (2021) demonstrating these analysis algorithms is presented in Section 3. CRL-derived cloud properties across a much more comprehensive dataset are unveiled in Section 4, providing a novel description of convective and stratiform rainband structure. This section also compares CRL cloud properties to flight level and TDR kinematic fields. Section 5 analyzes the asymmetric distribution of rainband clouds and rainfall, and Section 6 discusses these results and proposes future research directions.

3.2 Methods

3.2.1 Observational Datasets

The CRL provides high resolution cross sections of temperature, moisture, light scattering ratio (LSR), and backscattered power data along aircraft flight transects [Liu et al., 2014, Wu et al., 2016]. The downwards-pointing lidar emits 354.7 nm light at a pulse rate of 30 Hz, and after processing the data, final CRL cross sections have horizontal and vertical resolutions of 250 m and 6 m, respectively. The CRL was deployed on the NOAA P-3 aircraft during the 2021 and 2022 Atlantic hurricane seasons. CRL temperature and water vapor profiles show strong agreement with dropsondes. CRL data have been successfully used to investigate atmospheric phenomena such as mesoscale convective systems [Lin et al., 2019] and undular bores [Lin et al., 2021], and they have recently been used to enhance our understanding of TC eye clouds [Murray et al., 2024] and to validate dynamical TC forecasts (Murray et al. [2025b], under review). The CRL's backscatter power channel is primarily used for this analysis.

To better understand TC kinematic and microphysical processes, CRL profiles are compared to TDR data. The TDR is routinely operated during P-3 reconnaissance flights, and the instrument provides extensive reflectivity and 3D wind fields from TCs dating back to 1997 [Fischer et al., 2023,

2022]. Both TDR swath and profile data are used in this analysis. While TDR swath data provide 3D coverage of the storm's inner core, they have lower vertical and horizontal resolutions of 0.5 km and 2 km, respectively. Meanwhile, profile datasets only provide 2D cross sections along the flight track, but they have improved horizontal and vertical resolutions of .15 km and 1.5 km, respectively. TDR profile data from 2021 and 2022 are directly compared to CRL backscattered power, and all TDR profile data from 2019-2023 are used for TDR composite plots since high-quality TDR data are available over this longer period, increasing confidence in the composites. Swath data are used for plan views of TC Sam' reflectivity field and precipitation classification.

In situ vertical wind (w) data are used to characterize rainband updrafts and downdrafts. These data are collected at flight height (around 3 km) and at 1 Hz frequency, roughly translating to 100m horizontal resolution depending on the flight speed of the P-3 [Kossin and Eastin, 2001, Martinez et al., 2017, Wadler et al., 2025]. Stepped frequency microwave radiometer (SFMR) rainfall data from along the P-3 track are also compared to CRL profiles [Jiang et al., 2006]. All rainfall rates weaker than 5 mm/hr are removed due to noise concerns (Jiang et al. [2006], p. 200).

TC intensity and environmental shear information are determined using the Statistical Hurricane Intensity Prediction Scheme (SHIPS) dataset [Kaplan et al., 2010]. The 'SHRD' and 'SHTD' variables are used for environmental shear magnitude and direction, respectively. Environmental shear quadrants are found by comparing the location of each flight leg to the current shear direction and the TC center present in the NOAA Hurricane Research Division 2 minute track files.

3.2.2 Classifying CRL Backscattered Power

The CRL's backscattered power channel can differentiate between cloud tops, clear air, aerosols, and rainfall regions (Figure 3.2e). Rainfall regions and aerosols lead to enhanced backscatter, but due to their large particle sizes compared to the CRL's operative wavelength, they do not fully attenuate the return signal. Rainfall and aerosol backscattered powers have values between -12.5 dB and -17.5 dB; sea-spray aerosols are constrained to the atmospheric boundary layer in this application, while rainfall regions extend from flight height downwards towards the sea surface or a

low cloud top. Clear air regions, with return power values around -20 dB in nighttime observation periods.

Cloud tops rapidly attenuate CRL signals and are often capped by a narrow region of high return power [Murray et al., 2024]. This intense attenuation cuts off all thermodynamic and rainfall data within and below low-level clouds. Therefore, all observed rainfall is entrained from above the P-3 flight height, which is typically around 3 km. This is almost always stratiform rainfall due to the high cloud bases required for CRL observation ([Barron et al., 2022]).

An empirical algorithm has been developed to identify each of these CRL features (Figure 3.2f). First, cloud heights are found by scanning downwards to find where significant CRL signal attenuation occurs [Murray et al., 2024]. Next, a thresholding technique separates enhanced backscatter rainfall regions from low backscatter clear air regions. Rainfall has the P-3 flight height as an upper bound, and the sea surface or cloud top as a lower bound. The remaining regions above cloud tops are considered clear air.

Cloud regions are divided into three sub-categories: convective clouds, shallow clouds with stratiform rain above, and shallow clouds with clear air above. Convective sectors contain cells that reach within 250m of flight height; many of these features likely extend above the P-3. A filter is applied to create more coherent, distinct convective regions. Shallow clouds with stratiform rain above are distinguished from shallow clouds with clear air above by checking if any entrained rainfall signals are present above the cloud top.

After classification, five CRL atmospheric features are highlighted: convection, stratiform rainfall to the sea surface, stratiform rainfall above shallow clouds, clear air to the sea surface, and clear air above shallow clouds. Representative examples of these classifications are presented during the Hurricane Sam case study (Figure 3.2e). These classifications have both radial distance and height dimensions. To simplify these classifications for statistical tests, each x axis value is assigned a single identifying category (Figure 3.2g, CRL color bar). For flight level w and SFMR rainfall rate partitions, all five categories are retained since they each have distinct properties.

Meanwhile, for radial and shear quadrant partitions, these five categories are simplified to

three. Convective profiles are the same, stratiform rain cases above a shallow cloud or above the sea surface are grouped together, and clear air cases above a shallow cloud or above the sea surface are joined. This simplifies results by focusing on the key dynamical drivers in the region: convection, stratiform rainfall, and low-level clear air.

For TDR tests, only convection and stratiform rainfall classifications are used, as the TDR cannot retrieve wind or reflectivity measurements under clear air conditions. Finally, for the shallow cloud width and height statistics (Figure 3.5), shallow clouds from stratiform rain and clear air regions are combined. These simplifications improve statistical significance measures, while grouping categories with relatively similar cloud properties.

3.2.3 Analysis Methods

Differentiating the rainbands from the TC eyewall and eye is essential for this analysis, as these regions have very different kinematic and thermodynamic properties [Houze, 2010]. To do so, TC rainband limits are manually determined for each flight leg (Figure 3.2e). We chose to manually select rainband inner limits because using either a fixed distance inner limit for all cases or a variable limit based upon the radius of maximum wind (RMW) [Wunsch and Didlake, 2018, Zhang et al., 2022a] would often, upon visual inspection, include eyewall features and bias our results. By manually defining rainband inner limits, the amount of rainband data can be maximized while still excluding eyewall data.

To determine the inner rainband limit, the eyewall is first identified by visually identifying the innermost large convective cell in the CRL backscattered power channel. This cloud is confirmed to be the eyewall by visually identifying intense tangential and vertical winds in TDR and in situ data. The rainband limit is then placed just outside of this first convective feature. If a distinct rainband cloud isn't observed, no rainband limits are determined. An outer bound of 200 km is used to constrain flight legs that go beyond this radial distance.

For the radial comparisons made in Figure 3.7, distances are normalized by the RMW to place CRL rainband statistics into context with the TC eye and eyewall. RMW values are calculated

for individual flights by averaging together all tangential wind profiles, smoothing the result, and finding the location of maximum wind [Martinez et al., 2017]. While this RMW comparison suffers from the spatial smoothing limitations discussed above, it provides a holistic view of TC structure impossible otherwise.

To calculate the widths of convective and shallow cloud complexes, an algorithm searches radially outward from the innermost cell edge to the outermost cell edge. Cloud horizontal spacings are determined in a similar manner. The average heights of the shallow cloud layers are also calculated; doing so for the deep cloud layers is not possible because these features extend above the P-3 flight height.

TC rainband properties are partitioned into four environmental shear quadrants: UR, DR, DL, and UL. While TC motion can generate convective asymmetries [Corbosiero and Molinari, 2003, Lonfat et al., 2004], this secondary effect is only noticeable in low shear conditions (< 5 m/s) [Barron et al., 2022, Chen et al., 2006, Corbosiero and Molinari, 2003], so only shear-relative partitions are made here.

3.2.4 Cases Sampled by the CRL

The CRL collected 169 total radial legs across 32 flight days into nine TCs. 76 of these flight legs sampled hurricane strength TCs, and 64 of those legs had defined rainband complexes that were within a single shear quadrant. For 12 Cat. 1+ strength cases, a flight leg crosses between two shear quadrants or lies too close to a shear quadrant boundary, so its shear quadrant cannot be determined and the flight leg is not used for asymmetric analysis. Data from tropical depressions and tropical storms are not used, as these systems are too weak to have defined eyewall and rainband complexes.

Our TC intensity samples are relatively well distributed: there are 35, 7, 19, 15, and 0 radial legs for hurricane categories 1-5, respectively (Figure 3.1a). The near even split between minor and major hurricanes provides confidence in our results. Flight legs are not partitioned by intensity change, as a majority of the sampled cases are intensifying (Figure 3.1c). Leg counts, intensity,

environmental shear strength, and additional information are listed for all 32 TC flights in Table B1.

Most sampled storms were experiencing moderate, westerly shear (Figures 3.1e-f). Moderate shear strength is typically defined as being between 8.75 kt and 21.4 kt [Rios-Berrios and Torn, 2017]. Out of all of our TC cases, 129 of 169 flight legs fall into this moderate shear strength category, with only 26 weak and 14 strong shear cases. For Category 1+ TC flight legs, 22 weak, 48 moderate, and 6 strong shear environments were encountered. To improve the distribution of weak versus moderate shear cases in our statistical analysis, a separation value of 10.3 kt is used. Now, 38 Cat. 1+ shear values fall above this threshold, and 38 fall below it for our tests. Results are similar using either the 8.75 kt or 10.3 kt shear magnitude limits, but we have more confidence in our results due to the balanced leg counts using the 10.3 kt definition.

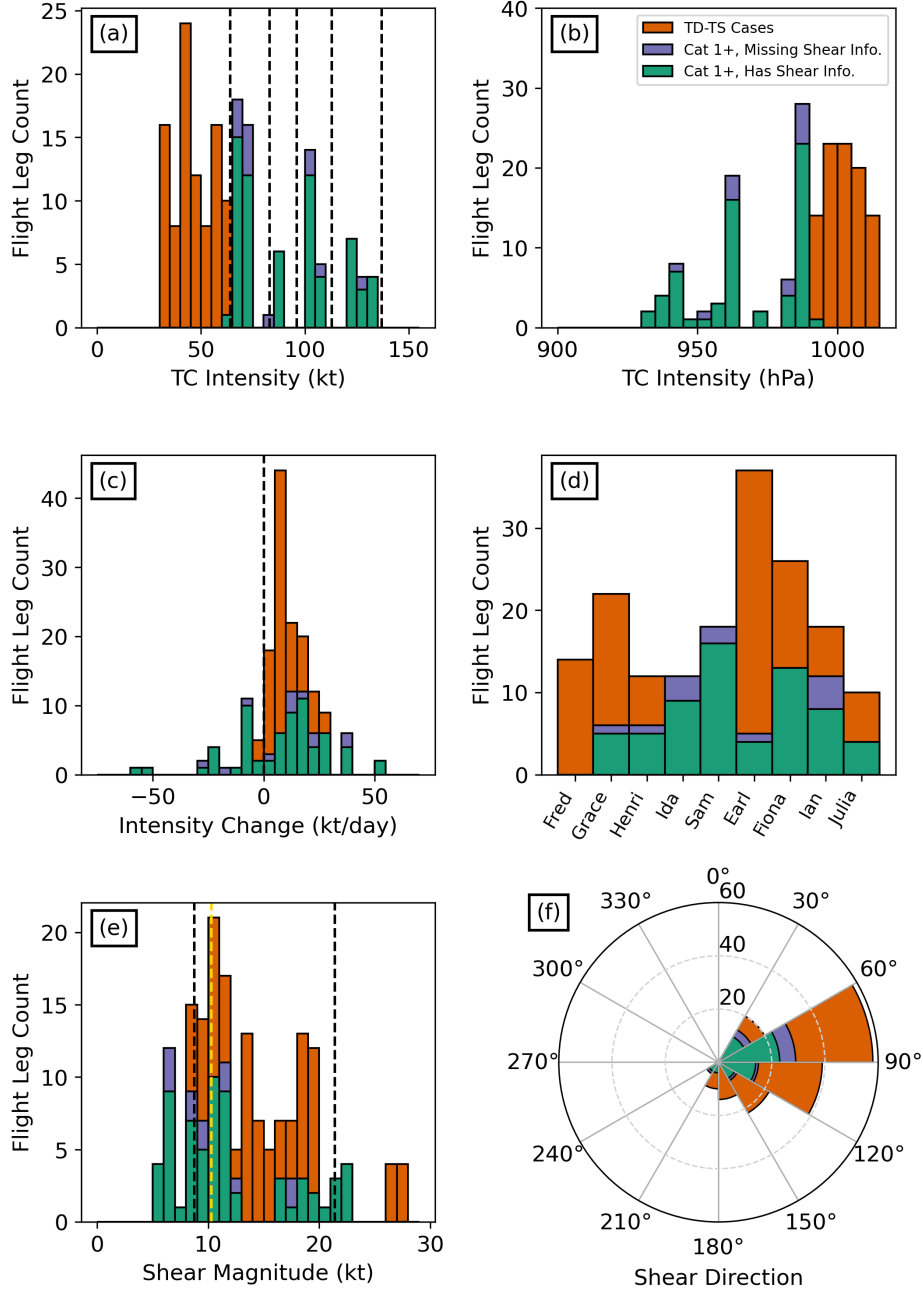


Figure 3.1: Distributions of flight legs sampled by the CRL partitioned by (a) TC sustained wind speed, (b) surface pressure, (c) intensity change, (d) TC name, (e) environmental shear magnitude, and (f) environmental shear direction. Each distribution contains data from weak TC cases (red bars), legs reaching hurricane strength with shear quadrant information (green bars), and hurricane strength legs without adequate shear quadrant information (purple bars). Black lines represent different TC category limits in (a), 0 m/s intensification rate in (b), and the original shear definitions of [Rios-Berrios and Torn, 2017] in (e). The gold line in (e) represents the new shear definition separating cases into weak and moderate shear classifications.

3.3 Case Study

3.3.1 TC Sam (2021) Rainbands: Plan View

On 0000 UTC 9/28/2021, TC Sam was a Category 3 hurricane (105 kt) east of the Lesser Antilles Islands. It had just rapidly weakened in conjunction with an ERC [Pasch and Roberts, 2022] and dry air ventilation [Tang et al., 2024]. Sam experienced weak southwesterly shear with values around 8 kt during the P-3's second eye pass (Figure 3.2a). Sam's convective structure appeared relatively symmetric but ragged in the GOES-16 infrared image, and no eye was visible at Sam's center, as central dense overcast and a tilted vortex obscured the region.

Sam's eye and eyewall were much wider after the ERC, and low-level eyewall reflectivity from the TDR was strong and symmetric, suggesting that the storm was recovering its deep inner core convection (Figure 3.2b). Sam's DL rainband had high reflectivity values across a large region, suggesting that Sam's DL rainband was predominantly convective. The UR rainband had strong convection in its innermost sector, but its precipitation was less spatially extensive, reflectivity values were moderate outside of the innermost sector, and it mostly displayed stratiform properties.

An empirical TDR precipitation algorithm [Rogers et al., 2020, Wadler et al., 2023a] classified TC Sam's precipitation (Figure 3.4c). This algorithm is originally based upon the work of Steiner et al. [1995] with ground-based radar, and it has been adapted to study TC precipitation structures. In this algorithm, 3D radar reflectivity data classify spatially coherent precipitation structures as either convective, stratiform, weak echo, or no echo using intensity, surrounding area, height, and peakedness criteria. In the DL quadrant, the inner rainband was filled with moderate and strong convection, while the outer rainband was mostly stratiform with one moderate convective band present. Meanwhile, the UR rainband had one moderate convective cell next to the eyewall, while the rest of the rainband was classified as stratiform.

3.3.2 TC Sam (2021) Rainbands: Profile View

A profile view of TC Sam's rainband using both the TDR and CRL provides additional insight into its shear induced asymmetry (Figures 2d-f). TDR data reveal Sam's outer rainband melting layer at 4.5 km height (Figure 2d). These regions are characteristic of tropical stratiform precipitation [Houze, 1997]. The reflectivity cross section confirms that Sam's DL rainband is wider and contains stronger precipitation than the UR rainband.

The CRL backscattered power channel illuminates Sam's low level cloud field (Figure 2e). In the UR rainband between -200 km and -150 km radial distance, faint precipitation fall streaks are detected, indicating very weak stratiform rainfall. Between -150 km and -70 km, a couple of narrow, tall clouds are identified, but strong stratiform rainfall and shallow clouds 1500m tall dominate. From -70 km to the inner rainband edge at -36 km, a convective region reaching close to flight height is identified. This region contains multiple convective cells and is separated from the UR eyewall by entrained rainfall.

In the outer DL rainbands (180 km - 145 km), faint fall streaks, sporadic convective clouds, and boundary layer aerosols are once again observed. From 145 km to 80 km, a large region of stratiform rainfall and boundary layer clouds is bisected by a deep, 7 km wide convective cell. From 80 km to 34 km, the inner core DL rainband has a much wider extent of deep convection. Cells range in width from 1.25 km to 9.5 km, and they are interspersed with shallow clouds and stratiform rainfall entrained from above.

3.3.3 TC Sam (2021) Rainbands: Cloud and Rainfall Classifications

The CRL cloud and rainfall classification algorithm summarizes these spatial patterns well (Figure 2f). Rainfall regions are correctly identified, including the weak fall streaks found in the outer rainbands. The algorithm identifies shallow cloud tops in the outer rainbands well, and it realistically separates deep cloud complexes when stratiform rainfall is present.

The CRL and TDR cloud classifications have some important differences (Figure 2g). First,

the CRL classification's higher horizontal resolution of 250m compared to the TDR's resolution of 2000m allows for additional detail when the CRL differentiates between convection and stratiform regions. Also, the CRL classification is based upon actual cloud height measurements, while the TDR uses reflectivity as a proxy for cloud location. This generates differences in the location and width of low level convection.

For example, UR rainband convection at -55 km is much wider in the CRL classification. In the DL rainband, the TDR portrays a larger, continuous convective region from 40 km to 80 km than the CRL. Overall, the CRL results are more realistic, highlighting the interaction between narrow convective cells with updrafts and low level downdrafts filled with entrained stratiform rainfall [Didlake and Houze, 2009]. This analysis demonstrates that while the TDR precipitation classification approximates the boundaries of convective cells well, the CRL captures overlooked, small scale cloud structures.

The CRL cloud and rainfall classification maps well onto flight level w and surface SFMR rain rates (Figure 2g). In the convective portion of the UR rainband (from -60 km to -45 km), updrafts are dominant at flight level. In the stratiform region separating the UR rainband from the eyewall, a broad downdraft is found (-45 km to -40 km). This example qualitatively shows that CRL convection is linked to updrafts, while CRL stratiform regions are connected to downdrafts. Moderate and high SFMR rain rates (>5 mm/hr) are only found in the same convective portion of the UR rainband, suggesting that CRL convective regions support enhanced precipitation generation. This classification approach is applied to all TCs with CRL data available in the following section, demonstrating that this relationship is robust across many cases.

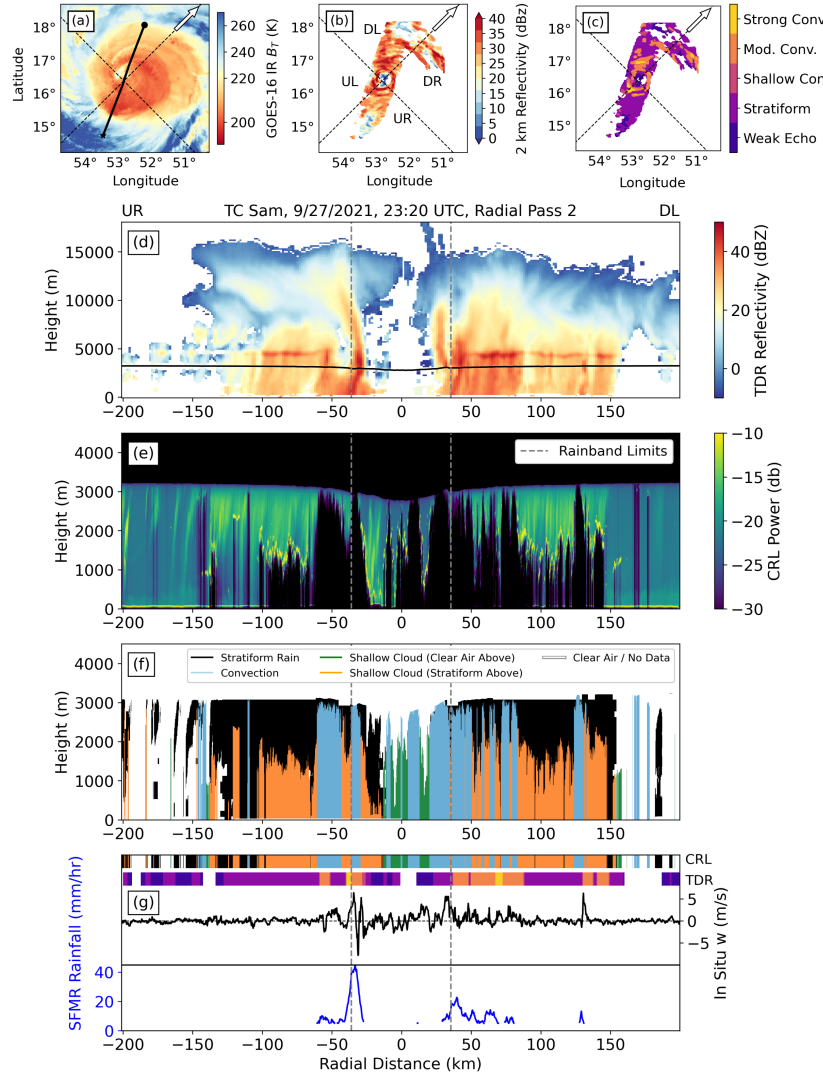


Figure 3.2: Plan view of TC Sam on 9/26/21 at 22:38 UTC. (a) GOES-16 IR brightness temperature. The P-3 flight path (solid black line), leg starting point (circle), and leg ending point (star) are indicated. The white arrow points in the direction of the environmental shear, and the dashed black lines indicate the four environmental shear quadrants. (b) Cross section of TDR reflectivity at 2 km height along the flight path. The four environmental shear quadrants are labeled. (c) TDR precipitation classification results. TDR classifications along the flight path are also displayed in (f). (d) Cross section of TDR reflectivity. Environmental shear quadrants are denoted above the subplot. The black line represents the P-3 flight height. Gray dashed lines show manually defined inner rainband limits. (e) Cross section of CRL backscattered power. Black regions depict total signal attenuation below cloud tops. (f) CRL cloud and precipitation classification results. The five possible classifications are described in the subplot legend. (g) Flight level vertical velocity and SFMR surface rainfall along the flight legs. The five respective TDR and CRL classifications are taken from subplots (c) and (f) along the P-3 flight path, and they use the same colormaps as in those subplots.

3.4 Rainband Cloud, Rainfall, and Kinematic Properties

3.4.1 Flight Level Vertical Motion Differences by CRL Classification

Data from other observing platforms are partitioned by the five CRL classification groups to see if differences emerge between each group. First, in situ vertical velocity data are analyzed to provide insight into updrafts and downdrafts at the P-3 flight height. The positively skewed right tail of the convection distribution (Figure 3a) shows that convective updrafts are significantly stronger than in stratiform or clear air regions. The distribution has a mean value of .5 m/s. This result verifies the accuracy of the CRL classification algorithm because convection is expected to contain strong updrafts. Convective regions also have many strong downdrafts, as this region is quite turbulent and contains a cellular overturning circulation pattern to maintain deep clouds [Didlake and Houze, 2009].

Areas of strong rainband convection can be identified using flight level data. For example, if a rainband updraft is 2 (5) m/s strong, Figure 3a determines that it is 4 (9) times more likely that a convective cloud is present versus another cloud type. The reverse is also true; if low level rainband convection is spotted visually by NHC crew members during a reconnaissance mission, the risk of encountering extreme turbulence can be better estimated using this vertical velocity distribution.

The stratiform rainfall category with shallow clouds has enhanced updrafts compared to stratiform cases with no shallow clouds. This is from updrafts spreading from convective regions into adjacent stratiform regions with slightly shallower cloud heights, or from shallow cells generating enough turbulence above the cloud top that it reaches flight height. The stratiform distribution has a mean value of 0.0 m/s, suggesting that weak downdrafts balance out weak updrafts at flight level. Clear air sectors have the fewest updrafts and downdrafts due to an absence of upwards forcing from tall clouds or a downwards forcing from entrained stratiform rainfall.

3.4.2 Surface SFMR Rainfall Differences by CRL Classification

SFMR rainfall distributions are compared for the three classifications (Figure 3b). First, we see that moderate to high precipitation rates are limited in clear air regions. This makes sense: there is no stratiform rainfall being entrained from above, so it must be either laterally advected into the clear air region or generated by clouds lower than 3 km height. This second process mentioned only applies to the clear air category containing shallow clouds, partially explaining why this distribution has higher rainfall rates.

Stratiform and convective regions all contain moderate rainfall rates (5 mm/hr), and convective clouds have the highest probability of heavy rain. This is because deep convection has frequent, strong updrafts that generate large rainfall rates [Houze, 1997, Steiner et al., 1995]. The stratiform rainfall category with shallow clouds also experiences high rainfall rates. This suggests that in stratiform sectors, shallow cloud precipitation often combines with stratiform rain entrained from above to generate large observed rainfall rates. Stratiform rain regions without shallow clouds are not supplemented with this additional source of rainfall, explaining their lack of large rainfall rates.

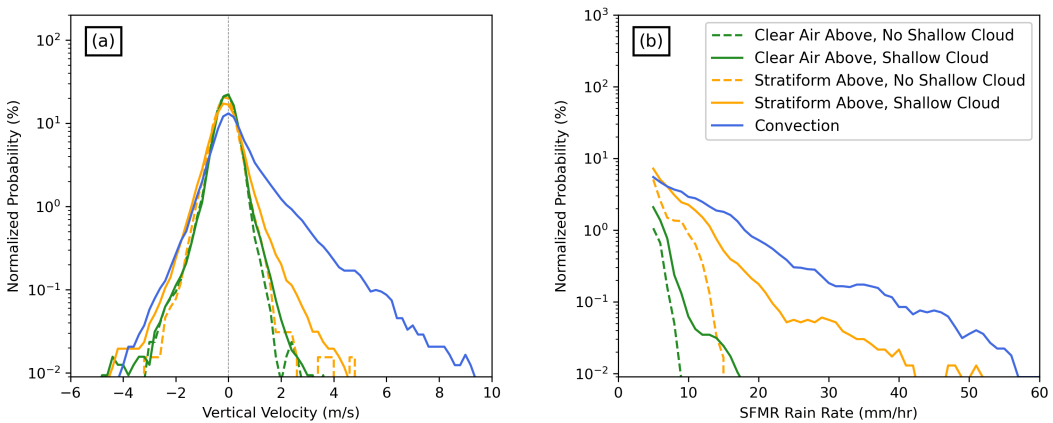


Figure 3.3: Distributions of flight level vertical velocity (a) and SFMR surface rainfall rate (b). Each distribution in (a) sums to 100%, while distributions in (b) sum to less than 100% since rain rates below 5 mm/hr are removed. Distributions in (a) and (b) have bin sizes of .2 m/s and .2 mm/hr, respectively. Data outside of ± 3 m/s and $+20$ mm/hr are smoothed with a moving average filter with a window size of 3.

3.4.3 TDR Differences by CRL Classification

This analysis is extended to TDR vertical velocity and reflectivity fields. Since the TDR collects data above and below flight height, we harness contoured frequency by altitude diagrams (CFADs) to visualize distributions throughout the troposphere [Hence and Houze, 2012]. Vertical velocity CFADs show heightened low to mid-level updrafts for convection compared to the stratiform category. The convective CFAD (Figure 4a) has positive mean TDR velocities from 1 km to 6 km heights above mean sea level (MSL). The stratiform rainfall CFAD, meanwhile, has negative mean vertical velocities from the surface to 7 km, symbolic of the weak downdrafts characterizing entrained stratiform rainfall [Didlake and Houze, 2013a, Houze, 1997]. Overall, convective regions have a mean TDR vertical velocity of .41 m/s from 0 km to 6 km, while stratiform regions have a mean vertical velocity of -.29 m/s.

These differences are best visualized by the convective minus stratiform distribution anomaly (Figure 4c). Distribution differences are greatest around 3 km because of the strongest convective updrafts at this height. Mean vertical velocity profiles are the same from 6 km heights upwards, indicating that convective updrafts linked to low level cells don't extend past the middle of the troposphere, likely from eyewall outflow and mid-level subsidence constraints [Hence and Houze, 2012].

CRL determined convective regions have stronger low level TDR reflectivity than stratiform regions (Figure 4d-f). From 4 km downwards, the convective mean profile (Figure 4d) is 2.5 dBZ stronger than the stratiform mean profile (Figure 4e). This difference is driven by an increase in 35-40 dBZ reflectivity for convective clouds, and the differences are largest around 1.5 km height, which is lower than the velocity differences (Figure 4f). This is because kinematic changes appear at their respective heights, while convective reflectivity maxima are usually located close to the surface as more precipitation particles are generated and fall through the atmospheric column [Houze, 1997].

Figure S1 repeats this process for stratiform sectors with shallow clouds compared to those

with no shallow clouds. While both distributions have negative mean w values below 7 km height, cases with shallow clouds have proportionally more updrafts. So, clouds too shallow to be classified as convection still sometimes generate enhanced low level updrafts. Stratiform regions with shallow clouds also have enhanced low level reflectivity, matching the higher rainfall rates in Figure 3b. This process was not repeated for clear air regions, as the TDR would have no precipitation particles to sense.

Overall, TDR CFAD results agree well with flight level w and SFMR rainfall distributions. Both CFAD and flight level w plots indicate enhanced low level updrafts in convective regions, and both high SFMR rainfall rates and high CFAD reflectivity are more commonly found in regions with active low level convection. These tests confirm the effectiveness of the CRL classification algorithm, and they reveal the important kinematic differences between stratiform and convective rainband sectors.

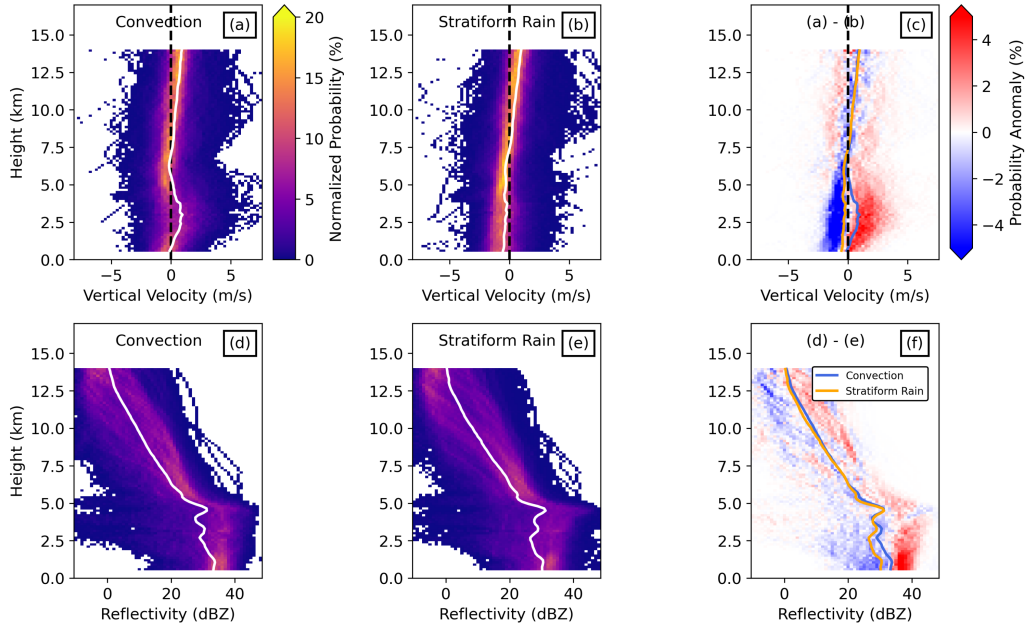


Figure 3.4: CFADs of TDR vertical velocity (a-c) and TDR reflectivity (d-f) for regions classified by the CRL as convection (a, d), stratiform rain (b, e), and convection minus stratiform rain (c, f). Mean CFAD values at each height are displayed as white lines in subplots (a-b, d-e) and in color for (c, f). A height bin of .15 km is used for all tests. Vertical velocity and reflectivity bin sizes are .25 m/s and 1 dBZ, respectively. Data below .5 km and above 14 km are removed due to small sample sizes and high noise. Black vertical lines in (a-c) denote a vertical velocity of 0 m/s.

3.4.4 CRL Cloud Classification Statistics

Having shown that CRL cloud classifications possess unique kinematic properties, statistics for convective and shallow clouds can be calculated. The following cloud width statistics account for cloud features ranging from small cells to large, cumulus congestus complexes (Figure 5a). The convective distribution has a mean value of 5.1 km and a mode of .5 km. This suggests that most convective clouds are small and that large convective complexes are outliers. Shallow cloud widths follow a similar negative exponential distribution as the convective clouds, but they have a less pronounced distribution tail, indicating that more shallow clouds have narrower widths than convection.

The spacing between convective regions also has a negative exponential distribution (Figure 5b). The mean spacing is 8.9 km, and the mode is for spacings smaller than 2 km. This suggests that

most convective complexes are separated by small distances, like small gaps generated by convective downdrafts. Shallow clouds have more small gaps and relatively fewer large gaps compared to convective cells.

A non-normal height distribution emerges for shallow clouds (Figure 5c). There is a peak at 750m, a constant distribution from 1100m to 2000m, and a linear decrease in shallow clouds up to 3000m. The peak at 750m is likely generated by boundary layer clouds, as this height matches typical TC boundary layer height metrics [Zhang et al., 2011b]. The tails around the 750m peak hint at the large spread in observed TC boundary layer heights [Zhang et al., 2013]. Heights above 1100m are likely from shallow clouds mixing upwards from the boundary layer, providing an important source of moisture for convective initiation and sustenance [Wang, 2014]. Height distributions are not calculated for convective clouds because many of these cells extend past the P-3 flight height and our observational range.

These are important details when considering the appropriate horizontal resolution for modeling TC rainband convective clouds. These distributions show that while standard horizontal resolutions of 1 km to 4 km found in operational dynamical TC models can capture mesoscale complexes, they cannot resolve the smaller, more common convective features observed here [Bryan et al., 2003, Jin et al., 2022, Murray et al., 2024].

The prevalence of convective, stratiform, and clear air regions varies greatly between flight legs (Figure 5d). For instance, one flight leg contains almost 100% stratiform rainfall, while a different flight leg contains nearly 0% stratiform rain. In the mean (Figure 5d, black stars), stratiform regions are most common, while significant areas of convection and clear air are still present. Statistically significant differences exist between the three groups (Kruskal-Wallis $p < .0001$). A Kruskal-Wallis H Test is used to determine if collections of distributions significantly differ from one another, as it is similar to the one-way ANOVA test but is non-parametric. Pairwise Dunn's Tests are conducted to determine significant differences between every combination of flight leg partition. All pairs are found to be statistically significantly different from one another (Dunn's Test $p < .005$).

The mean values for convective and stratiform distributions (black stars) are similar to the

median flight leg values (center line in the box plot), showing that individual legs are not biasing the distributions. For clear air, however, the mean value is much higher than the median for each flight leg, creating a non-normal distribution. This suggests that only a few cases have a substantial amount of clear air, and this biases the distribution mean towards higher clear air percentages.

It is important to note that our results only collect data along radial legs through the TC rather than covering the full areal swath of the TC. Therefore, clear air regions, which are more often found in the outer TC rainbands, would likely have larger spatial coverage compared to rainband convection and stratiform rain if they were sampled completely, rather than along individual paths through the TC [Hence and Houze, 2012]. Additionally, the P-3 aircraft typically avoids flying through the strongest convective cells, potentially decreasing flight leg convection percentages.

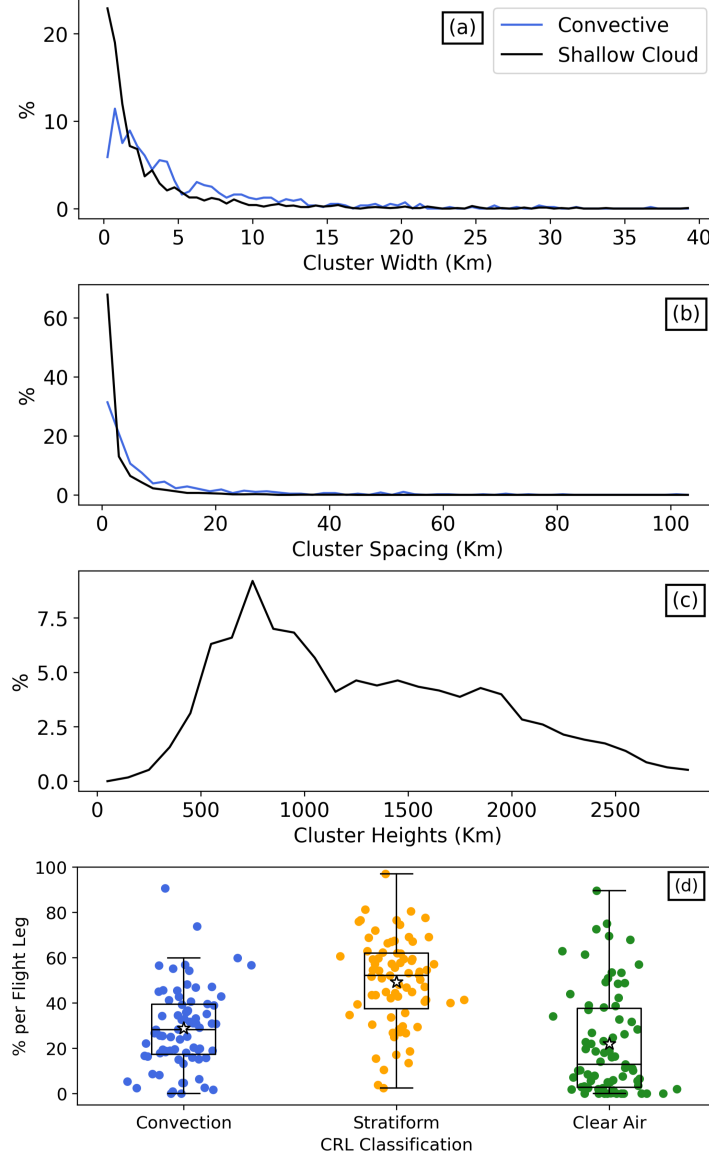


Figure 3.5: Distributions of convective and shallow cloud region widths (a) and spacings (b) from all observed TC rainbands. (c) Distributions of shallow cloud heights only from all observed TC rainbands. (d) Box and whisker plots of convective, stratiform, and clear air coverage in the TC rainbands. Each scatter point represents the percentage from one radial leg. Percentages of convection, stratiform rain, and clear air sum to 100% for each flight leg. The star symbolizes the mean for data not separated by flight leg, the horizontal black line represents the median for data separated by flight leg, the box edges are the interquartile ranges (IQR, Q1 and Q3) for data separated by flight leg, and the whiskers show the furthest point within 1.5 times the IQR from Q1 and Q3.

3.5 TC Rainband Asymmetries

3.5.1 Differences between Flight Legs

After partitioning the distributions of convective, stratiform rainfall, and clear air coverages by environmental shear quadrant, important TC asymmetries become evident (Figure 6). The ‘All’ distribution for each classification is reproduced from Figure 5d for clarity. In the following paragraphs, shear quadrant relationships are first identified for the three classifications, and then the impact of weak versus moderate shear strength is discussed.

Looking at the convective asymmetries (Figure 6a), the DL quadrant has the largest percentage of convective coverage with a median value of 38.7%. The DR, UL, and UR quadrants have median convective coverages of 31.3%, 22.7%, and 17.4%, respectively. These values are collectively statistically significantly different from one another (Kruskal-Wallis $p < 0.006$), and the DL and UR quadrants are statistically significantly different through pairwise tests (Dunn’s Test $p = .0008$). While these statistically significant relationships emerge, there is still high variability from flight leg to flight leg. The high proportion of downshear low level convection is physically reasonable, as this is where TC convection typically matures [Hence and Houze, 2012]. This convection is understood to collapse and reach a minimum upshear [Barron et al., 2022], which is consistent with our findings.

The DL and UL quadrants have the highest proportions of stratiform rainfall, while the UR quadrant has the smallest amount (Figure 6b). While these quadrant differences are not statistically significantly different from one another because of limited sample sizes (Kruskal-Wallis $p = 0.128$), they still illuminate important TC structural differences. The enhanced stratiform rainfall in the UL quadrant is symbolic of the decaying convective cells often found here [Didlake and Houze, 2013a]. The larger values found in the DL quadrant suggests that convective decay begins in the DL quadrant while still maintaining the highest proportion of active convection. DR and UR quadrants have relatively limited stratiform precipitation, as these quadrants are most associated with convective initiation.

The UR rainbands have the largest percentages of clear air per flight leg, while the DL rainbands have the smallest percentages (Figure 6c). The quadrants are collectively statistically significantly different (Kruskal-Wallis $p < 0.0005$), with statistically significant pairwise differences between the DR and DL quadrants (Dunn's Test $p < .002$) and the DL and UR quadrants (Dunn's Test $p = .0005$). These results match prior work, as the UR quadrant typically has a few initiating convective cells mostly surrounded by clear air [Hence and Houze, 2012]. Clear air decreases in the DR and DL quadrants as convection develops, and clear air increases again in the UL quadrant as convection collapses and stratiform rain sectors begin to clear.

Important variations in rainband convective, stratiform rainfall, and clear air coverages are driven by the strength of the environmental shear (Figure 6). Data from all shear quadrants show that moderate shear cases have 9.6% more convective coverage than for weak shear cases (Figure 6a). This suggests that shear-based convective enhancement mechanisms, including reductions in vortex tilt and strong upper to mid-level outflow shielding the vortex, enhance rainband convection [Fischer et al., 2023, Rios-Berrios et al., 2024, Wadler et al., 2021]. The DL quadrant sees an 18.4% increase in convection under moderate shear versus low shear cases. Since the DL quadrant already contains the most convection, this increase under enhanced shear ultimately enhances TC structural asymmetries.

The high variability in UR stratiform precipitation is driven by environmental wind shear (Figure 6b). Moderate shear UR cases have only 27.6% rainfall coverage compared to 59.1% coverage under low shear. This relationship supports the idea that enhanced environmental shear drives TC asymmetries, as UR convection and stratiform rainfall is reduced under such conditions.

Furthermore, both DL and UL quadrants have less clear air under moderate shear, while the UR quadrant has much more clear air coverage during moderate shear (Figure 6c). Changes are the largest for the UR quadrant, with clear air coverages of 23.4% for low shear versus the 55.0% coverage found for moderate shear. The far higher amounts of UR clear air under moderate shear compensate for the quadrant's limited stratiform coverage under the same conditions.

Overall, the DL and UR quadrants are the most sensitive to changes in environmental shear

strength. Moderate shear increases DL convection while limiting the ability of stratiform rain to wrap from the UL quadrant into the UR quadrant, increasing clear air coverage there. The net effect of these processes is to increase low level TC cloud and rainfall asymmetries [Rios-Berrios et al., 2024].

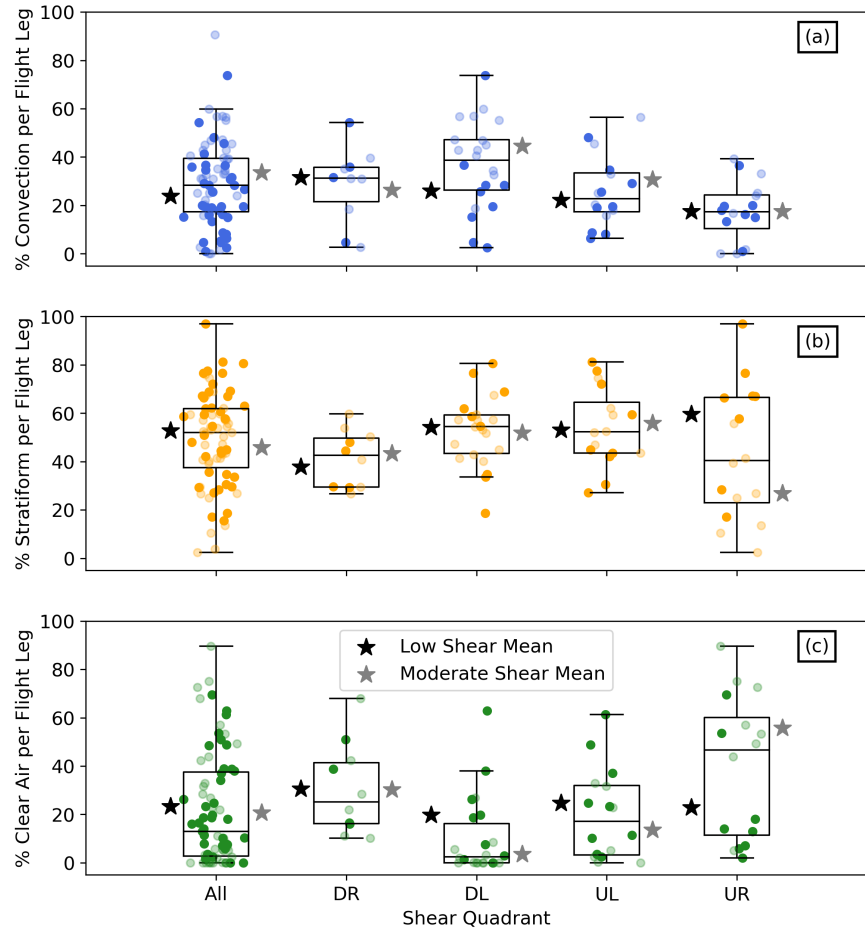


Figure 3.6: Box and whisker plots of TC rainband convective (a), rainfall (b), and clear air (c) distributions for all available rainbands and for the four different shear quadrants. Some Cat. 1+ strength legs do not have the necessary information to assign them a shear quadrant- these cases are still included in the “All” distributions. Box, whisker, and median definitions are the same as those described in Figure 3.5’s caption. Black (gray) stars represent low (moderate) shear separated by a shear magnitude threshold of 10.34 kt. Darker (lighter) scatter points represent individual flight legs experiencing low (moderate) shear.

3.5.2 Differences by Distance from the TC Center

Next, shear quadrant asymmetry tests are expanded to view radial differences in TC structures (Figure 7). For these tests, all available flight leg data are used rather than limiting our analysis to the TC rainband. Looking at shear driven convective asymmetries across all quadrants (Figure 7a), a typical TC structure emerges. In the TC eye, convective probabilities are low, as the strong temperature inversion present here caps most convective growth. Some shallow convection still forms in the TC eye, consistent with recent studies [Hirano et al., 2022, Murray et al., 2024].

In the TC rainbands for all cases, convective probabilities decrease towards higher r^* values. The DL quadrant has enhanced convection throughout the inner and outer rainbands, matching Figure 6a. While the UL quadrant experiences robust eyewall convection, its rainband convection is limited, suggesting that convective dissipation begins in the rainbands before spreading towards the eyewall. The UR quadrant sees the lowest percentages of inner core convection.

Similar relationships emerge for stratiform probabilities (Figure 7b). In the TC eye, the probability of identifying stratiform regions is low at roughly 20%. In the TC eyewall, only the UR quadrant has a significant stratiform rainfall peak at $r^*=.8$ from the weakened eyewall convection often found there. Stratiform rainfall in the TC rainbands has important shear quadrant differences, as from $r^*=2$ to $r^*=5$, the UL and DL quadrants have enhanced precipitation, matching the results from Figure 6b.

Clear air regions are elevated in the TC eye, with a mean value around 60% and no relationship with shear quadrant (Figure 7c). The UR eyewall has slightly more clear air present, but this is a relatively rare state. Clear air probabilities increase as radial distance increases and significant shear quadrant dependencies are present. The DL quadrant maintains clear air probabilities below 10% throughout almost all of the rainband. The UL quadrant has low clear air percentages close to $r^*=2$, but they increase towards higher radial distances. The right of shear quadrants possess enhanced clear air percentages, especially in the outer rainbands.

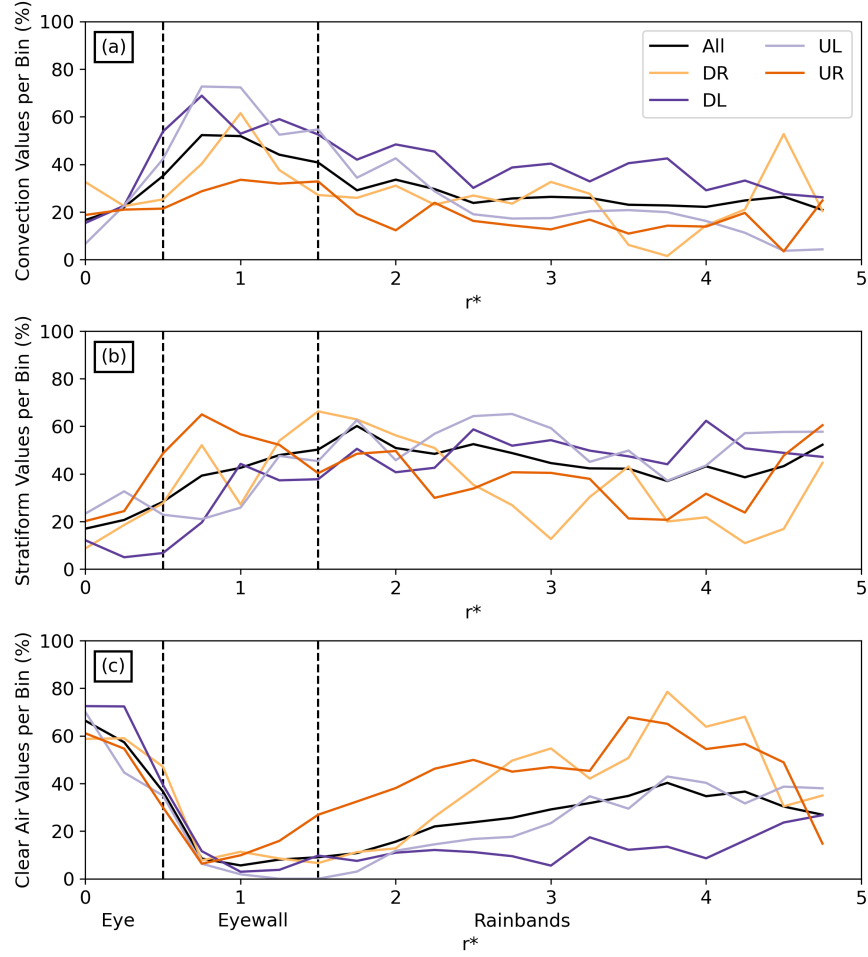


Figure 3.7: Normalized plots of TC structure using CRL cloud and rainfall classifications. Each line represents the probability of detecting convection (a), stratiform rain (b), and clear air (c). This is done at each radial distance r^* , which represents the normalized distance to the radius of maximum winds for individual flight legs. Rough estimates for TC eye, eyewall, and rainband limits are provided for context. Probabilities are calculated for all available flight legs, and for each of the four shear quadrants individually.

3.5.3 Kinematic Drivers of Rainband Asymmetries

Composites of TDR reflectivity and wind data for each environmental shear quadrant provide context for the low level convective, stratiform, and clear air differences detected by the CRL (Figure 8). TDR reflectivity is maximized in the DL and UL rainbands (Figure 8a, 8c), matching the enhanced stratiform rainfall found in these quadrants. The right of shear quadrants have relatively weaker radar reflectivity values (figure 8b, 8d).

Differences in rainband radial and vertical winds drive the convective asymmetries seen by the CRL (Figure 8e-h). The DR quadrant has the deepest radial inflow layer with a height above 4 km in the outer rainbands [Barron et al., 2022, Shimada et al., 2024], and the DL quadrant has the strongest inflow values out of the four regions. This enhanced downshear inflow provides a favorable environment for convective development through increased temperature and moisture fluxes [Chen et al., 2021b], supporting the convective initiation and maturation seen by the CRL here [Reasor et al., 2013]. The upshear quadrants, in contrast, have weak and shallow inflow layers capped by low level outflow [Reasor et al., 2013, Zhang et al., 2013]. This weak inflow leads to the collapse of UL rainband convection and the high amount of UR clear air, both of which were observed by the CRL.

DL and UL quadrants both possess the strongest eyewall updrafts (figure 8e, 8g), matching the enhanced eyewall convection seen here in Figure 7. The right of shear eyewalls, meanwhile, have weaker updrafts. UR eyewall updrafts peak in the lowest 2 km, suggesting that convection is just beginning to initiate, while DR eyewalls have peak values between 2 km and 4 km, suggesting that convection is deepening.

Midlevel rainband subsidence is diagnosed in all shear quadrants from 7 km to 5 km heights, which acts as a cap on deep rainband convection [Hence and Houze, 2012]. This midlevel convergence creates the rainband's melting layer and stratiform precipitation [Houze, 1997]. At low levels, most rainband regions have a mean vertical velocity of 0 m/s. The fewest low level downdrafts occur DR, where rainband convection strengthens. The UL quadrant has the most low level downdrafts, consistent with the high levels of stratiform precipitation seen here.

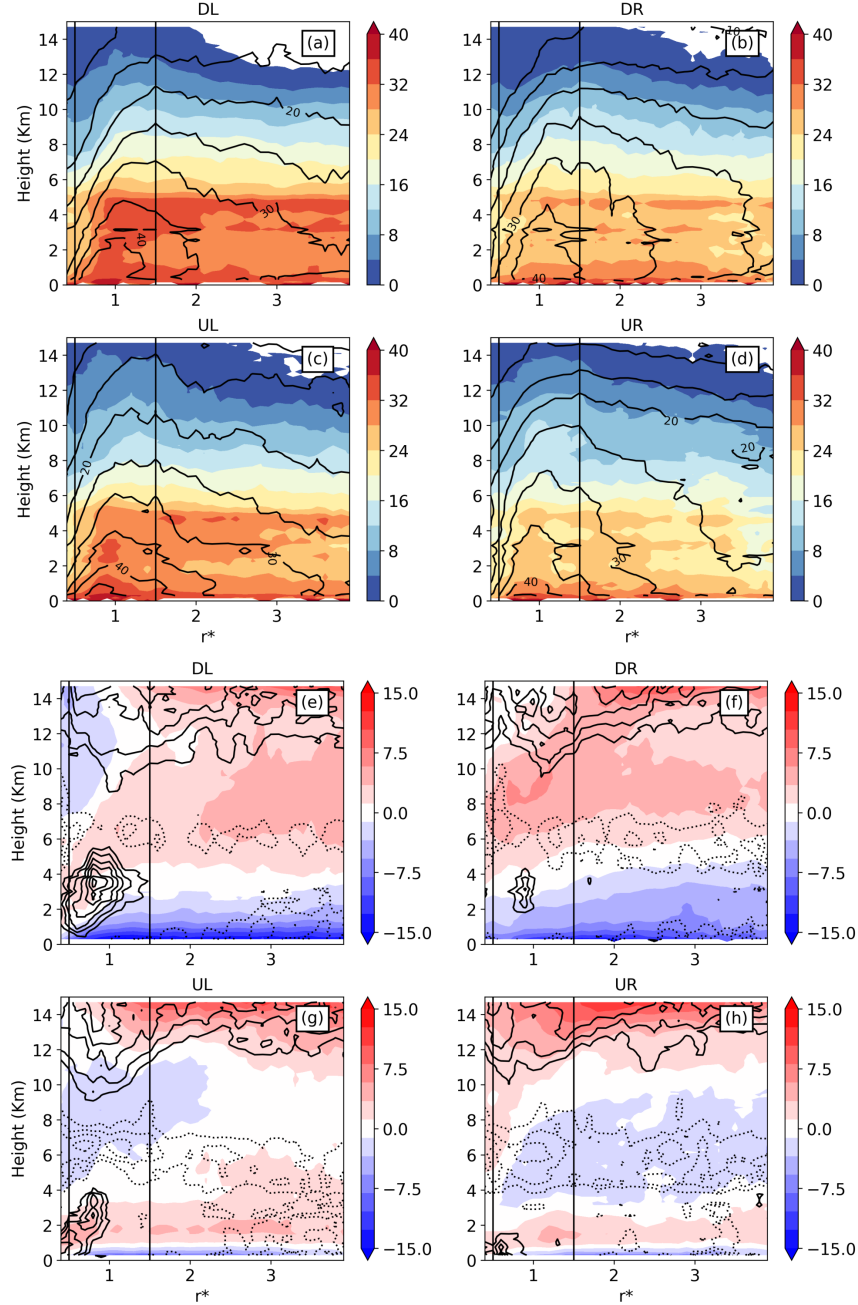


Figure 3.8: Environmental shear-relative composites of TDR profile data from hurricane strength TCs. (a-d) Composites of TDR reflectivity (shading, dBZ) and tangential wind speed (black contours every 5 m/s). (e-h) Composites of TDR radial wind (shading, m/s) and vertical wind (black contours every .2 m/s. Solid lines are positive, dashed lines are negative). Vertical black lines denote the estimated edges between the TC eye, eyewall, and rainbands shown in Figure 3.7.

3.5.4 Rainband Asymmetries: Example Flight Legs

Example flight legs were taken from TC Sam to illustrate the mean cloud, precipitation, and kinematic properties present in each environmental shear quadrant (Figure 9). In the DL quadrant example, many inner and outer core convective cells are identified in the CRL cross section, and stratiform rainfall fills much of the outer rainband (Figure 9a). Across all DL flight legs, more moderate and strong updrafts are present (Figure 9a), providing support for the extensive convection seen across these cases (Figure 6). This region has the most convection, plentiful stratiform rainfall, and the least clear air across all flight legs (Figure 7). As environmental shear increases, DL convection increases and its clear air coverage decreases due to an enhancement of TC asymmetries. These properties are supported by enhanced radial inflow and moisture generation in the DL boundary layer (Figure 8e).

In the UL rainband example, the CRL shows very few low level convective cells, especially in the outer core (Figure 9b). This matches our statistical results, underscoring how the UL rainband mostly contains decaying convection transitioning into stratiform rainfall (Figure 6). The UL rainband experiences enhanced mean downdrafts and weaker, shallow radial inflow (Figure 8g), stifling convective development and promoting stratiform rainfall.

The example UR quadrant rainband displays limited rainband extent, few convective cells above 1.5 km height, and clear air dominates the outer portion of the rainband (Figure 9c). The vertical velocity distribution for all UR flight legs shows that far fewer updrafts are detected compared to all legs (Figure 9c). Across all cases, UR rainbands contain the least convection, limited stratiform rainfall, and more clear air (Figure 7). The UR quadrant contains less stratiform rainfall and more clear air as environmental shear strength and TC asymmetries increase (Figure 6b, 6c).

In the DR rainband, the CRL cross section example shows that low level convection is developing in a region shrouded by stratiform precipitation from above (Figure 9d). Across all legs, the DR quadrant has enhanced convection and clear air percentages (Figure 6a, 6c), suggesting that this quadrant is usually composed of intensifying low level convective cells. This developing

convection is supported by strong, deep radial inflow and few rainband downdrafts (Figure 8f).

These results use CRL backscattered power data to reach these conclusions, allowing us to resolve low level cloud information for the first time, rather than using TDR reflectivity as a proxy for convection. Our results agree with the literature on TC rainband asymmetries [Barron et al., 2022, Didlake and Houze, 2013a,b, Hence and Houze, 2012, Wadler et al., 2022, 2023a], and they provide new statistics essential to understanding low level convective cell properties.

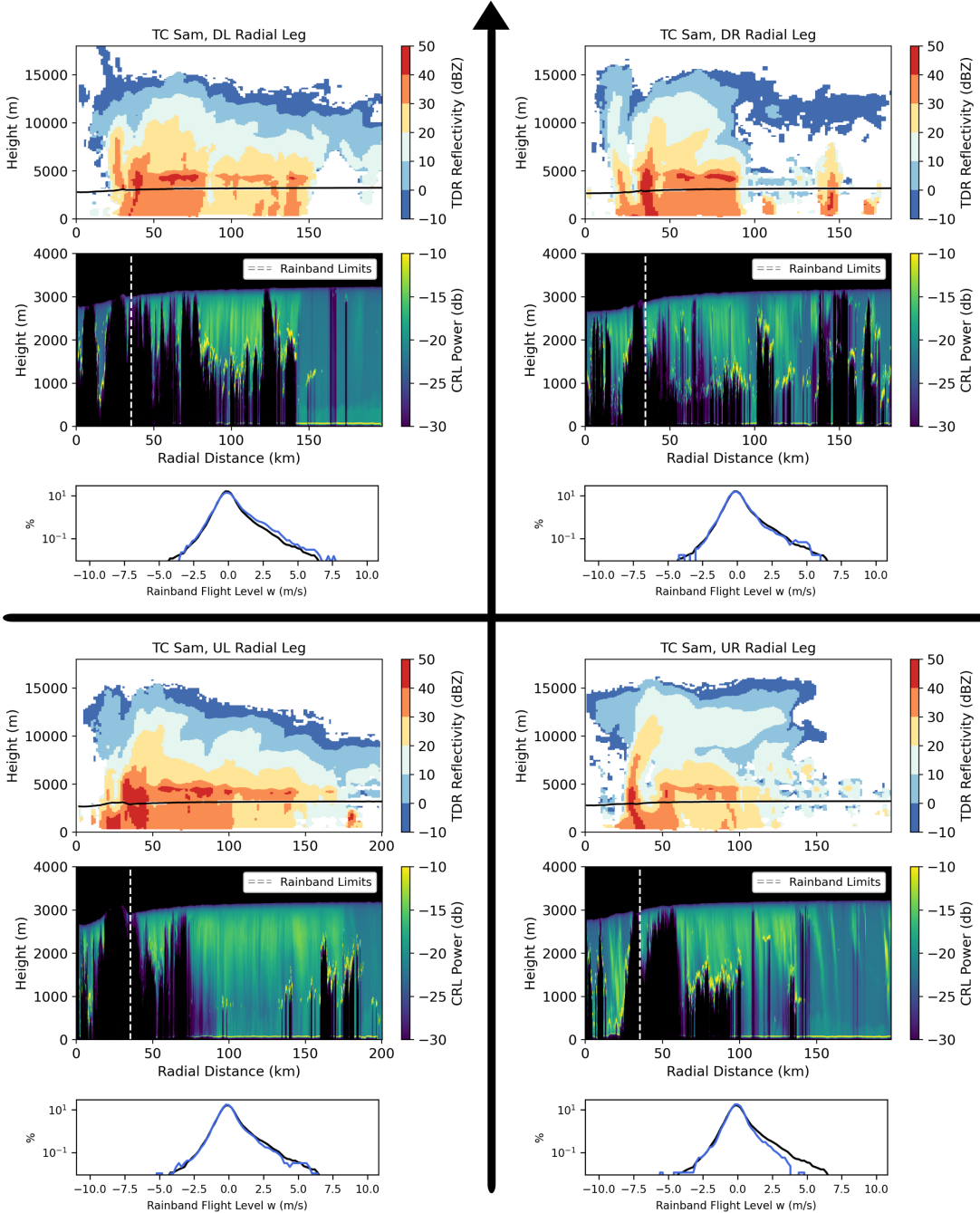


Figure 3.9: Top panels: TDR reflectivity cross sections from flight legs representative of each environmental shear quadrant's mean properties. Middle panels: corresponding CRL backscattered power cross sections. The DL and UR plots are the same as those in Figure 2. Bottom panels: flight level vertical velocity distributions from all rainbands (black line) and from just the selected shear quadrant (blue line).

3.6 Conclusion

This paper unveils distinct properties of low level cloud, rainfall, and clear air regions throughout the TC rainbands for the first time. To do so, a new classification algorithm is harnessed to precisely separate features found in CRL backscattered power cross sections. This paper expands upon traditional TDR observations of the TC rainband, which often portrays rainband convection as broad regions of high reflectivity, while the CRL resolves individual convective cells embedded within these regions. The CRL also resolves boundary layer clouds completely overlooked by the TDR. This work links low-level clouds to TC kinematics, captures the horizontal scales of convective and shallow clouds, and investigates TC cloud structure asymmetries.

While precipitation classifications can be made using TDR reflectivity data [Rogers et al., 2020], a case study of TC Sam (2021) shows that CRL backscattered power provide additional cloud information not resolved by the TDR. These CRL classifications have unique flight level vertical wind, SFMR surface rainfall rate, TDR vertical wind, and TDR reflectivity distributions. Furthermore, while convective complexes sometimes have mesoscale widths and spacings, many structures are on the convective scale with structures often less than 1 km wide and cell spacings smaller than 2 km. Low level shallow cloud widths and spacings are even narrower than the convective features diagnosed above, and shallow cloud height statistics show how boundary layer clouds mix upwards and above the layer. These results suggest that fine scale operational and research TC models are required to capture the unique kinematic properties of low level rainband clouds [Bryan et al., 2003, Jin et al., 2022].

In the future, the collection of more low level cloud top information using the CRL should be prioritized. Additional flight legs, especially into hurricane strength systems experiencing strong environmental wind shear or into weakening systems would better balance the flight leg distributions displayed in Figure 1. This would allow us to partition flight legs by TC intensification rate, possibly illuminating new physical mechanisms important for slow and rapid TC intensification [Guimond et al., 2016, Majumdar et al., 2023a, Tao and Jiang, 2015, Zhang et al., 2022a]. Additional CRL

deployments would collect more temperature and moisture profiles in the inner and outer cores, opening more direct and indirect avenues towards model improvement [Christophersen et al., 2022, Ditchek et al., 2023, Zhang et al., 2012].

The CRL database can be used to investigate other vortex processes. CRL classifications from weak TCs could illuminate TC genesis and early stage intensification processes [Alvey et al., 2020, 2022, Rogers et al., 2020, Zawislak and Zipser, 2014]. The CRL would provide a new perspective on the low level cloud and precipitation fields in these developing systems. CRL cloud and aerosol measurements could also be used to find the boundary layer height, complementing current kinematic and thermodynamic definitions [Zhang et al., 2013].

Finally, these observational rainband cloud and precipitation statistics should be compared to model forecasts. Comparisons should be made across scales to determine if low level cloud representations differ across large eddy simulations (LESs) (Chen et al. 2021a; Gomez et al. 2025), forecasts with resolutions in the “gray zone” (Chen et al. 2021c), and mesoscale models (Alaka et al. 2024; Komaromi et al. 2021). Different model parameterizations of convection and low level mixing could modify the TC boundary layer and impact TC intensity (Chen et al. 2021b; Houze 2010; Powell 1990b; Yu et al. 2018), making these observations an essential reference point when tuning a particular TC model.

Chapter 4

AN OBSERVATION-MODEL COMPARISON FRAMEWORK FOR DIAGNOSING TROPICAL CYCLONE THERMODYNAMIC CHANGE: APPLICATION TO HURRICANE SAM (2021)

Preface

This chapter is currently under revision and should be cited as below:

Ethan J. Murray, Jon Moskaitis, James Doyle, Kristopher B. Karnauskas, Zhien Wang, and Jun A. Zhang. An observation-model intercomparison framework for diagnosing tropical cyclone thermodynamic change: Application to hurricane sam (2021). **Monthly Weather Review**, in revision, 2025b

Abstract

Biases in tropical cyclone model forecasts impact track, intensity, and structural predictions. Yet, not all of these biases can be assessed using traditional comparisons with observations. This paper fills this research gap by introducing a new model evaluation framework that compares single forecasts to aircraft data from individual flights. Measurements from the novel compact Raman lidar are supplemented by dropsonde and tail Doppler radar data to explore how low-level tropical cyclone kinematics and thermodynamics evolve, particularly in the atmospheric boundary layer. The compact Raman lidar provides extensive and unique thermodynamic data in the tropical cyclone eye and rainbands. As a demonstration, observations are compared to short lead time COAMPS-TC forecasts of Hurricane Sam (2021) over three sampling periods to diagnose model biases.

Two important low-level biases consistently appear: the modeled rainband atmospheric boundary layer has a positive moisture bias, and the central warm core region has a cold bias. Despite these consistent thermodynamic differences, Sam's primary and secondary circulations vary between flights, suggesting that mean tropical cyclone kinematics alone do not drive these temperature and moisture anomalies. This analysis framework provides an avenue for future model improvement via atmospheric boundary layer scheme adjustments.

Significance Statement

Tropical cyclones rely on the transfer of heat and moisture from the ocean to the lower atmosphere to maintain their structure and intensity. Despite the importance of low-level thermodynamics, these fields are poorly constrained in tropical cyclone models. This study uses a new methodology to compare unique aircraft measurements of temperature and moisture with model forecasts for one storm. Key differences in the model with respect to observations are found, including increased low-level moisture and colder temperatures in the eye of the storm. These model biases alter the characteristics of the simulated storm, partially explaining intensity forecast errors. In the future, if we can correct these thermodynamic biases by improving model physics, a more accurate depiction of tropical cyclones could be achieved.

4.1 Introduction

A better understanding of the physical processes driving tropical cyclone (TC) intensity change remains a fundamental research priority [Hendricks, 2012, Zawislak et al., 2022]. Intensity change processes are dependent on atmospheric boundary layer (ABL) kinematics and thermodynamics, which are influenced by the TC's convective structure [Chen et al., 2023, Rogers, 2021] and by the nearby atmospheric and oceanic environments [Chen et al., 2021b, Rios-Berrios et al., 2024, Wadler et al., 2023b]. These are known as internally and externally driven intensity change processes.

A principal internal intensification process is the generation and maintenance of eyewall

convection. Intensifying TCs often contain deep, coherent convective towers near the radius of maximum wind (RMW) [Guimond et al., 2016, Zhang et al., 2022a]. These eyewall updrafts rely on heat and moisture concentrated in the ABL. Thus, the shallow ABL region drives TC spinup by providing energy to deep convection. Meanwhile, rainband downdrafts or a dry TC environment can ventilate the ABL with low entropy air (i.e., low equivalent potential temperature, θ_e) and hinder TC inner core convection [Alland et al., 2021a, Tang and Emanuel, 2010, Powell, 1990, Wadler et al., 2022]. These examples demonstrate how the ABL is essential in both TC intensification and weakening processes.

Modeling ABL kinematics and thermodynamics using operational simulations is a method to understand its importance for TC intensity change [Ahern et al., 2019, 2021]. Operational TC models leverage ABL parameterizations to speed up computations and effectively simulate TC structure [Stull, 1988]. Yet, model forecasts are sensitive to ABL scheme changes with downstream effects on the model's inflow layer height, low-level convergence, tangential winds, and thermodynamic fluxes [Gopalakrishnan et al., 2013, Takahashi et al., 2024, Zhang et al., 2015]. This sensitivity to differences in ABL schemes warrants detailed evaluation studies for all operational TC models.

In one such evaluation study, using different ABL schemes in the Weather Research and Forecasting Model (WRF, Skamarock et al. [2019]) meaningfully changes the TC ABL radial inflow, azimuthal winds, and low-level thermodynamics because of different surface frictional effects from each scheme [Nolan et al., 2009b]. Decreasing the vertical eddy diffusivity in the Hurricane Weather Research and Forecasting Model (HWRF, Alaka et al. [2024]) results in stronger inflow, enhanced eyewall convergence, stronger updrafts, a more symmetric TC, and increased intensity [Zhang et al., 2015, 2017b, Zhang and Rogers, 2019]. Other common ABL parameterization changes include adjusting the vertical moisture diffusivity parameter [Xu and Zhao, 2021], surface flux parameters [Ming and Zhang, 2016], and turbulence length scales [Bryan, 2012]. These studies all demonstrate the sensitivity of the TC ABL in operational models to the parameterization scheme used, and that changes to the same parameter in different models can lead to different simulation results.

To evaluate and improve upon these TC ABL parameterizations, modeled wind and thermo-

dynamic output is often compared to observational composites [Gopalakrishnan et al., 2021, Zhang et al., 2012]. These composites use radar [DesRosiers et al., 2023, Fischer et al., 2022, Rogers et al., 2012, Reasor et al., 2013], in-situ [Kossin and Eastin, 2001, Martinez et al., 2017], and dropsonde [Ahern et al., 2019, Wadler et al., 2022, Zhang et al., 2011b, 2013] data collected from many TCs to understand variations in ABL heights, precipitation strength, and other important features. These observational composites highlight mean TC structures well [Zhang et al., 2020], but they overlook key variations between storms, as many different cases are averaged together. This suggests the need for a new assessment framework focusing on individual TCs.

In this study, we examine ABL kinematics and thermodynamics using data from individual model runs and TC reconnaissance flights, rather than compositing many cases together. This allows for the identification of key ABL differences in single cases rather than smoothing differences across many cases. Forecasts from COAMPS-TC, the Navy's operational TC forecasting model, are used for these comparisons. Similar to operational TC models from NOAA like HWRF and the Hurricane Analysis and Forecast System (HAFS, Alvey et al. [2024]), COAMPS-TC is convection permitting and uses an ABL parameterization scheme to represent turbulent processes. A more detailed description of the COAMPS-TC model components used here is provided in the methods section.

To evaluate single, short lead time COAMPS-TC forecasts, aircraft observations from individual reconnaissance flights into TC Sam (2021) are used. Aircraft observations help to assess ABL parameterizations by providing targeted, high-resolution thermodynamic information to compare with model simulations. Current aircraft-based thermodynamic measurements mainly come from in-situ instruments, small unmanned aircraft systems (sUASs), and dropsondes [Rogers, 2021].

While in-situ data are abundant and have high temporal resolution, they are typically constrained to be above the ABL for flight safety precautions [Martinez et al., 2017, Zhang et al., 2009]. Recent deployments of the sUAS Coyote and Black Swift S0 into extreme TC environments like the eye-eyewall interface is an exciting, new research avenue, but their currently limited spatial sampling and sporadic use prevents us from creating comprehensive composites of TC boundary

layer thermodynamics [Chen et al., 2021a, Cione et al., 2020, Aberson et al., 2023].

Dropsondes have been a trusted thermodynamic measurement tool since their consistent introduction to aircraft operations in 1997 [Aberson et al., 2023, Hock and Franklin, 1999]. Recent data assimilation experiments confirm that assimilating dropsonde profiles into global and mesoscale models improves TC forecasts [Ditcheck and Sippel, 2023, Ditcheck et al., 2023, Sippel et al., 2022]. Nevertheless, dropsonde measurements are limited, as only 10 to 30 dropsondes are normally deployed per NOAA P-3 or G-IV flight [Ditcheck and Sippel, 2023]. P-3 aircraft typically deploy dropsondes in the TC center, eyewall, flight radial midpoint, and flight radial end point, leaving significant measurement gaps in the TC rainbands [Ditcheck and Sippel, 2023, Rogers et al., 2015, Stern and Bryan, 2018]. We argue that current dropsonde measurements are insufficient to capture ABL thermodynamic variability within individual TCs, suggesting that additional observations are needed.

In this paper, we utilize new data from the compact Raman lidar (CRL) along with standard aircraft measurements to implement our observation-model comparison framework. This framework analyzes single TC cases, rather than multiple TC composites, with the goal of identifying model biases to guide ABL physics improvement. The CRL is crucial in this effort, as it collects thousands of vertical profiles of temperature, water vapor, and rainfall in non-cloudy TC regions during a single P-3 flight. CRL thermodynamic measurements synergize well with dropsonde data, as a majority of CRL vertical profiles are gathered in the rainbands, a region of poor dropsonde coverage. The CRL was deployed on the NOAA P-3 (N42) during the 2021 and 2022 hurricane seasons. CRL data allow for the creation of single-day composites, even for cases that were previously limited by dropsonde coverage.

The observational and model datasets used in this paper are described in Section 2. In Section 3, the methods used to bias correct CRL data, virtually sample the COAMPS-TC model domain, and calculate composites are outlined. Section 4 provides an overview of North Atlantic Hurricane Sam (2021), the TC chosen to demonstrate this new model evaluation framework. Sam is an ideal case study because of its high intensity and considerable CRL data coverage from three

reconnaissance missions [Pasch and Roberts, 2022].

Full-TC (axisymmetric) analysis and analysis of flight legs sorted by environmental shear direction (asymmetric analysis) are presented in Section 5. Section 6 puts into context the main findings of this paper, summarizes the work and suggests future research directions for improving TC forecasts via aircraft observations. In sum, this work leverages high-resolution CRL thermodynamic data to identify two COAMPS-TC biases in TC Sam: a cold bias in the low-level TC eye, and a moist bias in the ABL. Results from this study suggest that making single day observation-model comparisons is a valuable framework for future model bias evaluation and correction.

4.2 Datasets

4.2.1 COAMPS-TC Model Configuration

The Coupled Ocean-Atmosphere Mesoscale Prediction System- Tropical Cyclone (COAMPS-TC) is a regional dynamical TC prediction model. The model is developed by the U.S. Naval Research Laboratory and run operationally by the Fleet Numerical Meteorology and Oceanography Center. COAMPS-TC has similar or better forecast performance compared to other operational deterministic regional dynamical TC models [Doyle et al., 2014], and as such is utilized as forecast guidance by the National Hurricane Center and Joint Typhoon Warning Center [Cangialosi et al., 2024, Francis and Strahl, 2020].

This study used the operational COAMPS-TC model that was run during the 2024 TC season (v2024 COAMPS-TC). It employs a stationary, horizontal outer grid and two higher resolution, nested storm following inner grids. The fixed outer grid has 36 km horizontal grid spacing; the storm following inner grids have 12 km and 4 km grid spacing. Experimental runs of COAMPS-TC suggest that horizontal grid spacing is impactful on TC intensity forecasts and storm structure, with finer grid spacing better simulating spiral rainbands, strong updrafts, and the TC warm core [Jin et al., 2014, 2022]. As this study utilizes the coarser, operational 4 km inner-most grid, convective-scale cloud structures like secondary eyewalls may be missed [Jin et al., 2022]. Nevertheless, the

goal of this study is to evaluate operational COAMPS-TC forecasts, rather than research ones, so the 4-km resolution model is used here.

The model uses a vertically staggered grid with 40 sigma levels from 10 m (the lowest model level) to around 30 km (the highest model level). COAMPS-TC has finer vertical grid spacing in the boundary layer, which greatly benefits observation-model comparisons. Here we use GFS to provide initial and lateral boundary condition information to COAMPS-TC, which is known as the “CTCX” version of the model (as opposed to “COTC”, which uses NAVGEM as the parent global model).

The COAMPS-TC model parameterizations used in this study are generally as described in Komaromi et al. [2021]. Parameterization of deep convection in the outer two horizontal grids follows that in Kain and Fritsch [1993], while shallow convection is parameterized according to Tiedtke [1989]. Deep convection is not parameterized on the inner-most 4-km grid. Turbulent mixing within the boundary layer and within the free troposphere is parameterized using a 1.5-order closure scheme with turbulent kinetic energy as a prognostic variable. Two different vertical mixing length formulations are used; the buoyancy-based non-local Bougeault [1985] formulation is used throughout the free troposphere, but a mixing length following the Mellor and Yamada [1982] formulation is prescribed below 3 km (see Doyle et al. [2014] for further details). For strong TCs, 3D winds are initialized by removing TC winds from the GFS global initialization and replacing them with a modified, balanced Rankine vortex [Komaromi et al., 2021]. A 3D temperature field is then generated from this vortex using hydrostatic and gradient wind balance. For TCs weaker than 55 kt ($1 \text{ kt} \approx 0.51 \text{ m s}^{-1}$), the GFS representation of TC winds and temperature is left in COAMPS-TC, and no Rankine vortex is added. Regardless of the TC strength, moisture is initialized from GFS initial conditions. These ABL scheme and vortex initialization details have important implications for simulated TC kinematic and thermodynamic structure.

4.2.2 Compact Raman Lidar (CRL)

The CRL is a remote sensing instrument that measures aerosol, cloud, temperature, and moisture structures. This instrument was recently used to sample nine TCs during the 2021 and 2022 Atlantic hurricane seasons as part of the Office of Naval Research Tropical Cyclone Rapid Intensification (TCRI) and NOAA Advancing the Prediction of Hurricanes Experiment (APHEX) collaborative field program, which utilized one NOAA P-3 as an observing platform. As the NOAA P-3 traverses the TC, the downwards-pointing CRL continuously samples the atmosphere with a 354.7 nm pulse laser operating at 30 Hz. After collection, raw CRL measurements are integrated along the flight path to create cross sections with horizontal and vertical resolutions of 250 m and 6 m, respectively.

Due to the CRL laser's short wavelength, high concentration small cloud particles cause rapid CRL signal attenuation, while low concentration larger rainfall particles cause weak attenuation. Therefore, cloud tops can be differentiated from rainfall regions, providing a unique, detailed perspective on TC microphysical structure [Murray et al., 2024]. Additionally, in cloud free regions, the CRL can provide continuous profiles of rainfall intensity, moisture, and temperature. CRL rainfall power is proportional to rain drop concentrations and the square of their size, and they can be combined with concurrent P-3 tail Doppler radar (TDR) and Stepped Frequency Microwave Radiometer (SFMR) rainfall measurements to further quantify precipitation microphysics.

Water vapor mixing ratio (WVMR) values are derived from the ratio of the water vapor Raman scattering channel to the nitrogen channel after a calibration [Liu et al., 2014]. Atmospheric temperature is calculated via the ratio of the high J pure rotational Raman channel to the low J Raman channel, where J is the rotational quantum number. These Raman effects slightly shift the return wavelength of laser light, and the intensities of high J and low J pure rotational Raman scattering for nitrogen and oxygen gasses vary with atmospheric temperature differently. This provides an effective way for atmospheric temperature determination [Wu et al., 2016].

4.2.3 Tail Doppler Radar (TDR)

The TDR aboard the NOAA P-3 aircraft provides 3D wind velocity and reflectivity measurements throughout the TC inner core. Since the TDR is an X-band radar with a 3.2 cm beam wavelength, its signal can be quickly attenuated wherever precipitation scatterers are present in the TC inner core [Reasor et al., 2009]. Thus, the P-3 typically traverses the TC inner core multiple times at different flight azimuths to cover nearly the whole cyclone, creating single swath measurements along each flight leg and a merged analysis using all flight legs [Fischer et al., 2022].

For this work, TDR profile data (Level 2) are used to create tangential and radial wind speed composites [Lorsolo et al., 2010, Rogers et al., 2012, Zhang et al., 2022a], and TDR swath data (Level 3) are used for vertical wind speed composites [Fischer et al., 2022, Rogers et al., 2012]. TDR profile data are created from single radial passes through the TC center and have vertical and horizontal resolutions of 150 m and 1500 m, respectively. The high vertical resolution of profile data allows for more accurate sampling of ABL winds, particularly the radial inflow layer, which can be quite shallow [Rogers et al., 2012]. Furthermore, their azimuthal confinement to within 10 km of the flight path makes the synergy with CRL measurements feasible. TDR swath data, which have vertical and horizontal resolutions of 500 m and 2000 m, respectively, are used to sample TC vertical wind speeds, as profile vertical wind speeds show a negative bias, especially in the TC rainbands (Rogers et al. [2012], table 2). Swath data are resampled close to the flight azimuth to match profile observations while retaining their lower spatial resolution [Lorsolo et al., 2010, Zhang et al., 2022a].

4.2.4 Dropsondes

Dropsonde profiles were used as a thermodynamic ground truth in this study [Bell and Montgomery, 2008, Montgomery et al., 2014, Tang et al., 2024]. With a fall speed between $12\text{-}15 \text{ m s}^{-1}$ [Aberson et al., 2017, Hock and Franklin, 1999] and collection rates of 2 Hz for thermodynamic data and 4 Hz for wind velocity data [Aberson et al., 2023], these quantities are collected at roughly

6.75-m and 3.38-m intervals, respectively. This allows for easy comparison with CRL measurements after regridding dropsonde data to the CRL's vertical resolution of 6 m.

4.2.5 Comparison of Thermodynamic Data Coverage

Figure 4.1 demonstrates the enhanced spatial coverage of thermodynamic measurements when combining the CRL with traditional in-situ and dropsonde data. During this pass through the center of Hurricane Sam, dropsondes were released at the flight track center, TC eyewalls, radial midpoint, and radial endpoint (Fig. 4.1b, 4.1c). While these 11 total dropsonde profiles reveal general aspects of Hurricane Sam's structure, they lack the horizontal resolution to resolve essential thermodynamic ABL variations associated with kinematic mixing processes across different scales, especially in the outer rainbands.

This makes the nearly continuous thermodynamic coverage of the outer rainbands and TC eye by the CRL even more impactful (Fig. 4.1d, 4.1e). CRL measurements reveal convective-scale variations in temperature and moisture, which are not visible in dropsonde profiles, and allow for the calculation of more robust statistics for single TC cases. Nevertheless, due to signal attenuation, the CRL lacks measurements in the surface layer and lowest levels of the boundary layer (0-m to 150-m height) (Fig. 4.1d, Note 1) and in the cloudy eyewalls (Fig. 4.1d, Note 2). Dropsonde and in-situ data help fill these measurement gaps, stressing the importance of synergizing these datasets.

The large CRL observational cross sections can be compared to COAMPS-TC output, diagnosing important differences between the two (Fig. 4.1f, 4.1g). COAMPS-TC model output is sampled virtually along the real P-3 flight track, allowing for comparisons with observations that capture the proper TC asymmetries (Fig. 4.1a).

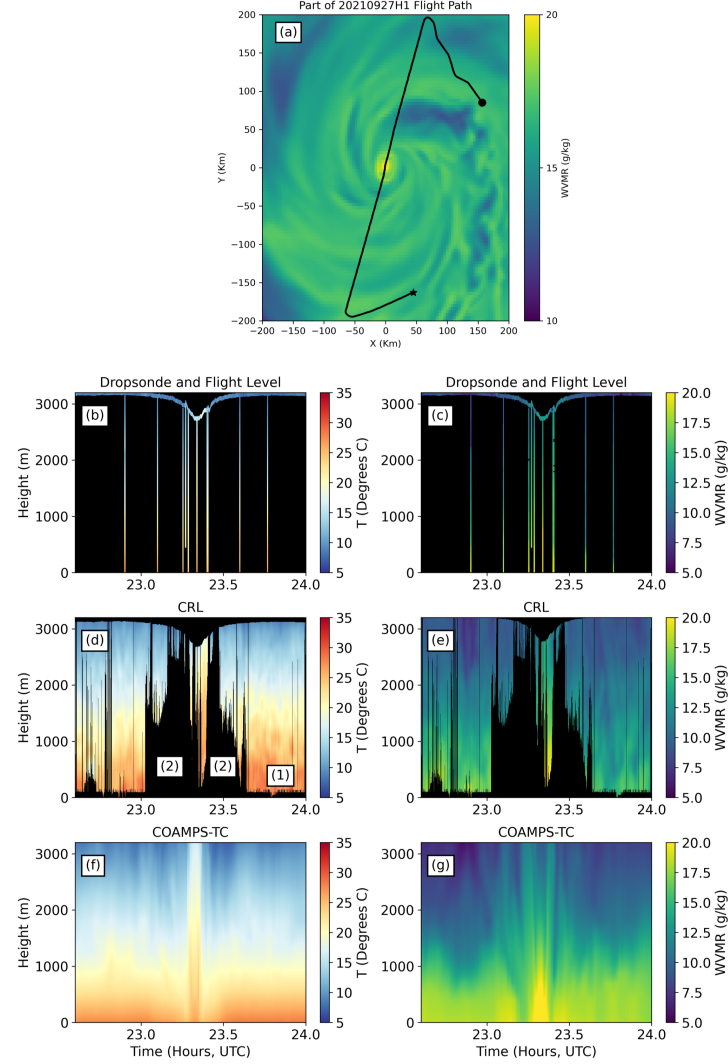


Figure 4.1: Plan and profile views of modeled and observed TC thermodynamics from one inner core pass through Hurricane Sam just before 0000 UTC 28 Sep 2021. The COAMPS-TC simulation was initialized on 1200 UTC 27 Sep 2021. (a) Plan view of ABL moisture in COAMPS-TC at 690 m ASL. The black line represents the real P-3 sampling flight path overlaying the modeled moisture field, the circle indicates the start of the flight cross section at 2236 UTC 27 Sep 2021, and the star represents the end of the sampled path at 0000 UTC 28 Sep 2021. TC Sam was at 105 kt intensity when sampled here, while its COAMPS-TC representation was at 120 kt intensity. Profile views of dropsonde and in-situ data (b-c), CRL data (d-e), and COAMPS-TC temperature and WVMR (f-g) values are provided. Dropsonde profiles are plotted as vertical lines at their release times. COAMPS-TC values are sampled along the flight track. Black regions represent observational gaps. For the CRL, these areas are associated with enhanced attenuation near the sea surface (1) and eyewall cloud tops (2) shown in (d).

4.3 Analysis Methods

4.3.1 CRL Bias Correction

Before comparing CRL data with COAMPS-TC model output, a simple bias correction is performed to bring CRL temperature data in line with dropsonde measurements. To facilitate these comparisons, columns of CRL data are matched with dropsonde data at their release locations. This sampling strategy is complicated by the tendency of dropsondes to drift cyclonically around the circulation center [Bell and Montgomery, 2008, Kopelman et al., 2024] while the CRL samples directly downwards. These spatial sampling differences could result in large measurement differences in the ABL for some cases.

However, these comparisons are reliable for a few reasons. Dropsonde paths typically show little to moderate radial drift, with only 7.1 km of drift at the 95th percentile of cases [Nguyen et al., 2019]. For our data, we decided to calculate mean drift, rather than the outliers, because there are far fewer dropsondes used in our study. For Sam's three flights, there is a higher mean drift distance of 9.8 km for dropsondes. This higher horizontal drift is caused by Sam's Cat. 3 to 4 winds and the enhanced number of dropsondes launched into the eyewall relative to typical P-3 missions. Splitting the TC into eye ($\text{distance to center} / \text{RMW} < 0.5$), eyewall ($0.5 \leq \text{distance to center} / \text{RMW} < 1.75$), and rainband ($1.75 \leq \text{distance to center} / \text{RMW}$), we find dropsonde drift errors for each region to be 2.35 km, 14.13 km, and 6.55 km, respectively. Due to cloud attenuation, little CRL data exist in the TC eyewall region where dropsonde drift is largest, so these large errors are avoided. Given that mean dropsonde drifts in the eye and rainbands across all flights are below the width of two COAMPS-TC grid cells, we assume that the impact of dropsonde drift on CRL comparisons is minimal, and that the two profiles are suitable for comparison.

Since CRL measurements within TCs are new and dropsondes are proven in-situ instruments, dropsonde profiles are regarded as the ground truth for CRL temperature bias corrections (Fig. 4.2 a-c). CRL warm biases vary from 1.40 °C to 2.45 °C per flight (Fig. 4.2 a-c, inset) for Hurricane Sam. These biases originate from different daily low J and high J channel overlap functions. This

requires an overlap correction for near range temperature measurements to quantify temperature calibration drift, due to variations in in-situ temperature measurements. One overlap correction was applied for temperature measurements across the entire hurricane season, yet there are unaccounted for day to day overlap differences, which lead to the biases shown in Fig 4.2. The daily biases from dropsonde comparisons are used to correct CRL temperature measurements for each flight day.

After correcting by this daily bias, remotely sensed CRL temperatures agree with in-situ dropsonde measurements. There are mean errors of 0.00 °C for all corrected CRL data and average standard deviations between the two temperature datasets are 3.22 °C for flight 20210926H1, 1.91 °C for flight 20210927H1, and 1.06 °C for flight 20210929H2. Spread in temperature biases is larger near the surface, where drifting dropsondes diverge further from stationary CRL profiles. This is especially true for flight 20210926H1, which has the highest mean dropsonde drift and temperature bias out of the three flights, as many dropsondes were launched in the TC eyewall, decreasing our sample of available CRL profiles for verification and increasing drift-related errors.

No similar correction is necessary for CRL WVMR measurements. The CRL's WVMR channel is very stable over time, and one calibration constant is used for the whole hurricane season. This is a known attribute of the CRL [Lin et al., 2021, Liu et al., 2014]. CRL moisture measurements are consistent with dropsonde profiles across all flights with mean errors per flight ranging from -0.07 g kg⁻¹ to 0.20 g kg⁻¹ (Fig. 4.2d-f). Outlier errors for flights 20210927H1 and 20210929H2 are from individual dropsondes passing close to an upright cloud boundary, which can cause biases in CRL water vapor returns. These outliers do not affect subsequent results.

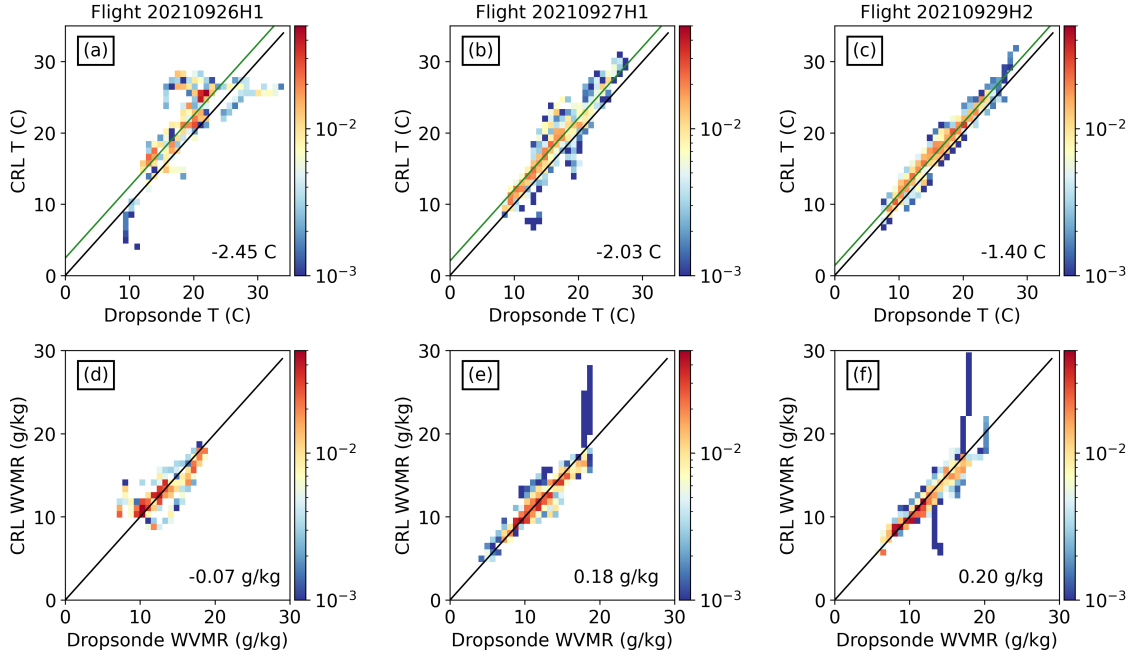


Figure 4.2: Heatmap plots comparing CRL and dropsonde temperature (top row) and WVMR (bottom row) measurements from Hurricane Sam for flights 20210926H1 (a, d), 20210927H1 (b, e), and 20210929H2 (c, f). Colorbars represent the normalized probability of paired values: all values per subplot sum to 1. Black lines represent a perfect, one-to-one match between datasets. Green lines found in (a-c) show the constant CRL temperature offsets used for correction. Offset values are listed in the bottom right corners of each subplot.

4.3.2 Observation and Model Matching Techniques

Due to differing TC center locations between observations and model forecasts, all data are converted to storm relative coordinates before comparison. Observational center fixes are determined using NOAA's 2-minute TC position estimate which includes flight-level center fixes and Best Tracks [Willoughby and Chelmow, 1982], while 6-hourly COAMPS-TC center fixes are generated using the GFDL vortex tracking algorithm [Marchok, 2021]. For each case, the nearest 6-hourly model output time is compared to the median time during P-3 observational collection. Short lead time forecasts are used for all three sampling periods, with lead times of 12 h, 12 h, and 30 h for flight comparisons on 26, 27, and 29 September 2021.

For this analysis, the COAMPS-TC model forecast data are sampled along the P-3 flight

track, mimicking real observational flight paths through the TC inner core and near environment (Fig. 4.1a). For each CRL column measurement, a corresponding column of COAMPS-TC data are taken from the nearest model grid cell. Model data are then vertically interpolated and gridded, allowing for daily composite comparisons with CRL thermodynamic data. A drawback of this sampling technique includes treating both modeled and observed TC structure as being fixed in time for the duration of the 4 h sampling period. Previous studies assume that dropsonde profiles collected over a few hours can show instantaneous TC structure [Tang et al., 2024], and this is the only way to directly compare daily flight observations to a model with 6-h output, so this method is used.

4.3.3 Single Day Compositing Methods

Vertical profile and radius-height compositing techniques are used to compare model outputs to observations. Single day composites are created to highlight mean TC structure for each flight and model run; this differs from compositing data across multiple TC flights. Vertical profiles use 10-m bins for comparisons, while 2D composite bin widths vary depending on the dataset. CRL data are binned using 3-km and 200-m radial and vertical bins. TDR profile and swath data both use 5 km radial bins, while the native vertical resolutions of 150 m and 500 m are used for each respective TDR dataset. This combination of vertical and radial bin widths is chosen to maximize data point counts within each bin, providing higher confidence levels, while still highlighting spatial variations of important kinematic and thermodynamic quantities.

4.4 Case Study: Hurricane Sam

Hurricane Sam was a long-lived Category 4 hurricane that formed in the main development region of the Atlantic Ocean on 22 September 2021 [Pasch and Roberts, 2022]. SSTs and wind shear magnitudes remained favorable for Sam, with the least conducive values during flight sampling periods reaching 28 °C and 11 kt, respectively.

Sam experienced rapid intensification during portions of its early life cycle (Fig. 4.3a): a 15.4

m s^{-1}) increase over a 24-h period [Kaplan and DeMaria, 2003]. It reached a peak intensity of 135 kt just before NOAA's P-3 (N42) mission 20210926H1 sampled the system on 0000 UTC 27 September 2021. These NOAA mission identifiers are used to reference each flight period throughout the paper. Sam then underwent an eyewall replacement cycle (ERC) in the presence of a temporary increase in environmental shear and an increase in radial ventilation [Pasch and Roberts, 2022, Tang et al., 2024], rapidly losing 30 kt of intensity by 0000 UTC 28 September 2021. NOAA mission 20210927H1 sampled Sam at this local minimum intensity. Sam then steadily intensified back to 125 kt strength by 0000 UTC 30 September 2021 when sampled by NOAA mission 20210929H2. The CRL was not deployed during the other P-3 (N43) flights, and the CRL was unable to collect data for some flights due to high turbulence, so no data from the 20210925H1, 20210927I1, or 20210929H1 Sam flights are used here. Sam's variable structure, combined with ample aircraft observations, make this TC ideal for demonstrating a new observation-model comparison framework.

Compared to the Best Track, COAMPS-TC consistently underestimated Sam's intensity, especially after 1200 UTC 29 September 2021 (Fig. 4.3a). Interestingly, the COAMPS-TC forecast initialized at 1200 UTC 27 September 2021 intensified the system by 15 kt before its intensity collapsed; this quick intensification led to a temporary intensity overestimation, impacting subsequent observational comparisons.

Sam was sampled by aircraft east and northeast of the Windward Islands as it began to recurve northwards (Fig. 4.3b). Sampling periods are nicely spaced along Sam's flight track. The effect of Sam's ERC can be seen in the low level TDR wind field, as the RMW expands from 10 km for the 20210926H1 flight to 30 km for the 20210927H1 and 20210929H2 flights (Fig. 4.3c).

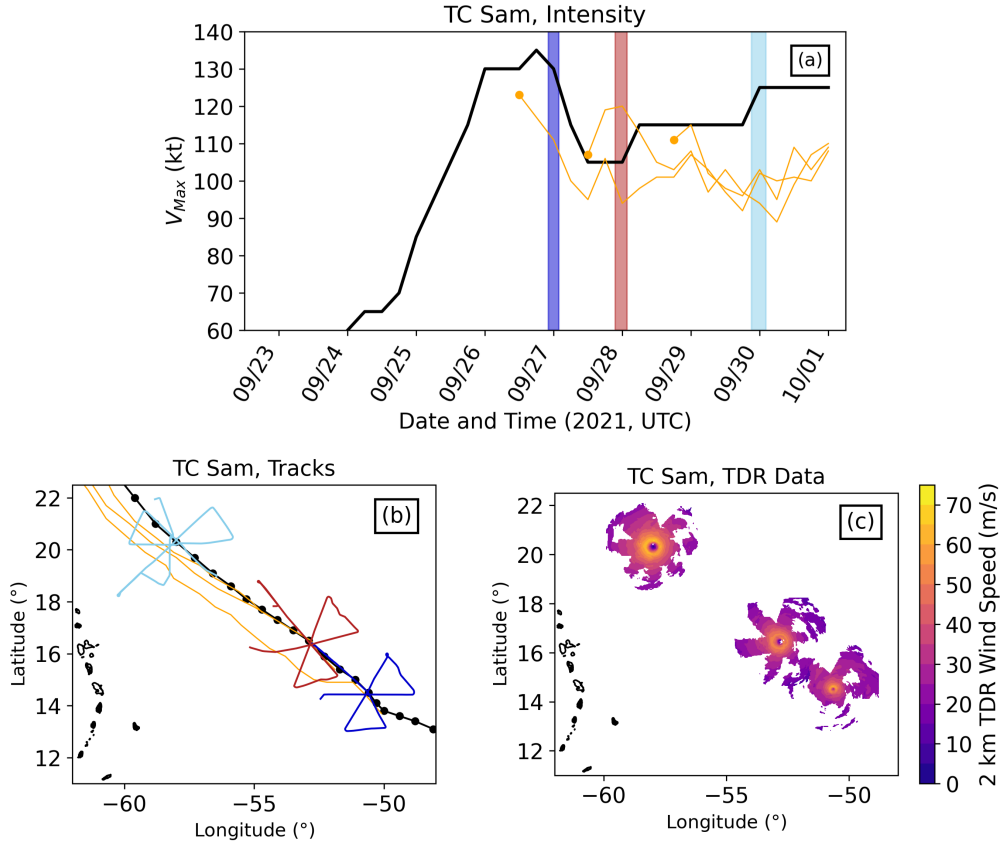


Figure 4.3: (a) NHC Best Track maximum sustained surface wind speeds from Sam (black line), along with forecasted COAMPS-TC maximum surface wind speeds (orange lines). Orange circles represent the three COAMPS-TC model initialization intensities. Colored vertical rectangles represent flight durations for P-3 flights 20210926H1 (dark blue), 20210927H1 (red), and 20210929H2 (light blue). (b) Spatial distribution of P-3 flights into Hurricane Sam that gathered TDR, CRL, and dropsonde data. Flight track colors match those shown in (a). Flight tracks are plotted atop the NHC 6-hourly Best Track (black line) and the three COAMPS-TC forecasted tracks (orange lines). (c) TDR-derived wind speeds at 2 km height for the three sampling periods.

4.5 Results

4.5.1 Kinematic Variability

TDR observations and COAMPS-TC model output of Sam's tangential wind speeds agree apart from anomalous RMW locations and peak wind speed strengths for some flights (Fig. 4.4). For flight 20210926H1, Sam's observed RMW was around 10 km with a narrow wind speed field and a small vertical gradient in the tangential wind speed (Fig. 4.4b). This structure suggests that an

ERC was imminent [Sitkowski et al., 2011], a feature not seen in this COAMPS-TC forecast. Peak modeled tangential wind speeds are stronger than the observed wind speeds for flight 20210927H1. This can be seen in the 2D composite (Fig. 4.4d-e, at the RMW). Finally, for flight 20210929H2, modeled tangential wind speeds are weaker and have a larger vertical gradient at the RMW (Fig. 4.4g-h), suggesting that the real vortex better maintained its coherent eyewall structure [DesRosiers et al., 2023].

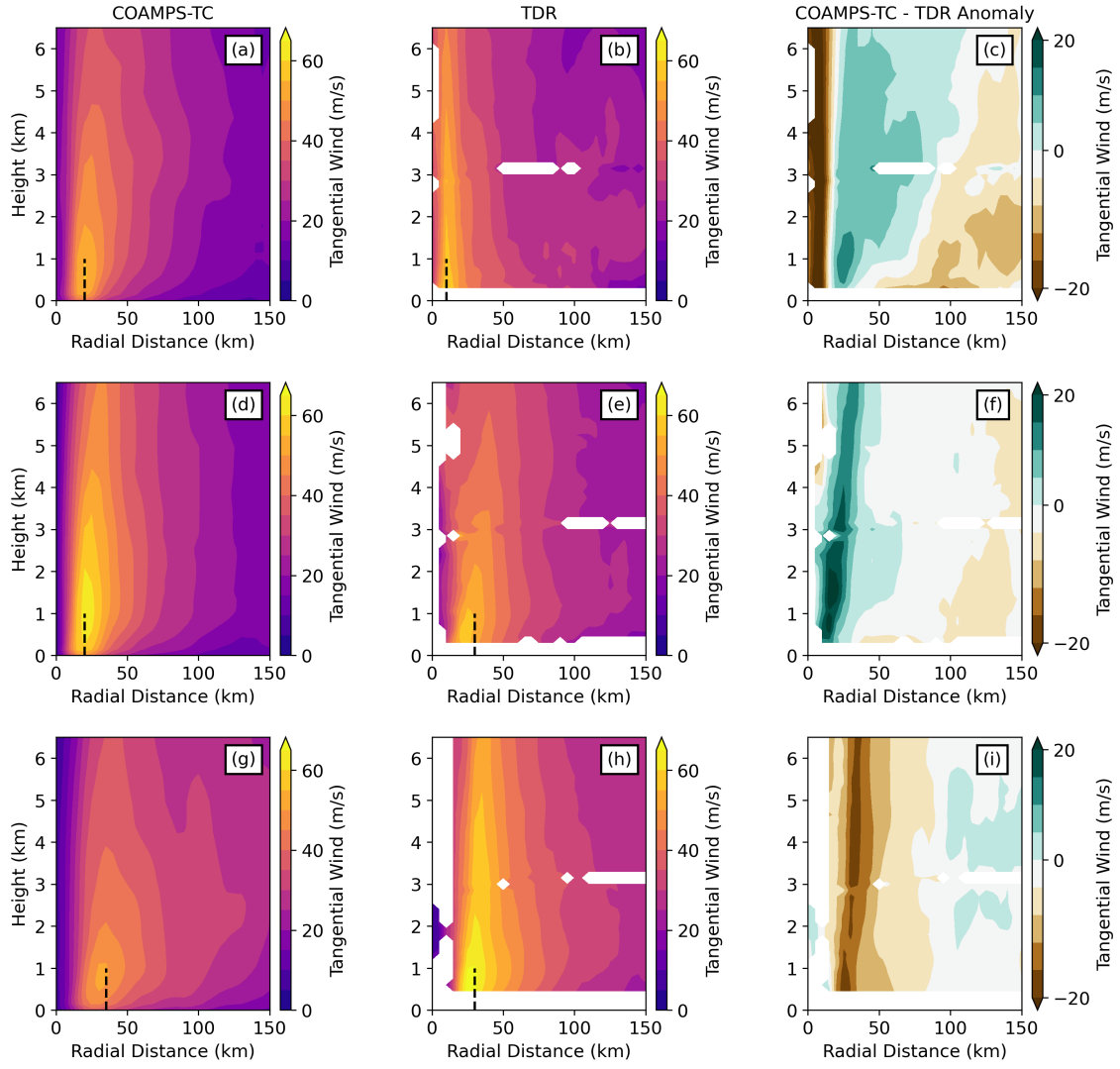


Figure 4.4: Radius-height composites of tangential wind speeds for Hurricane Sam flights 20210926H1 (a-c), 20210927H1 (d-f), and 20210929H2 (g-i). The differences (right column) between COAMPS-TC composites (left column) and TDR profile tangential wind speed composites (middle column) are provided. White regions in the TDR and anomaly composites indicate missing data due to insufficient hydrometeors in the TC eye or because the radar cannot sample efficiently at flight level. The vertical black lines reaching to 1 km height represent the locations of the COAMPS-TC and TDR 2 km RMWs across each flight day.

Although there are differences between COAMPS-TC and TDR radial wind speeds, agreement improves over each subsequent day, with little bias seen by the last flight. (Fig. 4.5). For COAMPS-TC, the radial wind speed composite for 20210926H1 shows a strong inflow layer below 1 km coupled to a strong outflow region at the RMW from 2 km to 6 km heights, coincident with the

TC eyewall (Fig. 4.5a). An interesting mid-level outflow layer is also seen in the composite from 1.5 km to 3 km height at 40 km to 150 km radial distance. These secondary circulation features match those found in strong, intensifying TCs [Barron et al., 2022, Rogers et al., 2012]. Meanwhile, the structure of the TDR radial wind speed composite is less coherent (Fig. 4.5b) with weaker mid-level outflow and a shallower, weaker inflow layer. The degraded secondary circulation seen in TDR observations suggests that Sam's ERC is underway on 20210926H1, sapping strength from the TC's deep eyewall convection. This evolving secondary eyewall can be seen in the widening of Sam's observed tangential wind field on 20210926H1 at 80 km radial distance (Fig. 4.4b).

On 20210927H1, Sam's modeled inflow is stronger than observations and extends slightly further towards the TC center, likely due to the model's narrower RMW (Fig. 4.5d-f). For mission 20210929H2, inflow heights are very similar, with the low-level TDR inflow slightly stronger (Fig. 4.5g-i). Eyewall outflow regions in both datasets are now weaker and more diffuse. This suggests that Sam's vortex has broadened, matching its wider RMW.

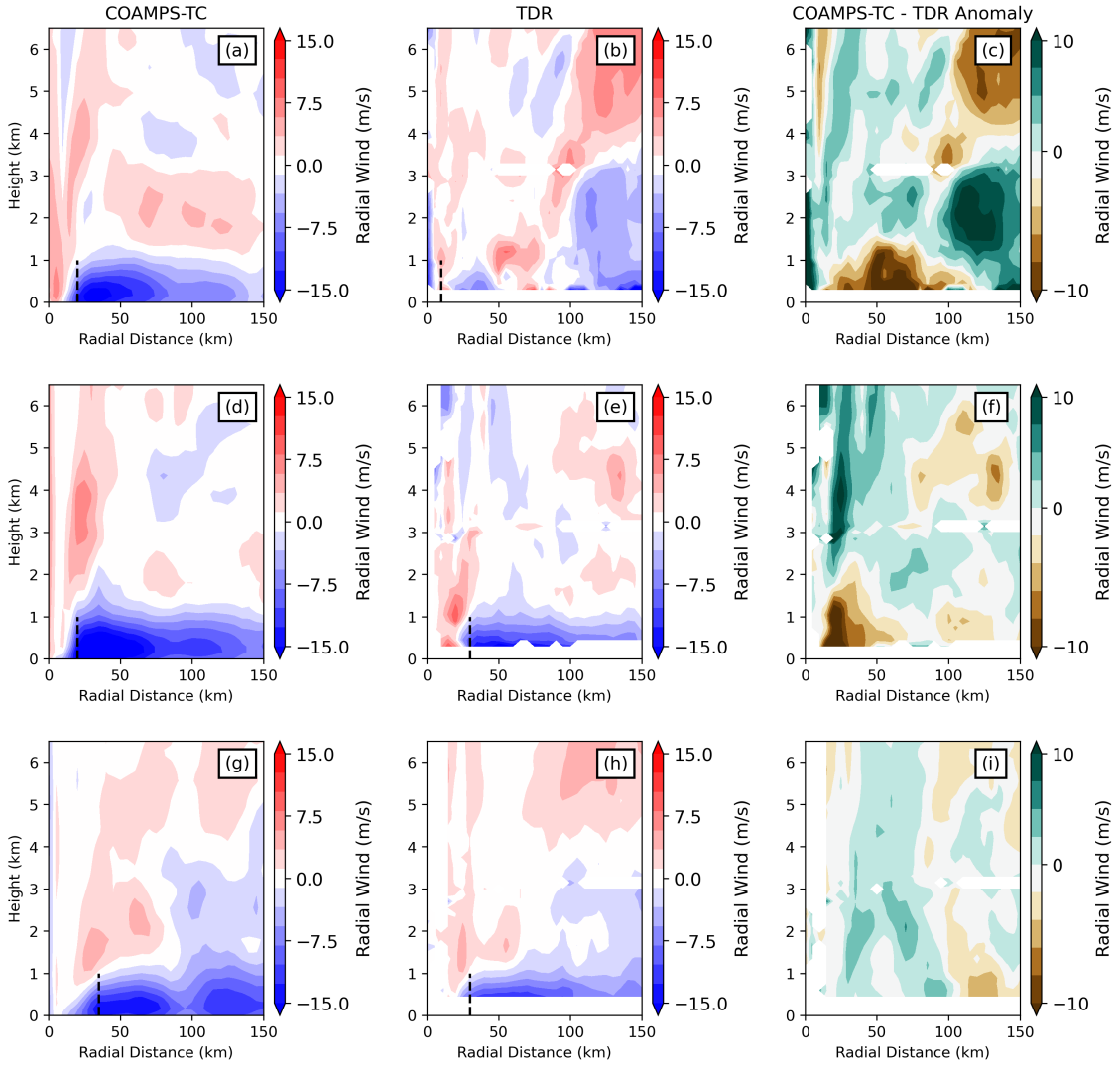


Figure 4.5: As in Fig. 4.4, but for COAMPS-TC and TDR profile radial wind speeds.

Modeled and observed vertical wind speeds also match reasonably well (Fig. 4.6). Across all dates, modeled eyewall updrafts at the RMW are stronger than those observed. This could be due to either stronger or more spatially coherent modeled updrafts. The TDR observed more frequent mean downdrafts coupled inside and outside the eyewall, a feature not seen in COAMPS-TC. TDR eye downdrafts are likely an erroneous result from a poor sample size of backscattering hydrometeors in this region or vertical velocity errors related to solving the continuity equation for the TDR swath data plotted here (Fig. 6e) [Rogers et al., 2012, Zhang et al., 2022a]. Modeled

updraft composites outside the RMW are slightly stronger or equal to those observed.

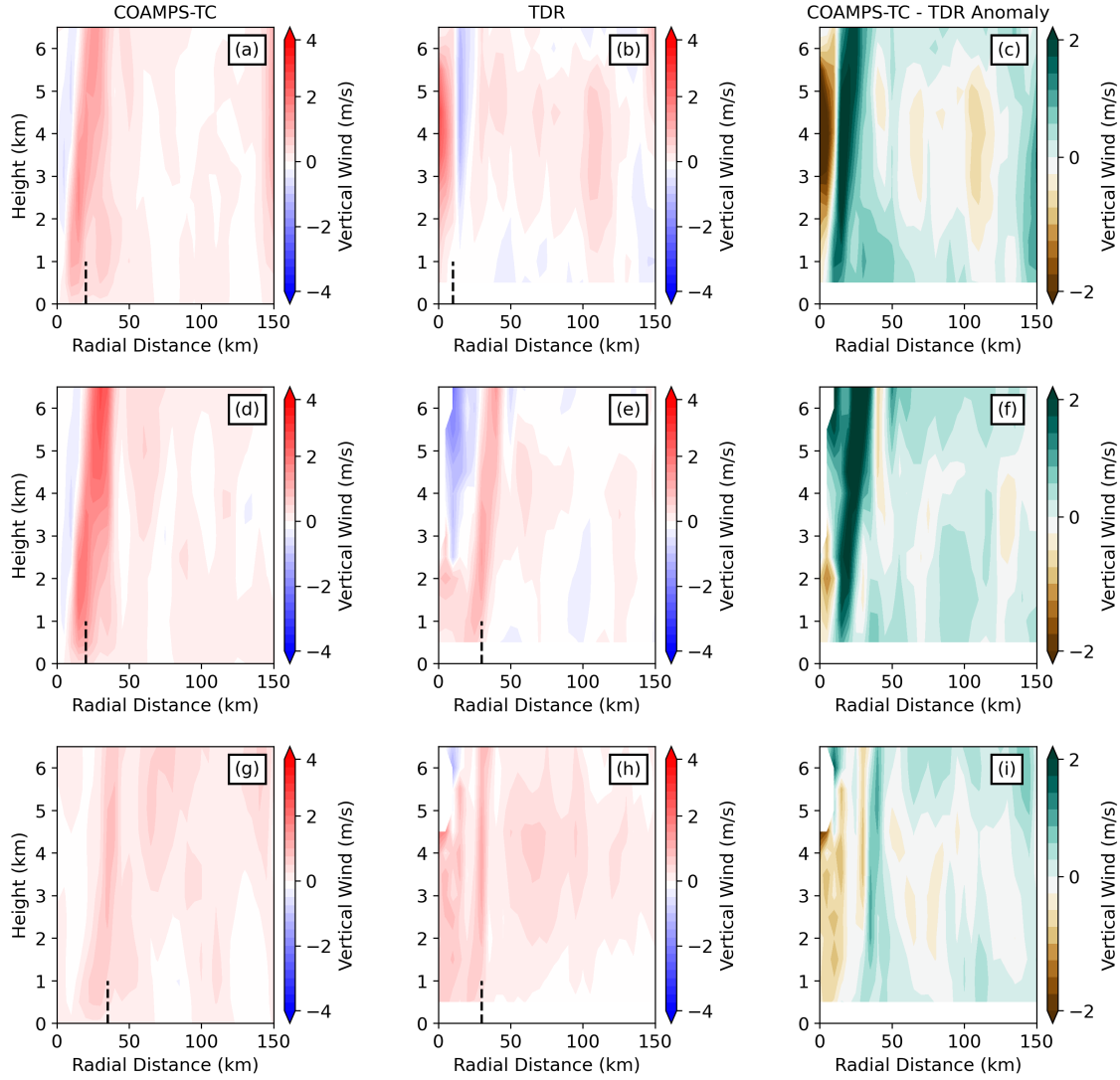


Figure 4.6: As in Fig. 4.4, but for COAMPS-TC and TDR profile radial wind speeds.

While the kinematic biases between TDR observations and COAMPS-TC forecasts are small enough to allow for effective comparisons, they are likely driven by Sam's observed ERC. ERCs occur in strong hurricanes and initially weaken the vortex, enlarge the eye, broaden the TC wind field, and re-intensify the system after the ERC [Fischer et al., 2020, Sitkowski et al., 2011]. Sam's ERC was well captured by TDR observations, diagnosing a transition away from a narrow RMW of

10 km for flight 20210926H1 to weaker wind speeds and an RMW of 30 km for flight 20210927H1. Sam's ERC was poorly represented by COAMPS-TC, which forecasted a 30 km wide RMW on 20210926H1, a 20 km RMW for flight 20210927H1, and TC intensification between these flights. COAMPS-TC's limited ability to capture the effects of Sam's ERC stems from its TC initialization method, which doesn't include secondary wind maxima in its prescribed vortex. The model's 4 km horizontal grid spacing is also too coarse to resolve ERCs for cases with narrow RMWs, like in Hurricane Sam [Jin et al., 2014, 2022]. While keeping these kinematic differences in mind, COAMPS-TC and TDR results are close enough to support further comparisons.

4.5.2 Thermodynamic Vertical Profiles

Given the differences in mean TC kinematics across observation periods, we investigate their impact on quantities like low-level potential temperature (θ) and moisture. First, mean vertical CRL profiles are compared to mean COAMPS-TC profiles. These comparisons partition the TC into two regions, inside and outside the eye. For these tests, eye and non-eye regions were manually determined for each pass using CRL cross sections. The eye-eyewall edge was determined by searching for the inner edge of a convective updraft in the CRL backscattered power channel, making sure updrafts or downdrafts are present in the in-situ vertical wind speed measurements, and checking that elevated TDR reflectivity was present at this radial distance. Manually checking for these three factors ensures an accurate eye-eyewall edge is identified.

To determine low level eye temperature and stability, θ profiles are plotted for each CRL dataset and model run (Fig. 4.7). θ is higher inside the eye than outside for both CRL observations and the COAMPS-TC model. This shows that the TC warm core extends downwards from the mid-troposphere to low levels for the model and observations. When comparing the model to observations, however, observed eye θ values are much higher than COAMPS-TC values. The θ disagreement is much smaller outside the TC eye.

This cold bias in modeled low-level TC eyes, together with the agreement between modeled and observed temperatures outside the eye, indicates that a weaker horizontal temperature gradient

is present at low levels in COAMPS-TC. Two possible explanations exist: either the entire warm core is too cold in COAMPS-TC, or that low-level warm core temperature biases differ from upper levels. Without high altitude dropsondes in the TC eye [Doyle et al., 2017, Komaromi and Doyle, 2017], the cold bias mechanism present in COAMPS-TC cannot be confirmed.

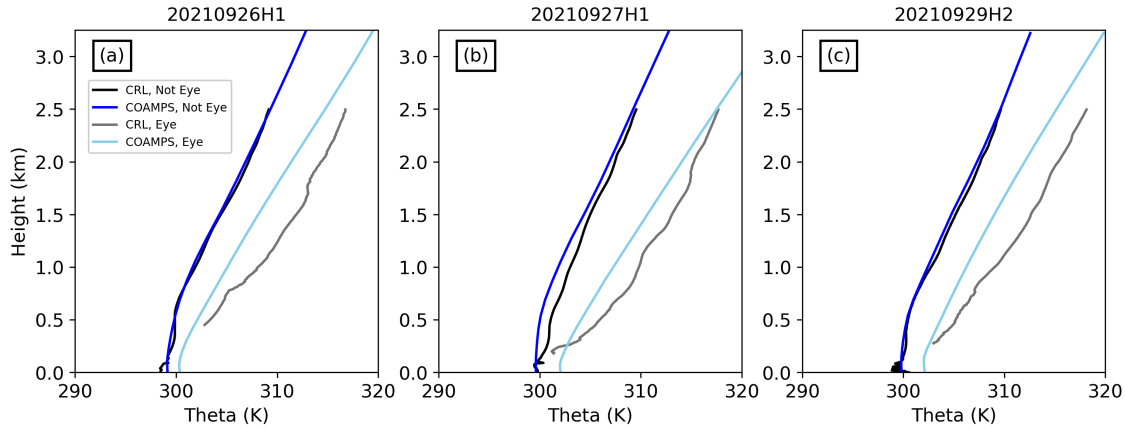


Figure 4.7: Mean vertical profiles of θ for Hurricane Sam flights 20210926H1 (a), 20210927H1 (b), and 20210929H2 (c) using collocated CRL and COAMPS-TC data. Profiles are shown inside the eye for CRL data (light gray line), outside of the eye for CRL data (black), inside the eye for COAMPS-TC data (light blue), and outside of the eye for COAMPS-TC data (dark blue).

Next, consistent moisture differences emerge when comparing modeled TC moisture outside the eye to CRL observations (Fig. 4.8). Across all three flight days, modeled ABL moisture values are too moist compared to CRL mean profiles, with anomalies of 2.20 g kg^{-1} for flight 20210926H1, 1.77 g kg^{-1} for 20210927H1, and 1.55 g kg^{-1} for 20210929H2 in the lowest 750 m of the atmosphere. This anomalously moist region extends upwards through the ABL to flight height for flights 20210926H1 and 20210927H1.

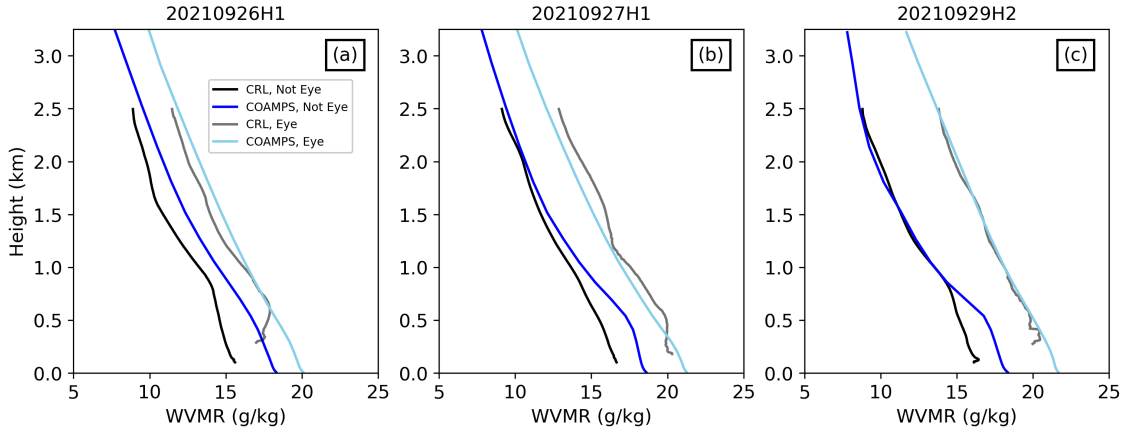


Figure 4.8: As in Fig. 4.7, but for COAMPS-TC and CRL WVMR profiles.

4.5.3 Thermodynamic 2D Composites

To get a better sense of the radial distribution of thermodynamic anomalies across each flight day, radius-height composites are created for model and CRL quantities. For the θ composites, a slight COAMPS-TC cold bias exists in the rainbands (roughly outside of 50 km radial distance), especially for flight 20210927H1, similar to the profile analysis (Fig. 4.7).

Looking at the TC eye, a large low-level cold bias is evident in COAMPS-TC. This cold bias exists across all three observational periods, with mean values of 2.34 K, 2.00 K, and 3.03 K for each subsequent sampling period. This cold bias exists uniformly across the eye on 20210926H1 and 20210929H2, but it is more biased in the outer eye on 20210927H1. The strong COAMPS-TC cold bias that exists in the low-level eye creates a weaker low-level temperature gradient and suggests that the modeled warm core doesn't extend as far downwards as in observations.

A range of low-level eye temperature biases are present in the literature [Nolan et al., 2009b, Smith et al., 2017]. Recent studies have found a cold bias in a single HWRF model run [Cione et al., 2020] and a cold bias aloft in HWRF composites [Zhang et al., 2020], but large differences between these studies and our study prevent direct comparisons.

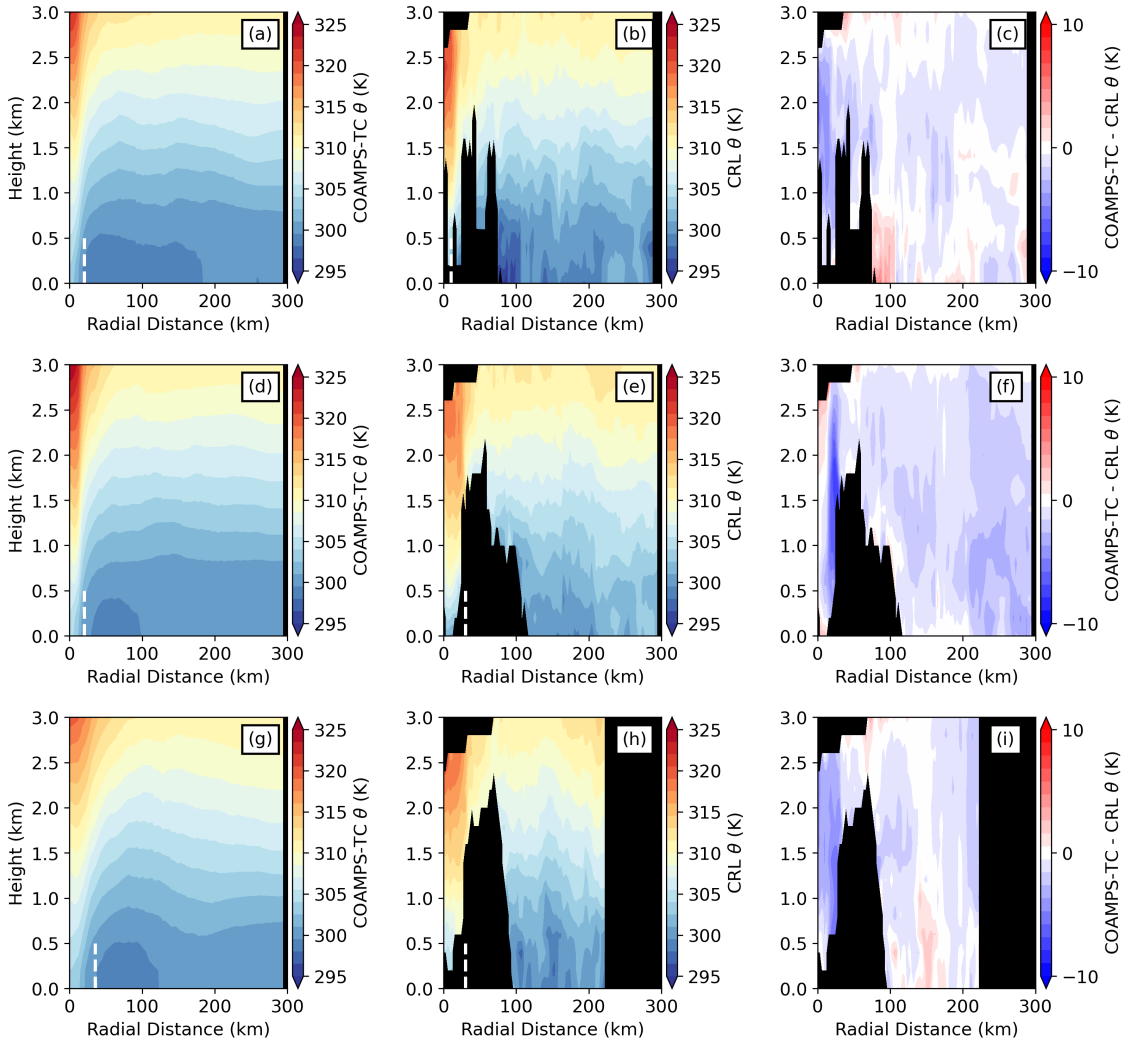


Figure 4.9: Radius-height composites of θ for flights 20210926H1 (a-c), 20210927H1 (d-f), and 20210929H2 (g-i) for COAMPS-TC (left column), the CRL (middle column), and their anomaly (right column). Black regions in the CRL and anomaly composites indicate missing data due to total signal attenuation from deep clouds in the TC eyewall. The vertical white lines reaching to .5 km height represent the locations of the COAMPS-TC and TDR 2 km RMWs across each flight day.

Similar composites were created for modeled and observed moisture distributions (Fig. 4.10).

COAMPS-TC is moister than CRL observations throughout most of the rainbands, with mean bias values of 0.76 g kg⁻¹, 0.51 g kg⁻¹, and .67 g kg⁻¹ for each subsequent sampling date. Moisture values below 800-m height, which roughly correspond to within the TC ABL [Zhang et al., 2013], have larger positive biases of 1.77 g kg⁻¹, 1.32 g kg⁻¹, and 1.63 g kg⁻¹ for each flight. These results

match the rainband vertical profiles well (Fig. 4.8).

Some dry biases exist in the rainbands above the ABL. This suggests that moisture aloft is better represented by the simulations than ABL moisture, or that biases are smaller because there is less moisture aloft. Furthermore, these dry biases are most prominent in the outer rainbands (roughly > 150 km from the TC center), especially on 20210929H2. Meanwhile, large moist biases aloft are found at smaller radial distances, closer to the eyewall convection. Overall, this enhanced inner core moisture indicates that modeled TCs are insulated from the dry outer environment and the presence of a more favorable low-level inflow environment for convective growth. This high spatial variability of moisture throughout Hurricane Sam's eye and rainbands from individual reconnaissance flights can only be determined using the CRL, which provides orders of magnitude more thermodynamic vertical profiles in cloud free TC regions than dropsondes do.

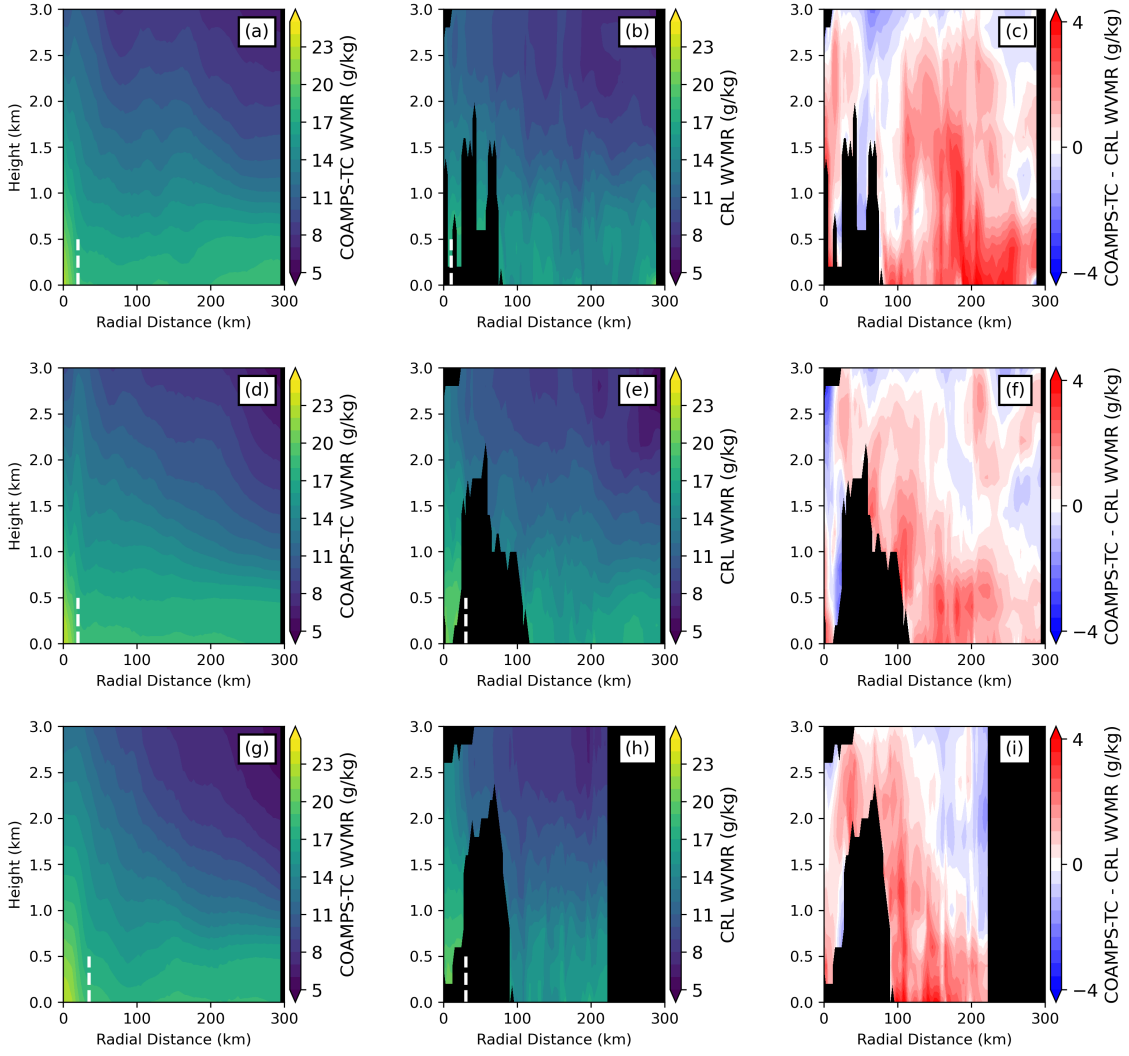


Figure 4.10: As in Fig. 4.9, but for COAMPS-TC and CRL WVMR.

Prior studies have investigated low-level moisture biases in other models. These studies have found enhanced low-level moisture biases in WRF [Nolan et al., 2009a], substantial dry biases in HWRF [Cione et al., 2020], and a model dry bias aloft across many HWRF composites [Zhang et al., 2020], yet the substantial differences between each model prevent direct comparisons.

Combining θ and moisture composites, θ_e distributions are calculated for each dataset and flight day (Fig. 4.11). θ_e is a useful quantity for determining the available atmospheric energy content for deep convection, as this quantity is conserved under dry and moist vertical motion, and it is consistently used in the literature [Powell, 1990, Smith et al., 2017, Wadler et al., 2022].

Looking at the θ_e distributions, a noticeable negative bias is found in the TC eye, and a positive bias is found in the rainbands.

These results match those found previously; COAMPS-TC temperature cold biases dominate the θ_e eye composite, while positive COAMPS-TC moisture biases drive rainband differences (> 50 km from the TC center). The higher observed θ_e values in the TC eye suggest that the model misses heightened convective potential, cloud formation, and mixing at low levels, as seen in prior observational studies [Hirano et al., 2022, Murray et al., 2024]. Meanwhile, COAMPS-TC supports deeper convection around the eyewall and near the inner rainbands, as θ_e anomalies are uniformly positive here. These two θ_e distributions combine to create a much weaker modeled horizontal gradient of θ_e , which could impact the kinematics of Hurricane Sam's spinup and intensity maintenance [Smith et al., 2017]. The modeled vertical gradient of θ_e is also generally higher in COAMPS-TC, with the largest θ_e anomalies just above the surface and weaker positive to weak negative anomalies aloft. These differing θ_e distributions support decreased vertical stability in the COAMPS-TC model and increase vertical mixing.

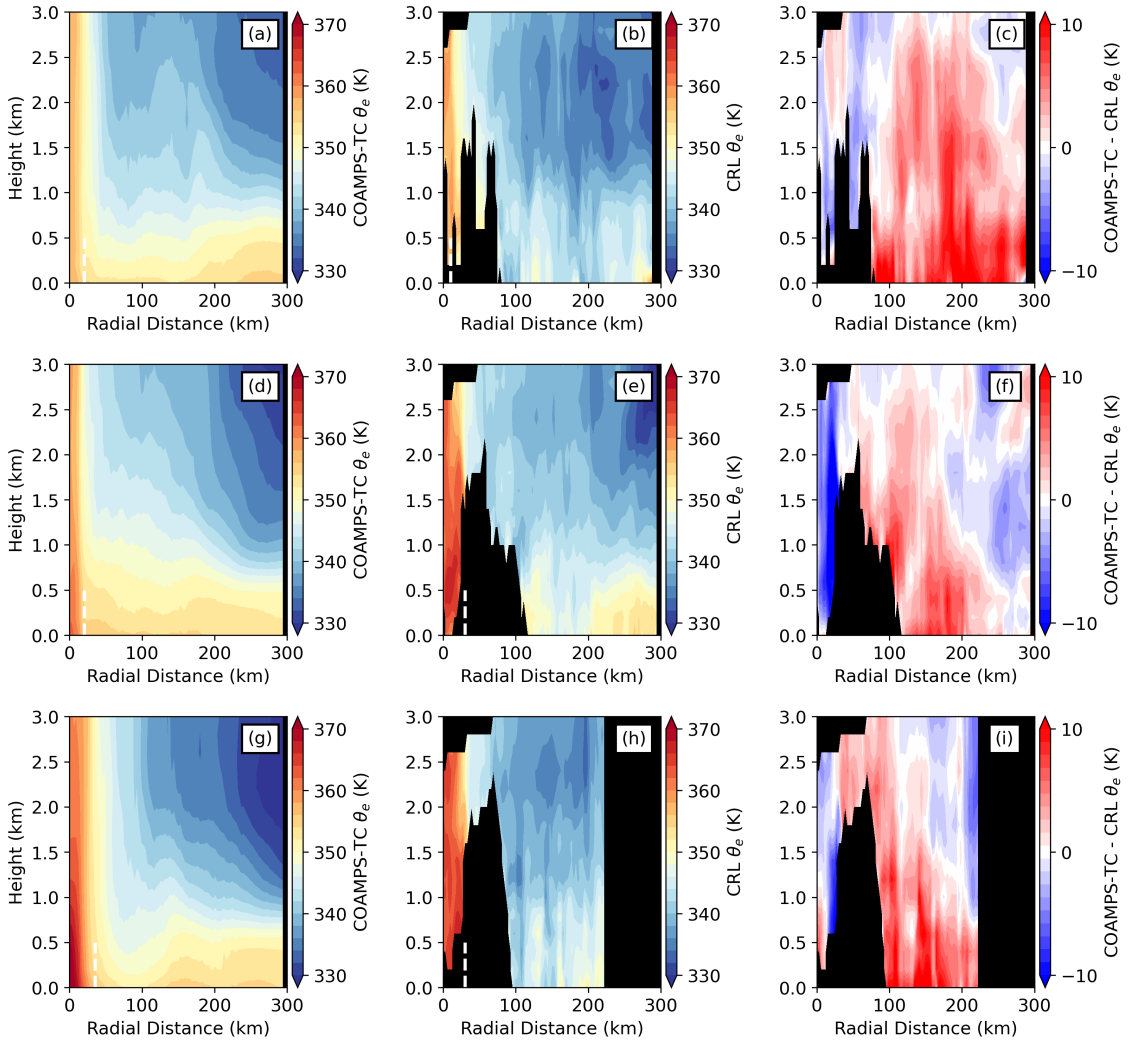


Figure 4.11: As in Fig. 4.9, but for COAMPS-TC and CRL θ_e .

4.5.4 Kinematic and Thermodynamic Asymmetries

The full-TC (axisymmetric) results presented above are complemented by a shear-separated (asymmetric) analysis. This framework is important because ABL temperature and moisture fields are often modified by the environmental shear vector [Alland et al., 2021a, Chen et al., 2021b, Nguyen et al., 2019, Wadler et al., 2022, Zhang et al., 2013]. To demonstrate this, the TC is split into four shear oriented quadrants: downshear right (DR), downshear left (DL), upshear right (UR), and upshear left (UL). TC thermodynamics often exhibit a wavenumber 1 asymmetry,

with low-level moisture and θ_e maximized in the TC's DR quadrant [Chen et al., 2021b, Wadler et al., 2022, Zhang et al., 2013]. These asymmetries can be masked when averaging azimuthally, thus conducting an asymmetric analysis is necessary and possible given the CRL's comprehensive thermodynamic data coverage.

Cross sections from different environmental shear quadrants in Hurricane Sam reveal important low-level moisture asymmetries (Fig. 4.12). Looking at the observation-model moisture asymmetries in the DL and UR quadrants (Fig. 4.12g, h), note that positive model moisture biases exist below 1 km in both shear quadrants. This suggests that the axisymmetric moisture bias diagnosed previously exists throughout the TC, not just in one part of the storm. The modeled UR moisture bias is stronger and deeper (Fig. 4.12h) than in the DL quadrant (Fig. 4.12g), though, reaching up to 2 km above the sea surface. This suggests that the model's ABL recovers moisture more efficiently than observed, especially in the UR quadrant, leading to a more symmetric moisture distribution.

Interestingly, in the distant COAMPS-TC rainbands (> 100 km from the TC center), asymmetric water vapor distributions are similar (Fig. 4.12c). The CRL, meanwhile, shows a distinct positive moisture anomaly in the DL quadrant compared to the UR quadrant (Fig. 4.12f). This moister DL outer environment in observations shows enhanced TC asymmetry, suggesting that the COAMPS-TC model doesn't capture all the spatial variability seen in the observations.

The moisture differences seen above could arise from different physical drivers. One possibility is that vertical mixing in the low-level TC rainband is stronger in the model compared to reality, adding more moisture to COAMPS-TC's ABL (Fig. 4.6). Radial and downdraft ventilation can also mix low θ_e air towards the low-level TC inner core and dry out the ABL [Alland et al., 2021a, Tang et al., 2024]. These processes act on mean and turbulent scales, and they seem to have a larger impact on observations, displayed by their finer-scale low-level variation (Fig. 4.12).

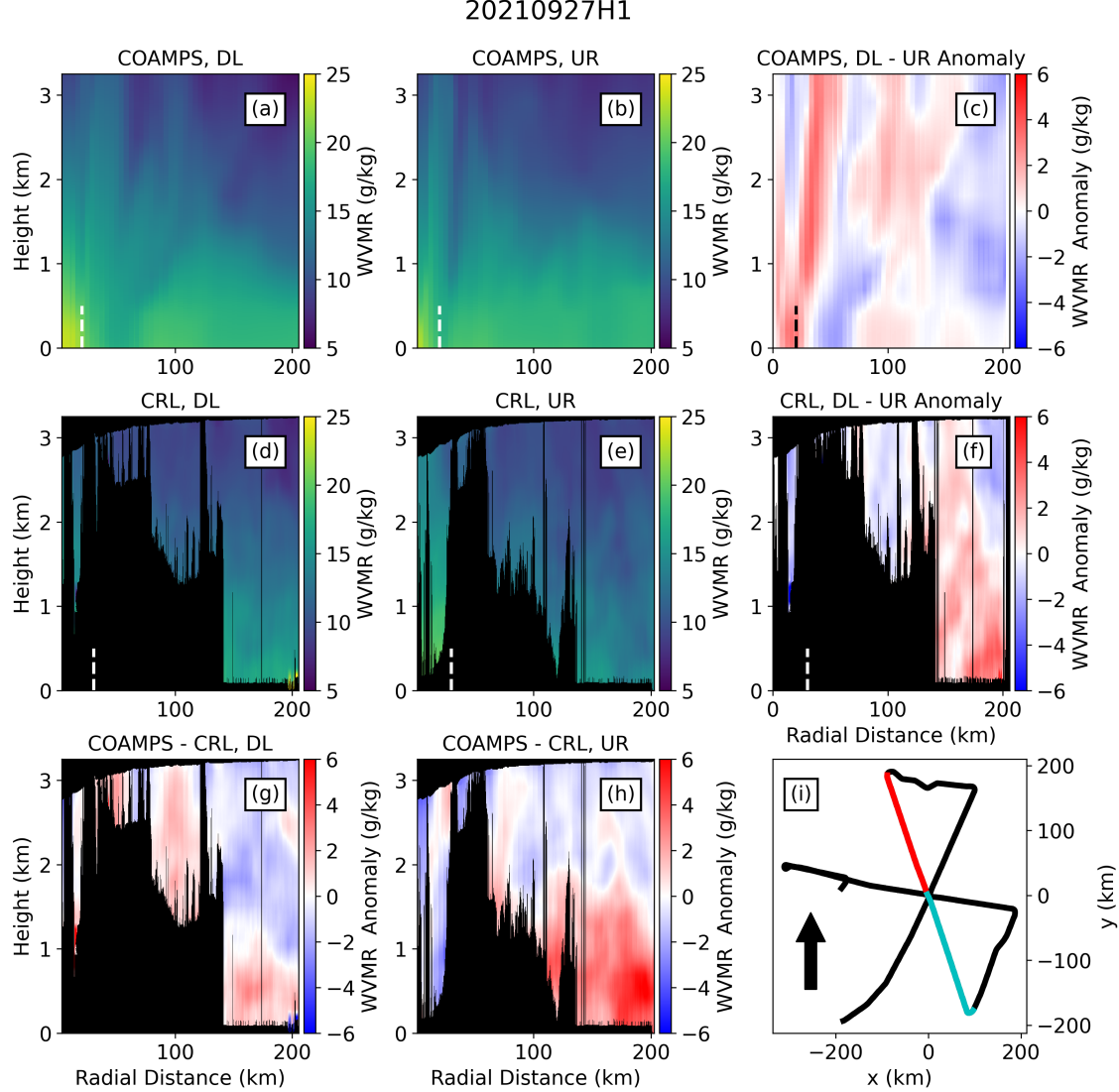


Figure 4.12: Individual cross sections of WVMR taken from the COAMPS-TC model (a, b) and CRL observations (d, e) in the DL and UR environmental shear quadrants of Hurricane Sam during flight 20210927H1. Anomalies are shown for the different quadrants (c, f) and model vs observations (g, h). A shear-corrected flight pattern highlights the location of the DL (red line) and UR (teal line) flight legs (i). The black arrow denotes the environmental shear direction. The vertical white lines (black line in c for clarity) reaching to .5 km height represent the locations of the COAMPS-TC and TDR 2 km RMWs across each flight day.

Another driver of moisture differences are changes in radial inflow strengths and heights. Cross sections from the same flight tracks discussed above display major radial wind speed differences (Fig. 4.13). For the DL quadrant, COAMPS-TC's inflow layer (Fig. 4.13a) has a similar

height compared to observations (Fig. 4.13c), yet it has a much larger magnitude. This stronger inflow can generate increased surface enthalpy fluxes and ABL moisture mixing, potentially explaining the enhanced modeled low-level WVMR. Similarly, inflow is stronger and deeper in the UR quadrant of COAMPS-TC, once again increasing moisture fluxes. This stronger, more symmetric inflow could explain the positive moisture biases seen in COAMPS-TC's ABL.

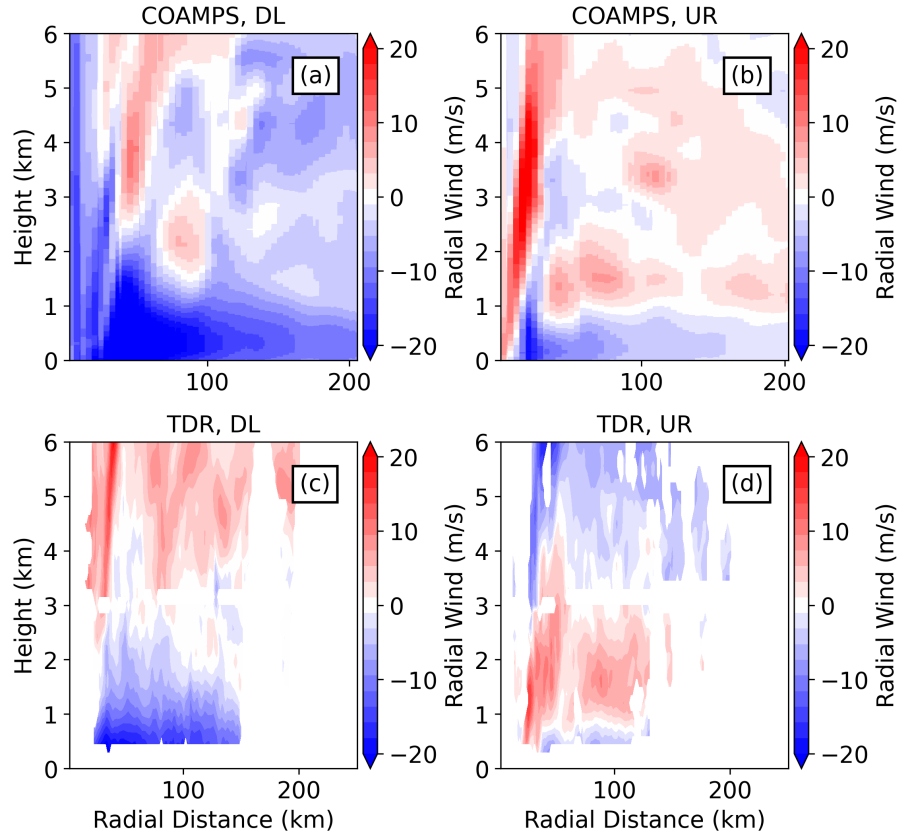


Figure 4.13: Individual cross sections of radial wind speeds from COAMPS-TC (a, b) and TDR profile observations (c, d) taken from the same DL and UR environmental shear quadrants as in Fig. 4.12.

4.6 Conclusions

In this study, we introduced a novel framework for comparing single TC model forecasts with aircraft observations to diagnose key thermodynamic and kinematic structural differences.

This study differs from traditional forecast assessment techniques, which generally rely on metrics like track and intensity errors or observational composites across many cases to improve models [Cangialosi et al., 2020, Heming et al., 2019, Zhang et al., 2012, 2020]. To create these single day comparisons, we contrasted high-resolution measurements from the TDR and the novel CRL with operational COAMPS-TC forecasts from Hurricane Sam (2021). CRL data proved particularly useful, filling thermodynamic measurement gaps in the TC eye and rainbands and facilitating the creation of unique single-day thermodynamic composites. This novel comparison framework uncovered persistent COAMPS-TC low-level cold biases in the eye and anomalous moist biases in the model’s ABL. These thermodynamic differences created a weaker θ_e horizontal gradient throughout the low-level TC in the model.

A combination of both mean and turbulent processes create the thermodynamic anomalies seen in COAMPS-TC. Mean processes are captured by the equations of motion governing COAMPS-TC; these include differences in primary and secondary circulations that force thermodynamic change. Meanwhile, turbulent processes like convective downdrafts operate on scales close to the model’s gray zone [Chen et al., 2021c] or are unresolved and require parametrizations to capture their effects [Stull, 1988].

Changes in mean secondary circulation can help generate the differences between Sam’s observed and modeled moisture distributions. For instance, the strong vertical shear caused by stronger modeled radial inflow (Fig. 4.5) acts to generate increased enthalpy fluxes and cap ABL moisture, reinforcing the strong vertical moisture gradients seen COAMPS-TC. Additionally, enhanced mean model rainband updrafts and weaker downdrafts (Fig. 4.6) promote less low θ_e air ventilation from aloft, potentially creating a stronger ABL moisture layer. Meanwhile, many convective downdrafts operate on scales close to or below the model’s gray zone, suggesting that turbulent processes also impact modeled and observed kinematic and thermodynamic composites. Modifying turbulent parameterizations, particularly in the ABL, can be an effective way to nudge TC simulations towards observed structures [Gopalakrishnan et al., 2021, Zhang et al., 2012].

The low-level eye cold bias and lower modeled TC intensity seen in COAMPS-TC can po-

tentially be accounted for by tuning the turbulent vertical eddy diffusivity parameter. Reducing vertical eddy diffusivity can create a stronger warm core, among other TC structural effects [Gopalakrishnan et al., 2013, Zhang et al., 2015]. This change could eliminate the cold bias found in the modeled TC eye, and it could increase wind speed forecasts, potentially improving Sam's intensity prediction at longer lead times. This strategy has drawbacks, however, as lowering the vertical eddy diffusivity can lead to even stronger radial wind speed biases for flights 20210926H1 and 20210927H12021 [Zhang et al., 2015]. Additionally, the modeled eye cold bias might only exist at low levels: COAMPS-TC might do a better job at simulating upper level temperature anomalies. To test this, we need to look beyond low-level CRL composites using high altitude dropsonde data [Komaromi and Doyle, 2017].

The positive moisture biases found in the COAMPS-TC ABL and in previous modeling studies [Nolan et al., 2009a] could result from the turbulent vertical moisture diffusivity parameter. Similar to the vertical eddy diffusivity term mentioned above, this quantity controls how readily moisture mixes vertically throughout the ABL [Stull, 1988]. This quantity, related to the moisture roughness length, is highly uncertain and is often held constant or varies based on the enthalpy exchange coefficient [Bryan, 2012, Xu and Zhao, 2021]. For COAMPS-TC, the moisture diffusivity is based on the TOGA COARE parameterization [Komaromi et al., 2021, Fairall et al., 2003], which is designed for low to medium wind conditions and linearly increases the Charnock parameter for wind speeds between 10 m s^{-1} and 18 m s^{-1}). Given the uncertainty in vertical moisture diffusivity, this term could be tuned to a smaller value, which is known to decrease ABL and eyewall moisture, increase the moisture ABL depth, and lower surface heat flux [Xu and Zhao, 2021]. Interestingly, these moisture diffusivity changes influence TC central pressures but do not greatly impact tangential wind speeds [Xu and Zhao, 2021]. Therefore, this moisture diffusivity parameter can be tuned alongside the eddy diffusivity term with less fear of generating offsetting biases.

While this paper acts as an important demonstration of model evaluation techniques and presents future avenues for improving COAMPS-TC ABL parameterization schemes, our compar-

isons can be improved in a few ways. With 4 km grid spacing, the operational configuration of COAMPS-TC used in this paper is an order of magnitude coarser than the observations used for evaluation. Using a smaller grid spacing would allow for better comparisons with observations and the direct simulation of convective-scale features like intense eyewall updrafts [Gentry and Lackmann, 2010], ERCs [Jin et al., 2022], and shallow eye convection [Murray et al., 2024]. While these resolution increases are prohibitively expensive for operational implementation at this time, these tests would allow for more detailed investigations into the kinematic drivers of TC thermodynamic evolution.

Running these tests using other operational TC models, such as HWRF and HAFS, could isolate whether Hurricane Sam's low-level biases are unique to COAMPS-TC, or if they occur in other simulation frameworks [Alaka et al., 2024, Alvey et al., 2024]. Similarly, ABL parameterizations can be changed in each forecasting model to determine the impact of the mean and turbulent processes discussed above. While Sam was analyzed here, other TCs sampled by the CRL can be studied using the same comparison framework. CRL data are currently available from eight other TCs, and more thermodynamic composites can be created if the CRL is deployed operationally again. Overall, future work should focus on applying this framework at higher model resolutions, using different TC models and ABL parameterizations, and results should be compared across multiple storms.

To enhance low-level observational composites, which would improve model comparisons, cloud and precipitation data from the CRL or TDR could be used. This would offer powerful data for model evaluation of a TC's convective and microphysical properties. Additional remote sensing platforms can be used alongside the CRL, including the Doppler wind lidar [Bucci et al., 2018, Zhang et al., 2018] and the Imaging Wind and Rain Airborne Profiler (IWRAP) radar [Guimond et al., 2018]. While using additional measurement platforms on a single P-3 poses operational challenges, these remote sensing instruments would provide wind measurements at higher spatial resolution than the TDR. This would complement CRL thermodynamic observations nicely and allow for the calculation of turbulent enthalpy fluxes throughout the ABL. Even without additional

wind measurements, using the CRL for regular Hurricane Hunter operations would provide much more low-level thermodynamic data, which is particularly useful for initializing model runs for weaker systems where fewer dropsondes are launched [Sippel et al., 2022]. Using these current and proposed remote sensing techniques would greatly enhance the spatial coverage of kinematic and thermodynamic TC data, allowing for more detailed model comparisons and forecast bias corrections.

Acknowledgments

This research project was made possible by ONR Grant N00014-21-1-2606 through the TCRI Departmental Research Initiative. Much of this research was completed during the Summer 2024 Naval Research Enterprise Internship Program at the U.S. Naval Research Laboratory in Monterey, CA. The authors thank the employees at NOAA/AOML Hurricane Research Division who deployed and operated the CRL during the 2021 and 2022 Atlantic hurricane seasons. Co-authors Moskaitis and Doyle gratefully acknowledge support from Office of Naval Research Program Elements 0601153N, 0602435N, and 0603207N. Co-author Jun Zhang acknowledges support from Office of Naval Research Award N00014-24-1-2761 and NOAA grant NA22OAR4050669D.

Data Availability Statement

TDR profile and dropsonde observations were obtained from NOAA AOML's website. TDR swath data from 1997 to 2023 are made available via the TC-RADAR dataset (Fischer et al. 2022). This study used the operational COAMPS-TC model that was run during the 2024 TC season (v2024 COAMPS-TC). Processed CRL, TDR, dropsonde, and COAMPS-TC data for TC Sam are available online via the link: <https://doi.org/10.5281/zenodo.15007542> (Murray et al. 2025). Python code used to create the figures in this paper can be accessed via the link: <https://github.com/ethanmurr/murray-et-al-2025-coamps-vs-observations-tc-sam>.

Chapter 5

CONCLUSIONS AND FUTURE WORK

5.1 Conclusions

The research presented in Chapters 2, 3, and 4 of this dissertation advances our understanding of TC cloud structure and thermodynamics through novel NOAA P-3 aircraft observations and an innovative observation-model comparison framework. To do so, high-resolution Compact Raman Lidar (CRL) data are compared with traditional observational techniques and operational model output. Together, this thesis provides new insights into cloud, precipitation, and thermodynamic structures throughout the TC inner core.

Chapter 2 focuses on novel high-resolution, low-level cloud height and thermodynamic measurements in the TC eye. Shallow convective clouds are found throughout the eye, differing from the uniform stratiform clouds typically depicted there [Houze, 2010]. This work links the formation of these convective clouds to low-level thermodynamics and vertical mixing. Eye cloud structures are presented in a detailed case study of Hurricane Sam (2021). They show significant horizontal and vertical variation, with some deeper convective clouds interspersed between narrow convective clouds, shallow stratiform layers, and clear air. An increase in Sam's low-level eye moisture and a decrease in its eye inversion strength over time results in a higher spatial coverage of low-level convection.

Distributions of cloud heights and vertical winds show that tropical depressions experience widespread central lift while strong hurricanes possess enhanced turbulent vertical mixing. Cloud width statistics demonstrate that coarser-resolution operational models may fail to capture small

eye cloud structures. This would prevent some models from accurately representing convective eye cloud formation, removing an important intensity change pathway from the model. This chapter demonstrates that vertical mixing in the low-level TC eye can overcome the region's strong temperature inversion, leading to the formation of low-level convective clouds at all TC intensities.

In Chapter 3, CRL data are used to provide unique rainfall and cloud height statistics in the TC rainbands. To do so, a novel classification algorithm distinguishes between different rainband features in CRL backscattered power data with unprecedented detail. A case study of Hurricane Sam demonstrates that CRL classifications correspond nicely with tail Doppler radar (TDR) classifications, but they have higher spatial resolution and can distinguish between low-level clouds and rainfall. This provides valuable information on TC rainband convective and stratiform development.

Statistical results reveal that many rainband convective and shallow clouds exist at sub-kilometer scales, and that high-resolution TC models are required to capture these features. There are also pronounced asymmetries in TC rainband convection, rainfall, and clear air. The downshear left quadrant has the strongest convection and least clear air, while the UR quadrant has the least convection and stratiform rain but the most clear air. This confirms the presence of asymmetries that were indirectly inferred using other observational techniques [Hence and Houze, 2012]. In summation, this study uses the CRL to provide a new perspective on convective cloud and stratiform rainfall development in the TC rainbands.

Chapter 4 introduces a novel framework for comparing individual operational TC model forecasts with high-resolution aircraft observations. This work focuses on differences between low-level dynamic and thermodynamic properties across three observation periods in Hurricane Sam by contrasting TDR and CRL measurements with operational COAMPS-TC forecasts. Persistent low-level cold biases in the TC eye and anomalous moist biases in the model's boundary layer are identified. This work suggests that tuning boundary layer parameterizations and increasing model resolution, if possible, could improve agreement with observations. This single storm observation-model comparison framework is applicable to other storms and models, offering a promising pathway for systematic model evaluation and improvement.

The CRL is central to these observational advances, as it provides unique, high-resolution measurements of low-level cloud tops, rainfall, temperature, and moisture. Unlike the TDR, the CRL can resolve boundary layer clouds, shallow convection, and sea-spray aerosols, filling critical observational gaps. The high spatial density of temperature and moisture vertical profiles collected by the CRL nicely supplement dropsonde and in situ data typically collected by the P-3 aircraft. This allows for enhanced analysis of TC thermodynamic properties and more detailed comparisons with models.

5.2 Future Work

Looking forward, collecting CRL data across a broader range of TC intensities, environmental conditions, and storm stages would enable more comprehensive statistical analyses. Particularly, current CRL samples are biased towards intensifying storms and those experiencing moderate wind shear, limiting the scope of the statistical tests conducted in this thesis (Fig 3.1). More legs from weakening and steady state storms experiencing weak or strong shear would allow for more detailed intensification and shear strength tests, similar to TDR based studies [Wadler et al., 2023a, Zhang et al., 2022a] Furthermore, collecting data from Cat. 3-5 hurricanes, landfalling TCs, TCs with enhanced rainfall and storm surges, and TCs undergoing rapid intensification would provide insight into the most societally impactful storms [Bosma et al., 2020, Gori et al., 2025, Anderson et al., 2020]. This makes the planned CRL deployment during the 2025 hurricane season especially valuable.

While the work presented in this thesis collocates CRL data with TDR, dropsonde, and in situ data, these comparisons can be expanded upon. For instance, CRL, dropsonde, and in situ thermodynamic data can be fully integrated into combined profiles. This would provide the most complete observational coverage of low-level TC temperature and moisture possible, and it would be an important step towards assimilating CRL data into operational or research forecasts [Christophersen et al., 2022, Ditchek and Sippel, 2023, Sippel et al., 2022].

Integrating CRL measurements with other remote sensing platforms is another powerful

option for future research. Comparisons of thermodynamic data between the CRL and sUASs could validate CRL retrievals and add another source of data to the assimilation framework discussed above [Cione et al., 2020, Sellwood et al., 2023]. Quantitative comparisons should be made to measurements from different satellite instruments, particularly those focused on remotely sensing TC thermodynamic properties [Blackwell et al., 2018]. Comparisons between the CRL and the Doppler wind lidar [Bucci et al., 2018, Zhang et al., 2018] or imaging wind and rain airborne profiler radar [Guimond et al., 2018] could provide higher-resolution kinematic measurements and facilitate the calculation of low-level turbulent fluxes of temperature and moisture. This would support an enhanced understanding of essential surface enthalpy flux processes.

Focus should be placed upon expanding the observation-model comparisons made in Chapter 4 of this dissertation. Observational comparisons can be made across multiple model resolutions to reveal the optimal model configuration given resource constraints [Jin et al., 2022, Gomez et al., 2025]. Large-eddy simulations, mesoscale models, and global models of TCs can all be tested using this comparison framework. Evaluating how different physical parameterizations represent low-level TC clouds and thermodynamics should be used to inform future model updates.

CRL data can be leveraged to study other important TC processes such as genesis, early intensification, and boundary layer height variability. While observations of TC genesis are sparse [Emanuel, 2018b, Zawislak and Zipser, 2014], the CRL captured the early intensification periods for TC Grace (2021) and TC Ian (2022) while also sampling TC Fred (2021), a case that failed to strengthen. Better resolving the convective and thermodynamic processes and asymmetries present in these cases could provide new insight into genesis processes. While dynamic and thermodynamic data are often used to quantify the atmospheric boundary layer height within TCs [Kepert et al., 2016, Zhang et al., 2013], the CRL provides a new, complementary definition, as it can resolve boundary layer cloud tops and sea-spray aerosols with unprecedented resolution. This enables comparisons between traditional boundary layer height measurements and CRL derived ones in the TC rainbands, potentially revealing the connection between low-level thermodynamics, aerosols, and clouds. These additional studies would provide new insights into the structures and life cycles

of tropical cyclones.

Overall, tropical cyclones remain the most economically destructive natural hazard [Muller et al., 2025], and their impacts on lives and infrastructure must be mitigated. To enhance forecast accuracy and reduce societal vulnerability, we must improve our understanding of TC structure and build new model validation tools. This thesis makes progress towards both of these goals by using the CRL to provide new insight into the TC eye, rainbands, and operational TC models, offering new pathways for model improvement and hazard mitigation.

Bibliography

- Sim D. Aberson. 10 Years of Hurricane Synoptic Surveillance (1997–2006). *Monthly Weather Review*, 2010. doi: 10.1175/2009MWR3090.1. URL <https://journals.ametsoc.org/view/journals/mwre/138/5/2009mwr3090.1.xml>.
- Sim D. Aberson, Jason P. Dunion, and Frank D. Marks. A Photograph of a Wavenumber-2 Asymmetry in the Eye of Hurricane Erin. *Journal of the Atmospheric Sciences*, 63(1):387–391, 2006a. ISSN 0022-4928, 1520-0469. doi: 10.1175/JAS3593.1.
- Sim D. Aberson, Michael T. Montgomery, Michael Bell, and Michael Black. Hurricane Isabel (2003): New Insights Into the Physics of Intense Storms. Part II: Extreme Localized Wind. *Bulletin of the American Meteorological Society*, 87(10):1349–1354, 2006b. ISSN 0003-0007, 1520-0477. doi: 10.1175/BAMS-87-10-1349.
- Sim D. Aberson, Altug Aksoy, Kathryn J. Sellwood, Tomislava Vukicevic, and Xuejin Zhang. Assimilation of High-Resolution Tropical Cyclone Observations with an Ensemble Kalman Filter Using HEDAS: Evaluation of 2008–11 HWRF Forecasts. *Monthly Weather Review*, 2015. doi: 10.1175/MWR-D-14-00138.1. URL <https://journals.ametsoc.org/view/journals/mwre/143/2/mwr-d-14-00138.1.xml>.
- Sim D. Aberson, Kathryn J. Sellwood, and Paul A. Leighton. Calculating Dropwindsonde Location and Time from TEMP-DROP Messages for Accurate Assimilation and Analysis. *Journal of Atmospheric and Oceanic Technology*, 2017. doi: 10.1175/JTECH-D-17-0023.1. URL <https://journals.ametsoc.org/view/journals/atot/34/8/jtech-d-17-0023.1.xml>.
- Sim D. Aberson, Jun A. Zhang, Jonathan Zawislak, Kathryn Sellwood, Robert Rogers, and Joseph J. Cione. The NCAR GPS Dropwindsonde and its impact on hurricane operations and research. *Bulletin of the American Meteorological Society*, -1, 2023. ISSN 0003-0007, 1520-0477. doi: 10.1175/BAMS-D-22-0119.1. URL <https://journals.ametsoc.org/view/journals/bams/aop/BAMS-D-22-0119.1/BAMS-D-22-0119.1.xml>.
- Samuel Adams, Austin Becker, Kyle McElroy, Noah Hallisey, Peter Stempel, Isaac Ginis, and Deborah Crowley. Ocean state rising: Storm simulation and vulnerability mapping to predict hurricane impacts for Rhode Island’s critical infrastructure. *Journal of Emergency Management (Weston, Mass.)*, 22(7):47–61, 2024. ISSN 1543-5865. doi: 10.5055/jem.0801. PMID: 38573729.
- Kyle Ahern, Mark A. Bourassa, Robert E. Hart, Jun A. Zhang, and Robert F. Rogers. Observed Kinematic and Thermodynamic Structure in the Hurricane Boundary Layer during Intensity Change. *Monthly Weather Review*, 147(8):2765–2785, 2019. ISSN 1520-0493, 0027-0644. doi: 10.1175/MWR-D-18-0380.1.

Kyle Ahern, Robert E. Hart, and Mark A. Bourassa. Asymmetric Hurricane Boundary Layer Structure during Storm Decay. Part I: Formation of Descending Inflow. *Monthly Weather Review*, 149(11):3851–3874, 2021. ISSN 1520-0493, 0027-0644. doi: 10.1175/MWR-D-21-0030.1. publisher: American Meteorological Society section: Monthly Weather Review.

Kyle Ahern, Robert E. Hart, and Mark A. Bourassa. Asymmetric Hurricane Boundary Layer Structure during Storm Decay. Part II: Secondary Eyewall Formation. *Monthly Weather Review*, 150(8):1915–1936, 2022. ISSN 1520-0493, 0027-0644. doi: 10.1175/MWR-D-21-0247.1. publisher: American Meteorological Society section: Monthly Weather Review.

Altug Aksoy, Sylvie Lorsolo, Tomislava Vukicevic, Kathryn J. Sellwood, Sim D. Aberson, and Fuqing Zhang. The HWRF Hurricane Ensemble Data Assimilation System (HEDAS) for High-Resolution Data: The Impact of Airborne Doppler Radar Observations in an OSSE. *Monthly Weather Review*, 140(6):1843–1862, 2012. ISSN 1520-0493, 0027-0644. doi: 10.1175/MWR-D-11-00212.1.

Altug Aksoy, Joseph J. Cione, Brittany A. Dahl, and Paul D. Reasor. Tropical Cyclone Data Assimilation with Coyote Uncrewed Aircraft System Observations, Very Frequent Cycling, and a New Online Quality Control Technique. *Monthly Weather Review*, 150(4):797–820, 2022. ISSN 1520-0493, 0027-0644. doi: 10.1175/MWR-D-21-0124.1.

Ghassan J. Alaka, Jason A. Sippel, Zhan Zhang, Hyun-Sook Kim, Frank D. Marks, Vijay Tallapragada, Avichal Mehra, Xuejin Zhang, Aaron Poyer, and Sundararaman G. Gopalakrishnan. Lifetime Performance of the Operational Hurricane Weather Research and Forecasting (HWRF) Model for North Atlantic Tropical Cyclones. *Bulletin of the American Meteorological Society*, -1:1–1, 2024. ISSN 0003-0007, 1520-0477. doi: 10.1175/BAMS-D-23-0139.1. URL <https://journals.ametsoc.org/view/journals/bams/aop/BAMS-D-23-0139.1/BAMS-D-23-0139.1.xml>.

A. Addison Alford, Benjamin Schenkel, Samuel Hernandez, Jun A. Zhang, Michael I. Biggerstaff, Emily Blumenauer, Thea N. Sandmæl, and Sean M. Waugh. Examining Outer Band Supercell Environments in Landfalling Tropical Cyclones Using Ground-Based Radar Analyses. *Monthly Weather Review*, 2024. doi: 10.1175/MWR-D-23-0287.1. URL <https://journals.ametsoc.org/view/journals/mwre/152/10/MWR-D-23-0287.1.xml>. section: Monthly Weather Review.

Joshua J. Alland, Brian H. Tang, Kristen L. Corbosiero, and George H. Bryan. Combined Effects of Midlevel Dry Air and Vertical Wind Shear on Tropical Cyclone Development. Part I: Down-draft Ventilation. *Journal of the Atmospheric Sciences*, 78(3):763–782, 2021a. ISSN 0022-4928, 1520-0469. doi: 10.1175/JAS-D-20-0054.1. publisher: American Meteorological Society section: Journal of the Atmospheric Sciences.

Joshua J. Alland, Brian H. Tang, Kristen L. Corbosiero, and George H. Bryan. Combined Effects of Midlevel Dry Air and Vertical Wind Shear on Tropical Cyclone Development. Part II: Radial Ventilation. *Journal of the Atmospheric Sciences*, 78(3):783–796, 2021b. ISSN 0022-4928, 1520-0469. doi: 10.1175/JAS-D-20-0055.1. publisher: American Meteorological Society section: Journal of the Atmospheric Sciences.

George R. Alvey, Ed Zipser, and Jonathan Zawislak. How Does Hurricane Edouard (2014) Evolve toward Symmetry before Rapid Intensification? A High-Resolution Ensemble Study. *Journal of the Atmospheric Sciences*, mar 1 2020. doi: 10.1175/JAS-D-18-0355.1. URL <https://journals.ametsoc.org/view/journals/jas/77/3/JAS-D-18-0355.1.xml>

<https://journals.ametsoc.org/view/journals/atsc/77/4/jas-d-18-0355.1.xml>. section: Journal of the Atmospheric Sciences.

George R. Alvey, Michael Fischer, Paul Reasor, Jonathan Zawislak, and Robert Rogers. Observed Processes Underlying the Favorable Vortex Repositioning Early in the Development of Hurricane Dorian (2019). *Monthly Weather Review*, 150(1):193–213, jan 21 2022. ISSN 1520-0493, 0027-0644. doi: 10.1175/MWR-D-21-0069.1. publisher: American Meteorological Society section: Monthly Weather Review.

George R. Alvey, Ghassan J. Alaka, Lew Gramer, and Andrew Hazelton. Evaluation of Hurricane Analysis and Forecast System (HAFS) Error Statistics Stratified by Internal Structure and Environmental Metrics. *Weather and Forecasting*, 2024. doi: 10.1175/WAF-D-24-0030.1. URL <https://journals.ametsoc.org/view/journals/wefo/aop/WAF-D-24-0030.1/WAF-D-24-0030.1.xml>. section: Weather and Forecasting.

G. Brooke Anderson, Joshua Ferreri, Mohammad Al-Hamdan, William Crosson, Andrea Schumacher, Seth Guikema, Steven Quiring, Dirk Eddelbuettel, Meilin Yan, and Roger D. Peng. Assessing United States County-Level Exposure for Research on Tropical Cyclones and Human Health. *Environmental Health Perspectives*, 128(10):107009, 2020. doi: 10.1289/EHP6976.

Karthik Balaguru, Gregory R. Foltz, L. Ruby Leung, Wenwei Xu, Dongmin Kim, Hosmay Lopez, and Robert West. Increasing Hurricane Intensification Rate Near the US Atlantic Coast. *Geophysical Research Letters*, 49(20):e2022GL099793, 2022. ISSN 1944-8007. doi: 10.1029/2022GL099793. URL <https://onlinelibrary.wiley.com/doi/10.1029/2022GL099793>.

Karthik Balaguru, Wenwei Xu, Chuan-Chieh Chang, L. Ruby Leung, David R. Judi, Samson M. Hagos, Michael F. Wehner, James P. Kossin, and Mingfang Ting. Increased U.S. coastal hurricane risk under climate change. *Science Advances*, 9(14):eadf0259, 2023. doi: 10.1126/sciadv.adf0259.

Carl E. Barnes and Gary M. Barnes. Eye and Eyewall Traits as Determined with the NOAA WP-3d Lower-Fuselage Radar. *Monthly Weather Review*, 142(9):3393–3417, 2014. ISSN 1520-0493, 0027-0644. doi: 10.1175/MWR-D-13-00375.1.

G. M. Barnes, E. J. Zipser, D. Jorgensen, and F. Marks. Mesoscale and Convective Structure of a Hurricane Rainband. *Journal of the Atmospheric Sciences*, 40(9):2125–2137, 1983. ISSN 0022-4928, 1520-0469. doi: 10.1175/1520-0469(1983)040<2125:MACSOA>2.0.CO;2.

Gary M. Barnes and Paul Fuentes. Eye Excess Energy and the Rapid Intensification of Hurricane Lili (2002). *Monthly Weather Review*, 138(4):1446–1458, 2010. ISSN 1520-0493, 0027-0644. doi: 10.1175/2009MWR3145.1.

Nicholas R. Barron, Anthony C. Didlake Jr., and Paul D. Reasor. Statistical Analysis of Convective Updrafts in Tropical Cyclone Rainbands Observed by Airborne Doppler Radar. *Journal of Geophysical Research: Atmospheres*, 127(6):e2021JD035718, 2022. ISSN 2169-8996. doi: 10.1029/2021JD035718. <https://onlinelibrary.wiley.com/doi/10.1029/2021JD035718>.

Michael M. Bell and Michael T. Montgomery. Observed Structure, Evolution, and Potential Intensity of Category 5 Hurricane Isabel (2003) from 12 to 14 September. *Monthly Weather Review*, 136(6):2023–2046, 2008. ISSN 1520-0493, 0027-0644. doi: 10.1175/2007MWR1858.1.

M. V. Bilskie and R. A. Luettich Jr. The Role of Advection in Storm Surge for Hurricane Michael (2018). *Journal of Geophysical Research: Oceans*, 129(7):e2024JC021105, 2024. ISSN 2169-9291. doi: 10.1029/2024JC021105. URL <https://onlinelibrary.wiley.com/doi/pdf/10.1029/2024JC021105>.

Michael L. Black and Hugh E. Willoughby. The Concentric Eyewall Cycle of Hurricane Gilbert. *Monthly Weather Review*, 120(6):947–957, 1992. ISSN 1520-0493, 0027-0644. doi: 10.1175/1520-0493(1992)120<0947:TCECOH>2.0.CO;2. publisher: American Meteorological Society section: Monthly Weather Review.

W. J. Blackwell, S. Braun, R. Bennartz, C. Velden, M. DeMaria, R. Atlas, J. Dunion, F. Marks, R. Rogers, B. Annane, and R. V. Leslie. An overview of the TROPICS NASA Earth Venture Mission. *Quarterly Journal of the Royal Meteorological Society*, 144(S1):16–26, 2018. ISSN 1477-870X. doi: 10.1002/qj.3290. URL <https://onlinelibrary.wiley.com/doi/pdf/10.1002/qj.3290>.

Annette M. Boehm and Michael M. Bell. Retrieved thermodynamic structure of hurricane rita (2005) from airborne multi-doppler radar data. *Journal of the Atmospheric Sciences*, 78(5):1583–1605, 2021. ISSN 0022-4928, 1520-0469. doi: 10.1175/JAS-D-20-0195.1. URL <https://journals.ametsoc.org/view/journals/atsc/78/5/JAS-D-20-0195.1.xml>. Publisher: American Meteorological Society Section: Journal of the Atmospheric Sciences.

Paul B. Bogner, Gary M. Barnes, and James L. Franklin. Conditional Instability and Shear for Six Hurricanes over the Atlantic Ocean. *Weather and Forecasting*, 15(2):192–207, 2000. ISSN 1520-0434, 0882-8156. doi: 10.1175/1520-0434(2000)015<0192:CIASFS>2.0.CO;2.

Christopher D. Bosma, Daniel B. Wright, Phu Nguyen, James P. Kossin, Derrick C. Herndon, and J. Marshall Shepherd. An Intuitive Metric to Quantify and Communicate Tropical Cyclone Rainfall Hazard. *Bulletin of the American Meteorological Society*, 101(2):E206–E220, 2020. ISSN 0003-0007, 1520-0477. doi: 10.1175/BAMS-D-19-0075.1. publisher: American Meteorological Society section: Bulletin of the American Meteorological Society.

Philippe Bougeault. The Diurnal Cycle of the Marine Stratocumulus Layer: A Higher-Order Model Study. *Journal of the Atmospheric Sciences*, 1985. ISSN 1520-0469. URL https://journals.ametsoc.org/view/journals/atsc/42/24/1520-0469_1985_042_2826_tdcotm_2_0_co_2.xml.

Léonard Boussoux, Cynthia Zeng, Théo Guénais, and Dimitris Bertsimas. Hurricane Forecasting: A Novel Multimodal Machine Learning Framework. *Weather and Forecasting*, 2022. doi: 10.1175/WAF-D-21-0091.1. URL <https://journals.ametsoc.org/view/journals/wefo/37/6/WAF-D-21-0091.1.xml>.

Scott A. Braun. A Cloud-Resolving Simulation of Hurricane Bob (1991): Storm Structure and Eyewall Buoyancy. *Monthly Weather Review*, 130(6):1573–1592, 2002. ISSN 1520-0493, 0027-0644. doi: 10.1175/1520-0493(2002)130<1573:ACRSOH>2.0.CO;2.

George H. Bryan. Effects of Surface Exchange Coefficients and Turbulence Length Scales on the Intensity and Structure of Numerically Simulated Hurricanes. *Monthly Weather Review*, 2012. doi: 10.1175/MWR-D-11-00231.1. URL <https://journals.ametsoc.org/view/journals/mwre/140/4/mwr-d-11-00231.1.xml>. section: Monthly Weather Review.

George H. Bryan and Richard Rotunno. The Influence of Near-Surface, High-Entropy Air in Hurricane Eyes on Maximum Hurricane Intensity. *Journal of the Atmospheric Sciences*, 66(1):148–158, 2009. ISSN 0022-4928, 1520-0469. doi: 10.1175/2008JAS2707.1.

George H. Bryan, John C. Wyngaard, and J. Michael Fritsch. Resolution Requirements for the Simulation of Deep Moist Convection. *Monthly Weather Review*, oct 1 2003. ISSN 1520-0493. URL https://journals.ametsoc.org/view/journals/mwre/131/10/1520-0493_2003_131_2394_rrftso_2.0.co_2.xml. section: Monthly Weather Review.

George H. Bryan, Rochelle P. Worsnop, Julie K. Lundquist, and Jun A. Zhang. A Simple Method for Simulating Wind Profiles in the Boundary Layer of Tropical Cyclones. *Boundary-Layer Meteorology*, 162(3):475–502, 2017. ISSN 1573-1472. doi: 10.1007/s10546-016-0207-0.

Lisa R. Bucci, Christopher O’Handley, G. David Emmitt, Jun A. Zhang, Kelly Ryan, and Robert Atlas. Validation of an Airborne Doppler Wind Lidar in Tropical Cyclones. *Sensors*, 18(12):4288, 2018. ISSN 1424-8220. doi: 10.3390/s18124288. number: 12 publisher: Multidisciplinary Digital Publishing Institute.

Mike Bush, Ian Boutle, John Edwards, Anke Finnenkoetter, Charmaine Franklin, Kirsty Hanley, Aravindakshan Jayakumar, Huw Lewis, Adrian Lock, Marion Mittermaier, Saji Mohandas, Rachel North, Aurore Porson, Belinda Roux, Stuart Webster, and Mark Weeks. The second Met Office Unified Model—JULES Regional Atmosphere and Land configuration, RAL2. *Geoscientific Model Development*, 16(6):1713–1734, 2023. ISSN 1991-959X. doi: 10.5194/gmd-16-1713-2023. publisher: Copernicus GmbH.

John Cangialosi, Brad Reinhart, and Jonathan Martinez. National Hurricane Center Forecast Verification Report: 2023 Hurricane Season. *NOAA Internal Publication*, 2024.

John P. Cangialosi, Eric Blake, Mark DeMaria, Andrew Penny, Andrew Latto, Edward Rappaport, and Vijay Tallapragada. Recent Progress in Tropical Cyclone Intensity Forecasting at the National Hurricane Center. *Weather and Forecasting*, 35(5):1913–1922, 2020. ISSN 1520-0434, 0882-8156. doi: 10.1175/WAF-D-20-0059.1.

Jacob D. Carstens and Allison A. Wing. Simulating Dropsondes to Assess Moist Static Energy Variability in Tropical Cyclones. *Geophysical Research Letters*, 49(15):e2022GL099101, 2022. ISSN 1944-8007. doi: 10.1029/2022GL099101. URL <https://onlinelibrary.wiley.com/doi/pdf/10.1029/2022GL099101>.

Stephanie E. Chang. Socioeconomic Impacts of Infrastructure Disruptions. In *Oxford Research Encyclopedia of Natural Hazard Science*. Oxford University Press, 2016. ISBN 978-0-19-938940-7. URL <https://oxfordre.com/naturalhazardscience/display/10.1093/acrefore/9780199389407.001.0001/acrefore-9780199389407-e-66>.

Jan-Huey Chen, Timothy Marchok, Morris Bender, Kun Gao, Sundararaman Gopalakrishnan, Lucas Harris, Andrew Hazelton, Bin Liu, Avichal Mehra, Matthew Morin, Fanglin Yang, Xuejin Zhang, Zhan Zhang, and Linjiong Zhou. Closing the gap — Hurricane Prediction Advances in the US FV3-based Models. *Bulletin of the American Meteorological Society*, pages BAMS-D-24-0036.1, may 21 2025. ISSN 0003-0007, 1520-0477. doi: 10.1175/BAMS-D-24-0036.1.

Shuyi S. Chen, John A. Knaff, and Frank D. Marks. Effects of Vertical Wind Shear and Storm Motion on Tropical Cyclone Rainfall Asymmetries Deduced from TRMM. *Monthly Weather Review*,

2006. doi: 10.1175/MWR3245.1. URL <https://journals.ametsoc.org/view/journals/mwre/134/11/mwr3245.1.xml>. section: Monthly Weather Review.
- Xiaomin Chen, George H. Bryan, Jun A. Zhang, Joseph J. Cione, and Frank D. Marks. A Framework for Simulating the Tropical Cyclone Boundary Layer Using Large-Eddy Simulation and Its Use in Evaluating PBL Parameterizations. *Journal of the Atmospheric Sciences*, 2021a. doi: 10.1175/JAS-D-20-0227.1. URL <https://journals.ametsoc.org/view/journals/atsc/78/11/JAS-D-20-0227.1.xml>.
- Xiaomin Chen, Jian-Feng Gu, Jun A. Zhang, Frank D. Marks, Robert F. Rogers, and Joseph J. Cione. Boundary Layer Recovery and Precipitation Symmetrization Preceding Rapid Intensification of Tropical Cyclones under Shear. *Journal of the Atmospheric Sciences*, 78(5):1523–1544, 2021b. ISSN 0022-4928, 1520-0469. doi: 10.1175/JAS-D-20-0252.1.
- Xiaomin Chen, Ming Xue, Bowen Zhou, Juan Fang, Jun A. Zhang, and Frank D. Marks. Effect of Scale-Aware Planetary Boundary Layer Schemes on Tropical Cyclone Intensification and Structural Changes in the Gray Zone. *Monthly Weather Review*, jun 7 2021c. doi: 10.1175/MWR-D-20-0297.1. URL <https://journals.ametsoc.org/view/journals/mwre/149/7/MWR-D-20-0297.1.xml>. section: Monthly Weather Review.
- Xiaomin Chen, George H. Bryan, Andrew Hazelton, Frank D. Marks, and Pat Fitzpatrick. Evaluation and Improvement of a TKE-Based Eddy-Diffusivity Mass-Flux (EDMF) Planetary Boundary Layer Scheme in Hurricane Conditions. *Weather and Forecasting*, 2022. doi: 10.1175/WAF-D-21-0168.1. URL <https://journals.ametsoc.org/view/journals/wefo/37/6/WAF-D-21-0168.1.xml>. section: Weather and Forecasting.
- Xiaomin Chen, Christopher M. Rozoff, Robert F. Rogers, Kristen L. Corbosiero, Dandan Tao, Jian-Feng Gu, Falko Judt, Eric A. Hendricks, Yuqing Wang, Michael M. Bell, Daniel P. Stern, Kate D. Musgrave, John A. Knaff, and John Kaplan. Research Advances on Internal Processes Affecting Tropical Cyclone Intensity Change from 2018–2022. *Tropical Cyclone Research and Review*, 2023. ISSN 2225-6032. doi: 10.1016/j.tcrr.2023.05.001. URL <https://www.sciencedirect.com/science/article/pii/S2225603223000127>. [Online; accessed 2023-05-10].
- Yueh-Li Chen and Chun-Chieh Wu. On the Two Types of Tropical Cyclone Eye Formation: Clearing Formation and Banding Formation. *Monthly Weather Review*, -1, 2022. ISSN 1520-0493, 0027-0644. doi: 10.1175/MWR-D-21-0239.1. URL <https://journals.ametsoc.org/view/journals/mwre/aop/MWR-D-21-0239.1/MWR-D-21-0239.1.xml>.
- Yueh-Li Chen and Chun-Chieh Wu. The Impact of Outer-Core Structure on Eye Formation and Intensification of Tropical Cyclones. *Monthly Weather Review*, 2025. doi: 10.1175/MWR-D-24-0004.1. URL <https://journals.ametsoc.org/view/journals/mwre/153/2/MWR-D-24-0004.1.xml>.
- Alex Alvin Cheung, Christopher J. Slocum, John A. Knaff, and Muhammad Naufal Razin. Documenting the Progressions of Secondary Eyewall Formations. *Weather and Forecasting*, 2023. doi: 10.1175/WAF-D-23-0047.1. URL <https://journals.ametsoc.org/view/journals/wefo/39/1/WAF-D-23-0047.1.xml>. section: Weather and Forecasting.
- Hui Christophersen, Altug Aksoy, Jason Dunion, and Kathryn Sellwood. The Impact of NASA Global Hawk Unmanned Aircraft Dropwindsonde Observations on Tropical Cyclone Track, In-

- tensity, and Structure: Case Studies. *Monthly Weather Review*, 145(5):1817–1830, 2017. ISSN 1520-0493, 0027-0644. doi: 10.1175/MWR-D-16-0332.1.
- Hui Christophersen, Jason Sippel, Altug Aksoy, and Nancy L. Baker. Recent advancements for tropical cyclone data assimilation. *Annals of the New York Academy of Sciences*, 1517(1):25–43, 2022. ISSN 1749-6632. doi: 10.1111/nyas.14873. URL <https://onlinelibrary.wiley.com/doi/pdf/10.1111/nyas.14873>.
- Joseph J. Cione, George H. Bryan, Ronald Dobosy, Jun A. Zhang, Gijs Boer, Altug Aksoy, Joshua B. Wadler, Evan A. Kalina, Brittany A. Dahl, Kelly Ryan, Jonathan Neuhaus, Ed Dumas, Frank D. Marks, Aaron M. Farber, Terry Hock, and Xiaomin Chen. Eye of the Storm: Observing Hurricanes with a Small Unmanned Aircraft System. *Bulletin of the American Meteorological Society*, 101(2):E186–E205, 2020. ISSN 0003-0007, 1520-0477. doi: 10.1175/BAMS-D-19-0169.1.
- Clement Combot, Alexis Mouche, John Knaff, Yili Zhao, Yuan Zhao, Leo Vinour, Yves Quilfen, and Bertrand Chapron. Extensive High-Resolution Synthetic Aperture Radar (SAR) Data Analysis of Tropical Cyclones: Comparisons with SFMR Flights and Best Track. *Monthly Weather Review*, 2020. doi: 10.1175/MWR-D-20-0005.1. URL <https://journals.ametsoc.org/view/journals/mwre/148/11/MWR-D-20-0005.1.xml>.
- Clément Combot, Alexis Mouche, Clément de Boyer Montegut, and Bertrand Chapron. Toward Comprehensive Understanding of AirSea Interactions Under Tropical Cyclones: On the Importance of High Resolution and MultiModal Observations. *Geophysical Research Letters*, 51(e2024GL110637), 2024.
- Kristen L. Corbosiero and John Molinari. The Effects of Vertical Wind Shear on the Distribution of Convection in Tropical Cyclones. *Monthly Weather Review*, 130(8):2110–2123, 2002. ISSN 1520-0493, 0027-0644. doi: 10.1175/1520-0493(2002)130<2110:TEOVWS>2.0.CO;2. publisher: American Meteorological Society section: Monthly Weather Review.
- Kristen L. Corbosiero and John Molinari. The Relationship between Storm Motion, Vertical Wind Shear, and Convective Asymmetries in Tropical Cyclones. *Journal of the Atmospheric Sciences*, 2003. ISSN 1520-0469. URL https://journals.ametsoc.org/view/journals/atsc/60/2/1520-0469_2003_060_0366_trbsmv_2.0.co_2.xml.
- Kristen L. Corbosiero, John Molinari, Anantha R. Aiyyer, and Michael L. Black. The Structure and Evolution of Hurricane Elena (1985). Part II: Convective Asymmetries and Evidence for Vortex Rossby Waves. *Monthly Weather Review*, 134(11):3073–3091, 2006. ISSN 1520-0493, 0027-0644. doi: 10.1175/MWR3250.1.
- Samantha Jo Cosgrove. Improving Technical and Risk Communication: An Organizational Study of North Carolina Emergency Management and Hurricane Florence. *IEEE Transactions on Professional Communication*, 66(3):284–299, 2023. ISSN 1558-1500. doi: 10.1109/TPC.2023.3295969.
- Thomas A. Cram, John Persing, Michael T. Montgomery, and Scott A. Braun. A Lagrangian Trajectory View on Transport and Mixing Processes between the Eye, Eyewall, and Environment Using a High-Resolution Simulation of Hurricane Bonnie (1998). *Journal of the Atmospheric Sciences*, 64(6):1835–1856, 2007. ISSN 0022-4928, 1520-0469. doi: 10.1175/JAS3921.1.

Yufan Dai, Qingqing Li, Lijuan Wang, and Hong Chen. Examining asymmetric outer-core CAPE in sheared tropical cyclones based on the FNL data set. *Frontiers of Earth Science*, 16(3):734–743, 2022. ISSN 2095-0209. doi: 10.1007/s11707-021-0920-y.

Mark DeMaria, Michelle Mainelli, Lynn K. Shay, John A. Knaff, and John Kaplan. Further improvements to the statistical hurricane intensity prediction scheme (SHIPS). *Weather and Forecasting*, 20(4):531–543, 2005. ISSN 1520-0434, 0882-8156. doi: 10.1175/WAF862.1. URL https://journals.ametsoc.org/view/journals/wefo/20/4/waf862_1.xml. Publisher: American Meteorological Society Section: Weather and Forecasting.

Mark DeMaria, James L. Franklin, Matthew J. Onderlinde, and John Kaplan. Operational Forecasting of Tropical Cyclone Rapid Intensification at the National Hurricane Center. *Atmosphere*, 12(6):683, 2021. ISSN 2073-4433. doi: 10.3390/atmos12060683.

Mark DeMaria, James L. Franklin, Rachel Zelinsky, David A. Zelinsky, Matthew J. Onderlinde, John A. Knaff, Stephanie N. Stevenson, John Kaplan, Kate D. Musgrave, Galina Chirokova, and Charles R. Sampson. The National Hurricane Center Tropical Cyclone Model Guidance Suite. *Weather and Forecasting*, 37(11):2141–2159, 2022. ISSN 0882-8156, 1520-0434. doi: 10.1175/WAF-D-22-0039.1.

Alexander J. DesRosiers and Michael M. Bell. Airborne radar quality control with machine learning. *Artificial Intelligence for the Earth Systems*, 2024. doi: 10.1175/AIES-D-23-0064.1. URL <https://journals.ametsoc.org/view/journals/aies/3/1/AIES-D-23-0064.1.xml>.

Alexander J. DesRosiers, Michael M. Bell, and Ting-Yu Cha. Vertical vortex development in hurricane michael (2018) during rapid intensification. *Monthly Weather Review*, 150(1):99–114, 2022. ISSN 1520-0493, 0027-0644. doi: 10.1175/MWR-D-21-0098.1. URL <https://journals.ametsoc.org/view/journals/mwre/150/1/MWR-D-21-0098.1.xml>. Publisher: American Meteorological Society Section: Monthly Weather Review.

Alexander J. DesRosiers, Michael M. Bell, Philip J. Klotzbach, Michael S. Fischer, and Paul D. Reasor. Observed Relationships Between Tropical Cyclone Vortex Height, Intensity, and Intensification Rate. *Geophysical Research Letters*, 50(8), 2023. ISSN 1944-8007. doi: 10.1029/2022GL101877. URL <https://onlinelibrary.wiley.com/doi/10.1029/2022GL101877>.

Anthony C. Didlake and Robert A. Houze. Convective-Scale Downdrafts in the Principal Rainband of Hurricane Katrina (2005). *Monthly Weather Review*, 137(10):3269–3293, 2009. ISSN 1520-0493, 0027-0644. doi: 10.1175/2009MWR2827.1.

Anthony C. Didlake and Robert A. Houze. Convective-Scale Variations in the Inner-Core Rainbands of a Tropical Cyclone. *Journal of the Atmospheric Sciences*, 70(2):504–523, 2013a. ISSN 0022-4928, 1520-0469. doi: 10.1175/JAS-D-12-0134.1. publisher: American Meteorological Society section: Journal of the Atmospheric Sciences.

Anthony C. Didlake and Robert A. Houze. Dynamics of the Stratiform Sector of a Tropical Cyclone Rainband. *Journal of the Atmospheric Sciences*, 70(7):1891–1911, 2013b. ISSN 0022-4928, 1520-0469. doi: 10.1175/JAS-D-12-0245.1.

Anthony C. Didlake, Gerald M. Heymsfield, Paul D. Reasor, and Stephen R. Guimond. Concentric Eyewall Asymmetries in Hurricane Gonzalo (2014) Observed by Airborne Radar.

Monthly Weather Review, 145(3):729–749, 2017. ISSN 1520-0493, 0027-0644. doi: 10.1175/MWR-D-16-0175.1.

Anthony C. Didlake, Paul D. Reasor, Robert F. Rogers, and Wen-Chau Lee. Dynamics of the Transition from Spiral Rainbands to a Secondary Eyewall in Hurricane Earl (2010). Journal of the Atmospheric Sciences, 75(9):2909–2929, 2018. ISSN 0022-4928, 1520-0469. doi: 10.1175/JAS-D-17-0348.1.

Terry Dinan. Projected Increases in Hurricane Damage in the United States: The Role of Climate Change and Coastal Development. Ecological Economics, 138:186–198, 2017. ISSN 0921-8009. doi: 10.1016/j.ecolecon.2017.03.034.

Sarah D. Ditcheck and Jason A. Sippel. A Comparison of the Impacts of Inner-Core, In-Vortex, and Environmental Dropsondes on Tropical Cyclone Forecasts during the 2017–2020 Hurricane Seasons. Weather and Forecasting, -1, 2023. ISSN 1520-0434, 0882-8156. doi: 10.1175/WAF-D-23-0055.1. URL <https://journals.ametsoc.org/view/journals/wefo/aop/WAF-D-23-0055.1/WAF-D-23-0055.1.xml>.

Sarah D. Ditcheck, Jason A. Sippel, Ghassan J. Alaka, Stanley B. Goldenberg, and Lidia Cucurull. A Systematic Assessment of the Overall Dropsonde Impact during the 2017–20 Hurricane Seasons Using the Basin-Scale HWRF. Weather and Forecasting, 38(6):789–816, 2023. ISSN 1520-0434, 0882-8156. doi: 10.1175/WAF-D-22-0102.1.

James D. Doyle, Richard M. Hodur, Sue Chen, Yi Jin, Jonathan R. Moskaitis, Shouping Wang, Eric A. Hendricks, Hao Jin, and Travis A. Smith. Tropical Cyclone Prediction Using COAMPS-Tc. Oceanography, 27(3):104–115, 2014. ISSN 1042-8275. publisher: Oceanography Society.

James D. Doyle, Jonathan R. Moskaitis, Joel W. Feldmeier, Ronald J. Ferek, Mark Beaubien, Michael M. Bell, Daniel L. Cecil, Robert L. Creasey, Patrick Duran, Russell L. Elsberry, William A. Komaromi, John Molinari, David R. Ryglicki, Daniel P. Stern, Christopher S. Velden, Xuguang Wang, Todd Allen, Bradford S. Barrett, Peter G. Black, Jason P. Dunion, Kerry A. Emanuel, Patrick A. Harr, Lee Harrison, Eric A. Hendricks, Derrick Herndon, William Q. Jeffries, Sharanya J. Majumdar, James A. Moore, Zhaoxia Pu, Robert F. Rogers, Elizabeth R. Sanabria, Gregory J. Tripoli, and Da-Lin Zhang. A View of Tropical Cyclones from Above: The Tropical Cyclone Intensity Experiment. Bulletin of the American Meteorological Society, 98(10):2113–2134, 2017. ISSN 0003-0007, 1520-0477. doi: 10.1175/BAMS-D-16-0055.1. publisher: American Meteorological Society section: Bulletin of the American Meteorological Society.

Vernon F. Dvorak. Tropical Cyclone Intensity Analysis and Forecasting from Satellite Imagery. Monthly Weather Review, 1975. ISSN 1520-0493. URL https://journals.ametsoc.org/view/journals/mwre/103/5/1520-0493_1975_103_0420_tciaaf_2_0_co_2.xml.

Matthew D. Eastin, Peter G. Black, and William M. Gray. Flight-Level Thermodynamic Instrument Wetting Errors in Hurricanes. Part I: Observations. Monthly Weather Review, 130(4):825–841, 2002. ISSN 1520-0493, 0027-0644. doi: 10.1175/1520-0493(2002)130<0825:FLTIWE>2.0.CO;2. publisher: American Meteorological Society section: Monthly Weather Review.

Matthew D. Eastin, William M. Gray, and Peter G. Black. Buoyancy of Convective Vertical Motions in the Inner Core of Intense Hurricanes. Part I: General Statistics. Monthly Weather Review, 133(1):188–208, 2005. ISSN 1520-0493, 0027-0644. doi: 10.1175/MWR-2848.1.

Roger Edwards. Tropical Cyclone Tornadoes: A Review of Knowledge in Research and Prediction. E-Journal of Severe Storms Meteorology, 7(6):1–61, 2012. ISSN 1559-5404. doi: 10.55599/ejssm.v7i6.42. number: 6.

Kerry Emanuel. Self-stratification of tropical cyclone outflow. part II: Implications for storm intensification. Journal of the Atmospheric Sciences, 69(3):988–996, 2012. ISSN 0022-4928, 1520-0469. doi: 10.1175/JAS-D-11-0177.1. URL <https://journals.ametsoc.org/view/journals/atsc/69/3/jas-d-11-0177.1.xml>. Publisher: American Meteorological Society Section: Journal of the Atmospheric Sciences.

Kerry Emanuel. Will global warming make hurricane forecasting more difficult? Bulletin of the American Meteorological Society, 98(3):495–501, 2017. ISSN 0003-0007, 1520-0477. doi: 10.1175/BAMS-D-16-0134.1. URL <https://journals.ametsoc.org/view/journals/bams/98/3/bams-d-16-0134.1.xml>. Publisher: American Meteorological Society Section: Bulletin of the American Meteorological Society.

Kerry Emanuel. 100 Years of Progress in Tropical Cyclone Research. Meteorological Monographs, 59:15.1–15.68, 2018a. ISSN 0065-9401. doi: 10.1175/AMSMONOGRAPH-D-18-0016.1.

Kerry Emanuel. 100 years of progress in tropical cyclone research. Meteorological Monographs, 59:15.1–15.68, 2018b. ISSN 0065-9401. doi: 10.1175/AMSMONOGRAPH-D-18-0016.1. URL <http://journals.ametsoc.org/doi/10.1175/AMSMONOGRAPH-D-18-0016.1>.

Kerry A. Emanuel. An air-sea interaction theory for tropical cyclones. part i: Steady-state maintenance. Journal of the Atmospheric Sciences, 43(6):585–605, 1986. ISSN 0022-4928, 1520-0469. doi: 10.1175/1520-0469(1986)043<0585:AASITF>2.0.CO;2.

Kerry A. Emanuel. Sensitivity of tropical cyclones to surface exchange coefficients and a revised steady-state model incorporating eye dynamics. Journal of the Atmospheric Sciences, 1995. ISSN 1520-0469.

Kerry A. Emanuel. Some Aspects of Hurricane Inner-Core Dynamics and Energetics. Journal of the Atmospheric Sciences, 54(8):1014–1026, 1997. ISSN 0022-4928, 1520-0469. doi: 10.1175/1520-0469(1997)054<1014:SAOHIC>2.0.CO;2.

C. W. Fairall, E. F. Bradley, J. E. Hare, A. A. Grachev, and J. B. Edson. Bulk Parameterization of Air–Sea Fluxes: Updates and Verification for the COARE Algorithm. Journal of Climate, 2003. ISSN 1520-0442. URL https://journals.ametsoc.org/view/journals/clim/16/4/1520-0442_2003_016_0571_bpoasf_2.0.co_2.xml.

Peter M. Finocchio and Sharanya J. Majumdar. A Statistical Perspective on Wind Profiles and Vertical Wind Shear in Tropical Cyclone Environments of the Northern Hemisphere. Monthly Weather Review, 145(1):361–378, jan 1 2017. ISSN 1520-0493, 0027-0644. doi: 10.1175/MWR-D-16-0221.1. publisher: American Meteorological Society section: Monthly Weather Review.

Peter M. Finocchio and Rosimar Rios-Berrios. The Intensity- and Size-Dependent Response of Tropical Cyclones to Increasing Vertical Wind Shear. Journal of the Atmospheric Sciences, sep 21 2021. ISSN 0022-4928, 1520-0469. doi: 10.1175/JAS-D-21-0126.1. URL <https://journals.ametsoc.org/view/journals/atsc/aop/JAS-D-21-0126.1/JAS-D-21-0126.1.xml>. [Online; accessed 2023-01-27].

Michael S. Fischer, Brian H. Tang, Kristen L. Corbosiero, and Christopher M. Rozoff. Normalized Convective Characteristics of Tropical Cyclone Rapid Intensification Events in the North Atlantic and Eastern North Pacific. *Monthly Weather Review*, 146(4):1133–1155, 2018. ISSN 1520-0493, 0027-0644. doi: 10.1175/MWR-D-17-0239.1.

Michael S. Fischer, Brian H. Tang, and Kristen L. Corbosiero. A Climatological Analysis of Tropical Cyclone Rapid Intensification in Environments of Upper-Tropospheric Troughs. *Monthly Weather Review*, 147(10):3693–3719, 2019. ISSN 1520-0493, 0027-0644. doi: 10.1175/MWR-D-19-0013.1.

Michael S. Fischer, Robert F. Rogers, and Paul D. Reasor. The Rapid Intensification and Eyewall Replacement Cycles of Hurricane Irma (2017). *Monthly Weather Review*, 148(3):981–1004, 2020. ISSN 1520-0493, 0027-0644. doi: 10.1175/MWR-D-19-0185.1.

Michael S. Fischer, Paul D. Reasor, Robert F. Rogers, and John F. Gamache. An Analysis of Tropical Cyclone Vortex and Convective Characteristics in Relation to Storm Intensity Using a Novel Airborne Doppler Radar Database. *Monthly Weather Review*, 150(9):2255–2278, 2022. ISSN 1520-0493, 0027-0644. doi: 10.1175/MWR-D-21-0223.1.

Michael S. Fischer, Robert F. Rogers, Paul D. Reasor, and Jason P. Dunion. An Observational Analysis of the Relationship between Tropical Cyclone Vortex Tilt, Precipitation Structure, and Intensity Change. *Monthly Weather Review*, 152(1):203–225, 2023. ISSN 1520-0493, 0027-0644. doi: 10.1175/MWR-D-23-0089.1.

Robert D. Fletcher, James R. Smith, and Robert C. Bundgaard. Superior Photographic Reconnaissance of Tropical Cyclones. *Weatherwise*, 14(3):102–109, 1961. ISSN 0043-1672. doi: 10.1080/00431672.1961.9930014.

Angela Francis and Brian Strahl. Joint Typhoon Warning Center Annual Tropical Cyclone Report: 2020. [FIX JOURNAL](#), 2020.

Cody Fritz, Zhuo Wang, Stephen W. Nesbitt, and Timothy J. Dunkerton. Vertical structure and contribution of different types of precipitation during Atlantic tropical cyclone formation as revealed by TRMM PR. *Geophysical Research Letters*, 43(2):894–901, 2016. ISSN 1944-8007. doi: 10.1002/2015GL067122. eprint: <https://onlinelibrary.wiley.com/doi/pdf/10.1002/2015GL067122>.

Tobias Geiger, Katja Frieler, and Anders Levermann. High-income does not protect against hurricane losses. *Environmental Research Letters*, 11(8):084012, 2016. ISSN 1748-9326. doi: 10.1088/1748-9326/11/8/084012.

Megan S. Gentry and Gary M. Lackmann. Sensitivity of simulated tropical cyclone structure and intensity to horizontal resolution. *Monthly Weather Review*, 138(3):688–704, 2010. ISSN 1520-0493, 0027-0644. doi: 10.1175/2009MWR2976.1. URL <https://journals.ametsoc.org/view/journals/mwre/138/3/2009mwr2976.1.xml>. Publisher: American Meteorological Society Section: Monthly Weather Review.

Miguel Sanchez Gomez, Georgios Deskos, and Julie K. Lundquist. Toward understanding the differences between mesoscale and large-eddy simulations of tropical cyclones. *Journal of the Atmospheric Sciences*, may 20 2025. doi: 10.1175/JAS-D-24-0131.1. URL <https://journals>.

ametsoc.org/view/journals/atsc/aop/JAS-D-24-0131.1/JAS-D-24-0131.1.xml. section: Journal of the Atmospheric Sciences.

Sundararaman Gopalakrishnan, Andrew Hazelton, and Jun A. Zhang. Improving Hurricane Boundary Layer Parameterization Scheme Based on Observations. *Earth and Space Science*, 8(3):e2020EA001422, 2021. ISSN 2333-5084. doi: 10.1029/2020EA001422. URL <https://onlinelibrary.wiley.com/doi/pdf/10.1029/2020EA001422>.

Sundararaman G. Gopalakrishnan, Frank Marks, Xuejin Zhang, Jian-Wen Bao, Kao-San Yeh, and Robert Atlas. The experimental HWRF system: A study on the influence of horizontal resolution on the structure and intensity changes in tropical cyclones using an idealized framework. *Monthly Weather Review*, 139(6):1762–1784, 2011. ISSN 1520-0493, 0027-0644. doi: 10.1175/2010MWR3535.1. URL <https://journals.ametsoc.org/view/journals/mwre/139/6/2010mwr3535.1.xml>. Publisher: American Meteorological Society Section: Monthly Weather Review.

Sundararaman G. Gopalakrishnan, Frank Marks, Jun A. Zhang, Xuejin Zhang, Jian-Wen Bao, and Vijay Tallapragada. A Study of the Impacts of Vertical Diffusion on the Structure and Intensity of the Tropical Cyclones Using the High-Resolution HWRF System. *Journal of the Atmospheric Sciences*, 2013. doi: 10.1175/JAS-D-11-0340.1. URL <https://journals.ametsoc.org/view/journals/atsc/70/2/jas-d-11-0340.1.xml>. section: Journal of the Atmospheric Sciences.

Avantika Gori, Ning Lin, Dazhi Xi, and Kerry Emanuel. Tropical cyclone climatology change greatly exacerbates US extreme rainfall–surge hazard. *Nature Climate Change*, 12(2):171–178, 2022. ISSN 1758-6798. doi: 10.1038/s41558-021-01272-7.

Avantika Gori, Ning Lin, Benjamin Schenkel, and Daniel Chavas. North Atlantic Tropical Cyclone Size and Storm Surge Reconstructions From 1950-Present. *Journal of Geophysical Research: Atmospheres*, 128(5):e2022JD037312, 2023. ISSN 2169-8996. doi: 10.1029/2022JD037312. URL <https://onlinelibrary.wiley.com/doi/pdf/10.1029/2022JD037312>.

Avantika Gori, Ning Lin, Daniel Chavas, Michael Oppenheimer, and Siyuan Xian. Sensitivity of tropical cyclone risk across the US to changes in storm climatology and socioeconomic growth. *Environmental Research Letters*, 20(6):064050, 2025. ISSN 1748-9326. doi: 10.1088/1748-9326/add60d. URL <https://dx.doi.org/10.1088/1748-9326/add60d>.

Sarah M. Griffin, Anthony Wimmers, and Christopher S. Velden. Predicting Rapid Intensification in North Atlantic and Eastern North Pacific Tropical Cyclones Using a Convolutional Neural Network. *Weather and Forecasting*, 2022. doi: 10.1175/WAF-D-21-0194.1. URL <https://journals.ametsoc.org/view/journals/wefo/37/8/WAF-D-21-0194.1.xml>.

Jian-Feng Gu, Zhe-Min Tan, and Xin Qiu. Quadrant-Dependent Evolution of Low-Level Tangential Wind of a Tropical Cyclone in the Shear Flow. *Journal of the Atmospheric Sciences*, 2016. doi: 10.1175/JAS-D-15-0165.1. URL <https://journals.ametsoc.org/view/journals/atsc/73/3/jas-d-15-0165.1.xml>.

Stephen R. Guimond, Gerald M. Heymsfield, Paul D. Reasor, and Anthony C. Didlake. The Rapid Intensification of Hurricane Karl (2010): New Remote Sensing Observations of Convective Bursts from the Global Hawk Platform. *Journal of the Atmospheric Sciences*, 73(9):3617–3639, 2016. ISSN 0022-4928, 1520-0469. doi: 10.1175/JAS-D-16-0026.1.

Stephen R. Guimond, Jun A. Zhang, Joseph W. Sapp, and Stephen J. Frasier. Coherent Turbulence in the Boundary Layer of Hurricane Rita (2005) during an Eyewall Replacement Cycle. *Journal of the Atmospheric Sciences*, 75(9):3071–3093, 2018. ISSN 0022-4928, 1520-0469. doi: 10.1175/JAS-D-17-0347.1. publisher: American Meteorological Society section: Journal of the Atmospheric Sciences.

Oscar Guzman and Haiyan Jiang. Heavier Inner-Core Rainfall of Major Hurricanes in the North Atlantic Basin Than in Other Global Basins. *Journal of Climate*, 2021. doi: 10.1175/JCLI-D-20-0668.1. URL <https://journals.ametsoc.org/view/journals/clim/34/14/JCLI-D-20-0668.1.xml>. section: Journal of Climate.

Oscar Guzman and Haiyan Jiang. Climatology of Tropical Cyclone Rainfall Magnitude at Different Landfalling Stages: An Emphasis on After-Landfall Rain. *Journal of Applied Meteorology and Climatology*, 2023. doi: 10.1175/JAMC-D-22-0055.1. URL <https://journals.ametsoc.org/view/journals/apmc/62/7/JAMC-D-22-0055.1.xml>. section: Journal of Applied Meteorology and Climatology.

Andrew Hagen, John Cangialosi, Marc Chenard, Laura Alaka, and Sandy Delgado. Tropical Cyclone Report: Hurricane Helene (AL092024). *National Hurricane Center Special Report*, 2025.

J. B. Halverson, J. Simpson, G. Heymsfield, H. Pierce, T. Hock, and L. Ritchie. Warm Core Structure of Hurricane Erin Diagnosed from High Altitude Dropsondes during CAMEX-4. *Journal of the Atmospheric Sciences*, 63(1):309–324, 2006. ISSN 0022-4928, 1520-0469. doi: 10.1175/JAS3596.1.

Andrew T. Hazelton and Robert E. Hart. Hurricane eyewall slope as determined from airborne radar reflectivity data: Composites and case studies. *Weather and Forecasting*, 28(2):368–386, 2013. ISSN 1520-0434, 0882-8156. doi: 10.1175/WAF-D-12-00037.1. URL https://journals.ametsoc.org/view/journals/wefo/28/2/waf-d-12-00037_1.xml. Publisher: American Meteorological Society Section: Weather and Forecasting.

Andrew T. Hazelton, Robert Rogers, and Robert E. Hart. Shear-Relative Asymmetries in Tropical Cyclone Eyewall Slope. *Monthly Weather Review*, 143(3):883–903, 2015. ISSN 1520-0493, 0027-0644. doi: 10.1175/MWR-D-14-00122.1.

Andrew T. Hazelton, Robert F. Rogers, and Robert E. Hart. Analyzing Simulated Convective Bursts in Two Atlantic Hurricanes. Part I: Burst Formation and Development. *Monthly Weather Review*, 145(8):3073–3094, 2017. ISSN 1520-0493, 0027-0644. doi: 10.1175/MWR-D-16-0267.1.

Julian T. Heming, Fernando Prates, Morris A. Bender, Rebecca Bowyer, John Cangialosi, Phillippe Caroff, Thomas Coleman, James D. Doyle, Anumeha Dube, Ghislain Faure, Jim Fraser, Brian C. Howell, Yohko Igarashi, Ron McTaggart-Cowan, M. Mohapatra, Jonathan R. Moskaitis, Jim Murtha, Rabi Rivett, M. Sharma, Chris J. Short, Amit A. Singh, Vijay Tallapragada, Helen A. Titley, and Yi Xiao. Review of Recent Progress in Tropical Cyclone Track Forecasting and Expression of Uncertainties. *Tropical Cyclone Research and Review*, 8(4):181–218, 2019. ISSN 2225-6032. doi: 10.1016/j.tctr.2020.01.001.

Deanna A. Hence and Robert A. Houze. Vertical Structure of Tropical Cyclone Rainbands as Seen by the TRMM Precipitation Radar. *Journal of the Atmospheric Sciences*, 69(9):2644–2661, 2012. ISSN 0022-4928, 1520-0469. doi: 10.1175/JAS-D-11-0323.1.

- Deanna A. Hence and Robert A. Houze Jr. Kinematic structure of convective-scale elements in the rainbands of Hurricanes Katrina and Rita (2005). *Journal of Geophysical Research: Atmospheres*, 113(D15), 2008. ISSN 2156-2202. doi: 10.1029/2007JD009429. URL <https://onlinelibrary.wiley.com/doi/abs/10.1029/2007JD009429>. eprint: <https://onlinelibrary.wiley.com/doi/pdf/10.1029/2007JD009429>.
- Eric A. Hendricks. Internal dynamical control on tropical cyclone intensity variability – a review. *Tropical Cyclone Research and Review*, 1(1):97–105, 2012. ISSN 2225-6032. doi: 10.6057/2012TCRR01.11. URL <https://www.sciencedirect.com/science/article/pii/S2225603218300201>.
- Eric A. Hendricks, Melinda S. Peng, Bing Fu, and Tim Li. Quantifying Environmental Control on Tropical Cyclone Intensity Change. *Monthly Weather Review*, 2010. doi: 10.1175/2010MWR3185.1. URL <https://journals.ametsoc.org/view/journals/mwre/138/8/2010mwr3185.1.xml>.
- Kevin A. Hill and Gary M. Lackmann. Influence of Environmental Humidity on Tropical Cyclone Size. *Monthly Weather Review*, 2009. doi: 10.1175/2009MWR2679.1. URL <https://journals.ametsoc.org/view/journals/mwre/137/10/2009mwr2679.1.xml>.
- Tomohito Hioki and Kazuhisa Tsuboki. Trajectory Analyses on the Warm Core Development and Pressure Falls of a Developing Typhoon as Simulated by a Cloud-Resolving Model. *Journal of the Meteorological Society of Japan. Ser. II*, 99(5):1329–1350, 2021. doi: 10.2151/jmsj.2021-064.
- Soichiro Hirano, Kosuke Ito, Hiroyuki Yamada, Satoki Tsujino, Kazuhisa Tsuboki, and Chun-Chieh Wu. Deep Eye Clouds in Tropical Cyclone Trami (2018) during T-PARCII Dropsonde Observations. *Journal of the Atmospheric Sciences*, 79(3):683–703, 2022. ISSN 0022-4928, 1520-0469. doi: 10.1175/JAS-D-21-0192.1.
- Terrence F. Hock and James L. Franklin. The NCAR GPS Dropwindsonde. *Bulletin of the American Meteorological Society*, 80(3):407–420, 1999. ISSN 0003-0007, 1520-0477. doi: 10.1175/1520-0477(1999)080<0407:TNGD>2.0.CO;2.
- Heather M. Holbach, Olivier Bousquet, Lisa Bucci, Paul Chang, Joe Cione, Sarah Ditchek, Jim Doyle, Jean-Philippe Duvel, Jack Elston, Gustavo Goni, Kai Kwong Hon, Kosuke Ito, Zorana Jelenak, Xiaotu Lei, Rick Lumpkin, Clive R. McMahon, Christopher Reason, Elizabeth Sanabia, Lynn Keith Shay, Jason A. Sippel, Andrey Sushko, Jie Tang, Kazuhisa Tsuboki, Hiroyuki Yamada, Jonathan Zawislak, and Jun A. Zhang. Recent advancements in aircraft and in situ observations of tropical cyclones. *Tropical Cyclone Research and Review*, 12(2):81–99, 2023. ISSN 2225-6032. doi: 10.1016/j.tcrr.2023.06.001.
- Song-You Hong, Yign Noh, and Jimy Dudhia. A New Vertical Diffusion Package with an Explicit Treatment of Entrainment Processes. *Monthly Weather Review*, 134(9):2318–2341, 2006. ISSN 1520-0493, 0027-0644. doi: 10.1175/MWR3199.1. publisher: American Meteorological Society section: Monthly Weather Review.
- Robert A. Houze. Stratiform Precipitation in Regions of Convection: A Meteorological Paradox? *Bulletin of the American Meteorological Society*, 78(10):2179–2196, 1997. ISSN 0003-0007, 1520-0477. doi: 10.1175/1520-0477(1997)078<2179:SPIROC>2.0.CO;2. publisher: American Meteorological Society section: Bulletin of the American Meteorological Society.

Robert A. Houze. Clouds in Tropical Cyclones. *Monthly Weather Review*, 138(2):293–344, 2010. ISSN 1520-0493, 0027-0644. doi: 10.1175/2009MWR2989.1.

Robert A. Houze, Shuyi S. Chen, Wen-Chau Lee, Robert F. Rogers, James A. Moore, Gregory J. Stossmeister, Michael M. Bell, Jasmine Cetrone, Wei Zhao, and S. Rita Brodzik. The Hurricane Rainband and Intensity Change Experiment: Observations and Modeling of Hurricanes Katrina, Ophelia, and Rita. *Bulletin of the American Meteorological Society*, 87(11):1503–1522, 2006. ISSN 0003-0007, 1520-0477. doi: 10.1175/BAMS-87-11-1503. publisher: American Meteorological Society section: Bulletin of the American Meteorological Society.

Robert A. Houze, Shuyi S. Chen, Bradley F. Smull, Wen-Chau Lee, and Michael M. Bell. Hurricane Intensity and Eyewall Replacement. *Science*, 315(5816):1235–1239, 2007. doi: 10.1126/science.1135650.

L. Hu, T. Wen, Y. Shao, Q. Wang, W. Fang, J. Yang, M. Liu, X. Wang, H. Zhang, J. Bi, and Z. Ma. Economic Impacts of Tropical Cyclone-Induced Multiple Hazards in China. *Earth's Future*, 11(9):e2023EF003622, 2023. ISSN 2328-4277. doi: 10.1029/2023EF003622. URL <https://onlinelibrary.wiley.com/doi/10.1029/2023EF003622>.

Virginia Iglesias, Anna E. Braswell, Matthew W. Rossi, Maxwell B. Joseph, Caitlin McShane, Megan Cattau, Michael J. Koontz, Joe McGlinchy, R. Chelsea Nagy, Jennifer Balch, Stefan Leyk, and William R. Travis. Risky Development: Increasing Exposure to Natural Hazards in the United States. *Earth's Future*, 9(7):e2020EF001795, 2021. ISSN 2328-4277. doi: 10.1029/2020EF001795. URL <https://onlinelibrary.wiley.com/doi/10.1029/2020EF001795>.

Yasutaka Ikuta and Udai Shimada. Impact of Assimilation of the Tropical Cyclone Strong Winds Observed by Synthetic Aperture Radar on Analyses and Forecasts. *Monthly Weather Review*, -1, 2024. ISSN 1520-0493, 0027-0644. doi: 10.1175/MWR-D-23-0103.1. URL <https://journals.ametsoc.org/view/journals/mwre/aop/MWR-D-23-0103.1/MWR-D-23-0103.1.xml>.

Jasmine B. D. Jaffrés and Jessie L. Gray. Chasing rainfall: estimating event precipitation along tracks of tropical cyclones via reanalysis data and in-situ gauges. *Environmental Modelling & Software*, 167:105773, 2023. ISSN 1364-8152. doi: 10.1016/j.envsoft.2023.105773.

Haiyan Jiang, Peter G. Black, Edward J. Zipser, Frank D. Marks, and Eric W. Uhlhorn. Validation of Rain-Rate Estimation in Hurricanes from the Stepped Frequency Microwave Radiometer: Algorithm Correction and Error Analysis. *Journal of the Atmospheric Sciences*, jan 1 2006. doi: 10.1175/JAS3605.1. URL <https://journals.ametsoc.org/view/journals/atsc/63/1/jas3605.1.xml>. section: Journal of the Atmospheric Sciences.

Haiyan Jiang, Cheng Tao, and Yongxian Pei. Estimation of Tropical Cyclone Intensity in the North Atlantic and Northeastern Pacific Basins Using TRMM Satellite Passive Microwave Observations. *Journal of Applied Meteorology and Climatology*, 58(2):185–197, 2019. ISSN 1558-8424, 1558-8432. doi: 10.1175/JAMC-D-18-0094.1.

Hao Jin, Melinda S. Peng, Yi Jin, and James D. Doyle. An evaluation of the impact of horizontal resolution on tropical cyclone predictions using COAMPS-TC. *Weather and Forecasting*, 29(2):252–270, 2014. ISSN 1520-0434, 0882-8156. doi: 10.1175/WAF-D-13-00054.1. URL https://journals.ametsoc.org/view/journals/wefo/29/2/waf-d-13-00054_1.xml. Publisher: American Meteorological Society Section: Weather and Forecasting.

Hao Jin, Jonathan R. Moskaitis, Yi Jin, and James D. Doyle. Resolution Impact on Rapid Intensification and Structure Change of Super Typhoon Hagibis (2019). *Journal of the Meteorological Society of Japan. Ser. II*, 100(6):943–964, 2022. ISSN 0026-1165, 2186-9057. doi: 10.2151/jmsj.2022-049.

Amethyst A. Johnson, Juliane Schwendike, Andrew N. Ross, Adrian Lock, John M. Edwards, and Jeffrey D. Kepert. Impacts of free tropospheric turbulence parametrisation on a sheared tropical cyclone. *Quarterly Journal of the Royal Meteorological Society*, n/a, 2024. ISSN 1477-870X. doi: 10.1002/qj.4823. URL <https://onlinelibrary.wiley.com/doi/abs/10.1002/qj.4823>. eprint: <https://onlinelibrary.wiley.com/doi/pdf/10.1002/qj.4823>.

Sarah C. Jones, Patrick A. Harr, Jim Abraham, Lance F. Bosart, Peter J. Bowyer, Jenni L. Evans, Deborah E. Hanley, Barry N. Hanstrum, Robert E. Hart, François Lalaurette, Mark R. Sinclair, Roger K. Smith, and Chris Thorncroft. The Extratropical Transition of Tropical Cyclones: Forecast Challenges, Current Understanding, and Future Directions. *Weather and Forecasting*, 2003. ISSN 1520-0434. URL https://journals.ametsoc.org/view/journals/wefo/18/6/1520-0434_2003_018_1052_tetotc_2_0_co_2.xml. section: Weather and Forecasting.

Thomas Jones, Patrick Skinner, Nusrat Yussouf, Kent Knopfmeier, Anthony Reinhart, and David Dowell. Forecasting High-Impact Weather in Landfalling Tropical Cyclones Using a Warn-on-Forecast System. *Bulletin of the American Meteorological Society*, 2019. doi: 10.1175/BAMS-D-18-0203.1. URL <https://journals.ametsoc.org/view/journals/bams/100/8/bams-d-18-0203.1.xml>. section: Bulletin of the American Meteorological Society.

C. L. Jordan. Marked Changes in the Characteristics of the Eye of Intense Typhoons Between the Deepening and Filling Stages. *Journal of the Atmospheric Sciences*, 18(6):779–789, 1961. ISSN 1520-0469. doi: 10.1175/1520-0469(1961)018<0779:MCITCO>2.0.CO;2.

Charles L. Jordan. On the low-level structure of the typhoon eye. *Journal of the Atmospheric Sciences*, 9(4):285–290, 1952. ISSN 1520-0469. doi: 10.1175/1520-0469(1952)009<0285:OTLLSO>2.0.CO;2. URL https://journals.ametsoc.org/view/journals/atsc/9/4/1520-0469_1952_009_0285_otllso_2_0_co_2.xml. Publisher: American Meteorological Society Section: Journal of the Atmospheric Sciences.

David P. Jorgensen. Mesoscale and Convective-Scale Characteristics of Mature Hurricanes. Part II. Inner Core Structure of Hurricane Allen (1980). *Journal of the Atmospheric Sciences*, 41(8):1287–1311, 1984. ISSN 0022-4928, 1520-0469. doi: 10.1175/1520-0469(1984)041<1287:MACSCO>2.0.CO;2.

John S. Kain and J. Michael Fritsch. *Convective Parameterization for Mesoscale Models: The Kain-Fritsch Scheme*, pages 165–170. American Meteorological Society, Boston, MA, 1993. ISBN 978-1-935704-13-3. URL https://doi.org/10.1007/978-1-935704-13-3_16. DOI: 10.1007/978-1-935704-13-3_16.

John Kaplan and Mark DeMaria. Large-Scale Characteristics of Rapidly Intensifying Tropical Cyclones in the North Atlantic Basin. *Weather and Forecasting*, 18(6):1093–1108, 2003. ISSN 1520-0434, 0882-8156. doi: 10.1175/1520-0434(2003)018<1093:LCORIT>2.0.CO;2.

John Kaplan, Mark DeMaria, and John A. Knaff. A Revised Tropical Cyclone Rapid Intensification Index for the Atlantic and Eastern North Pacific Basins. *Weather and Forecasting*, 25(1):220–241, 2010. ISSN 1520-0434, 0882-8156. doi: 10.1175/2009WAF2222280.1.

Jeffrey D. Kepert. Choosing a Boundary Layer Parameterization for Tropical Cyclone Modeling. *Monthly Weather Review*, 2012. doi: 10.1175/MWR-D-11-00217.1. URL <https://journals.ametsoc.org/view/journals/mwre/140/5/mwr-d-11-00217.1.xml>. section: Monthly Weather Review.

Jeffrey D. Kepert, Juliane Schwendike, and Hamish Ramsay. Why is the Tropical Cyclone Boundary Layer Not “Well Mixed”? *Journal of the Atmospheric Sciences*, 2016. doi: 10.1175/JAS-D-15-0216.1. URL <https://journals.ametsoc.org/view/journals/atsc/73/3/jas-d-15-0216.1.xml>. section: Journal of the Atmospheric Sciences.

Stanley Q. Kidder and Thomas H. Vonder Haar. *Satellite Meteorology: An Introduction*. Elsevier, 1995. ISBN 978-0-08-057200-0. Google-Books-ID: M5dsBgAAQBAJ.

Jeong-Hwan Kim, Yoo-Geun Ham, Daehyun Kim, Tim Li, and Chen Ma. Improvement in Forecasting Short-Term Tropical Cyclone Intensity Change and Their Rapid Intensification Using Deep Learning. *Artificial Intelligence for the Earth Systems*, 2024a. doi: 10.1175/AIES-D-23-0052.1. URL <https://journals.ametsoc.org/view/journals/aies/3/2/AIES-D-23-0052.1.xml>.

Sung-Hun Kim, Woojeong Lee, Hyoun-Woo Kang, and Sok Kuh Kang. Predicting rapid intensification of tropical cyclones in the western North Pacific: a machine learning and net energy gain rate approach. *Frontiers in Marine Science*, 10, 2024b. ISSN 2296-7745. URL <https://www.frontiersin.org/articles/10.3389/fmars.2023.1296274>. [Online; accessed 2024-02-02].

Philip J. Klotzbach, Steven G. Bowen, Roger Pielke, and Michael Bell. Continental U.S. Hurricane Landfall Frequency and Associated Damage: Observations and Future Risks. *Bulletin of the American Meteorological Society*, 99(7):1359–1376, 2018. ISSN 0003-0007, 1520-0477. doi: 10.1175/BAMS-D-17-0184.1.

Philip J. Klotzbach, Kimberly M. Wood, Carl J. Schreck III, Steven G. Bowen, Christina M. Patricola, and Michael M. Bell. Trends in Global Tropical Cyclone Activity: 1990–2021. *Geophysical Research Letters*, 49(6):e2021GL095774, 2022. ISSN 1944-8007. doi: 10.1029/2021GL095774. URL <https://onlinelibrary.wiley.com/doi/10.1029/2021GL095774>.

Kenneth R. Knapp, Steve Ansari, Caroline L. Bain, Mark A. Bourassa, Michael J. Dickinson, Chris Funk, Chip N. Helms, Christopher C. Hennon, Christopher D. Holmes, George J. Huffman, James P. Kossin, Hai-Tien Lee, Alexander Loew, and Gudrun Magnusdottir. Globally Gridded Satellite Observations for Climate Studies. *Bulletin of the American Meteorological Society*, 2011. doi: 10.1175/2011BAMS3039.1. URL https://journals.ametsoc.org/view/journals/bams/92/7/2011bams3039_1.xml.

Kenneth R. Knapp, Christopher S. Velden, and Anthony J. Wimmers. A Global Climatology of Tropical Cyclone Eyes. *Monthly Weather Review*, 146(7):2089–2101, 2018. ISSN 1520-0493, 0027-0644. doi: 10.1175/MWR-D-17-0343.1.

William A. Komaromi and James D. Doyle. Tropical Cyclone Outflow and Warm Core Structure as Revealed by HS3 Dropsonde Data. *Monthly Weather Review*, 145(4):1339–1359, 2017. ISSN 1520-0493, 0027-0644. doi: 10.1175/MWR-D-16-0172.1. publisher: American Meteorological Society section: Monthly Weather Review.

William A. Komaromi, Patrick A. Reinecke, James D. Doyle, and Jonathan R. Moskaitis. The Naval Research Laboratory's Coupled Ocean–Atmosphere Mesoscale Prediction System-Tropical Cyclone Ensemble (COAMPS-TC Ensemble). *Weather and Forecasting*, 36(2):499–517, 2021. ISSN 1520-0434, 0882-8156. doi: 10.1175/WAF-D-20-0038.1.

Michael V. Kopelman, Allison A. Wing, and Jacob D. Carstens. Spatial Variability of Dropsonde-Derived Moist Static Energy in North Atlantic Tropical Cyclones. *Geophysical Research Letters*, 51(20):e2024GL111086, 2024. ISSN 1944-8007. doi: 10.1029/2024GL111086. URL <https://onlinelibrary.wiley.com/doi/pdf/10.1029/2024GL111086>.

James P. Kossin and Matthew D. Eastin. Two Distinct Regimes in the Kinematic and Thermo-dynamic Structure of the Hurricane Eye and Eyewall. *Journal of the Atmospheric Sciences*, 58(9):1079–1090, 2001. ISSN 0022-4928, 1520-0469. doi: 10.1175/1520-0469(2001)058<1079:TDRITK>2.0.CO;2.

James P. Kossin and Wayne H. Schubert. Mesovortices in Hurricane Isabel. *Bulletin of the American Meteorological Society*, 85(2):151–153, 2004. ISSN 0003-0007.

James P. Kossin, Brian D. McNoldy, and Wayne H. Schubert. Vortical swirls in hurricane eye clouds. *Monthly Weather Review*, 130(12):3144–3149, 2002. ISSN 1520-0493, 0027-0644. doi: 10.1175/1520-0493(2002)130<3144:VSIHEC>2.0.CO;2. URL https://journals.ametsoc.org/view/journals/mwre/130/12/1520-0493_2002_130_3144_vsihec_2.0.co_2.xml.

James P. Kossin, John A. Knaff, Howard I. Berger, Derrick C. Herndon, Thomas A. Cram, Christopher S. Velden, Richard J. Murnane, and Jeffrey D. Hawkins. Estimating Hurricane Wind Structure in the Absence of Aircraft Reconnaissance. *Weather and Forecasting*, 2007. doi: 10.1175/WAF985.1. URL https://journals.ametsoc.org/view/journals/wefo/22/1/waf985_1.xml.

M. Kunz, B. Mühr, T. Kunz-Plapp, J. E. Daniell, B. Khazai, F. Wenzel, M. Vannieuwenhuyse, T. Comes, F. Elmer, K. Schröter, J. Fohringer, T. Münzberg, C. Lucas, and J. Zschau. Investigation of superstorm Sandy 2012 in a multi-disciplinary approach. *Natural Hazards and Earth System Sciences*, 13(10):2579–2598, 2013. ISSN 1561-8633. doi: 10.5194/nhess-13-2579-2013. publisher: Copernicus GmbH.

Sally L. Lavender and John L. McBride. Global climatology of rainfall rates and lifetime accumulated rainfall in tropical cyclones: Influence of cyclone basin, cyclone intensity and cyclone size. *International Journal of Climatology*, 41(S1):E1217–E1235, 2021. ISSN 1097-0088. doi: 10.1002/joc.6763. URL <https://onlinelibrary.wiley.com/doi/pdf/10.1002/joc.6763>.

Yu-Ju Lee, David Hall, Quan Liu, Wen-Wei Liao, and Ming-Chun Huang. Interpretable tropical cyclone intensity estimation using Dvorak-inspired machine learning techniques. *Engineering Applications of Artificial Intelligence*, 101:104233, 2021. ISSN 0952-1976. doi: 10.1016/j.engappai.2021.104233.

Qingqing Li and Yuqing Wang. A Comparison of Inner and Outer Spiral Rainbands in a Numerically Simulated Tropical Cyclone. *Monthly Weather Review*, 2012. doi: 10.1175/MWR-D-11-00237.1. URL <https://journals.ametsoc.org/view/journals/mwre/140/9/mwr-d-11-00237.1.xml>. section: Monthly Weather Review.

Xiaofeng Li, editor. *Hurricane Monitoring With Spaceborne Synthetic Aperture Radar*. Springer Natural Hazards. Springer, Singapore, 2017. ISBN 978-981-10-2892-2. URL <http://link.springer.com/10.1007/978-981-10-2893-9>. DOI: 10.1007/978-981-10-2893-9.

Guo Lin, Bart Geerts, Zhien Wang, Coltin Grasmick, Xiaoqin Jing, and Jing Yang. Interactions between a Nocturnal MCS and the Stable Boundary Layer as Observed by an Airborne Compact Raman Lidar during PECAN. *Monthly Weather Review*, 2019. doi: 10.1175/MWR-D-18-0388.1. URL <https://journals.ametsoc.org/view/journals/mwre/147/9/mwr-d-18-0388.1.xml>. section: Monthly Weather Review.

Guo Lin, Coltin Grasmick, Bart Geerts, Zhien Wang, and Min Deng. Convection Initiation and Bore Formation Following the Collision of Mesoscale Boundaries over a Developing Stable Boundary Layer: A Case Study from PECAN. *Monthly Weather Review*, 2021. doi: 10.1175/MWR-D-20-0282.1. URL <https://journals.ametsoc.org/view/journals/mwre/149/7/MWR-D-20-0282.1.xml>. section: Monthly Weather Review.

Christopher M. Little, Radley M. Horton, Robert E. Kopp, Michael Oppenheimer, Gabriel A. Vecchi, and Gabriele Villarini. Joint projections of US East Coast sea level and storm surge. *Nature Climate Change*, 5(12):1114–1120, 2015. ISSN 1758-6798. doi: 10.1038/nclimate2801.

Bo Liu, Zhien Wang, Yong Cai, Perry Wechsler, William Kuestner, Matthew Burkhart, and Wayne Welch. Compact airborne raman lidar for profiling aerosol, water vapor and clouds. *Optics Express*, 22(17):20613–20621, 2014. ISSN 1094-4087. doi: 10.1364/OE.22.020613. URL <https://www.osapublishing-org.colorado.idm.oclc.org/oe/abstract.cfm?uri=oe-22-17-20613>. Publisher: Optical Society of America.

Jia Liu, Xiaofeng Xu, and Xiangyang Luo. Estimation of Tropical Cyclone Intensity Using Infrared Data from a Geostationary Satellite. *Sola*, 15:189–192, 2019. doi: 10.2151/sola.2019-034.

Jiping Liu, Jeonghye Lee, and Ruide Zhou. Review of big-data and AI application in typhoon-related disaster risk early warning in Typhoon Committee region. *Tropical Cyclone Research and Review*, 12(4):341–353, 2023. ISSN 2225-6032. doi: 10.1016/j.tccr.2023.12.004.

Manuel Lonfat, Frank D. Marks, and Shuyi S. Chen. Precipitation Distribution in Tropical Cyclones Using the Tropical Rainfall Measuring Mission (TRMM) Microwave Imager: A Global Perspective. *Monthly Weather Review*, 132(7):1645–1660, 2004. ISSN 1520-0493, 0027-0644. doi: 10.1175/1520-0493(2004)132<1645:PDITCU>2.0.CO;2.

Sylvie Lorsolo, Jun A. Zhang, Frank Marks, and John Gamache. Estimation and Mapping of Hurricane Turbulent Energy Using Airborne Doppler Measurements. *Monthly Weather Review*, 2010. doi: 10.1175/2010MWR3183.1. URL <https://journals.ametsoc.org/view/journals/mwre/138/9/2010mwr3183.1.xml>.

Sharanya J. Majumdar, Linus Magnusson, Peter Bechtold, Jean Raymond Bidlot, and James D. Doyle. Advanced Tropical Cyclone Prediction Using the Experimental Global ECMWF and Operational Regional COAMPS-TC Systems. *Monthly Weather Review*, jul 26 2023a. doi: 10.1175/MWR-D-22-0236.1. URL <https://journals.ametsoc.org/view/journals/mwre/151/8/MWR-D-22-0236.1.xml>. section: Monthly Weather Review.

Sharanya J. Majumdar, Samantha Nebylitsa, Philip J. Klotzbach, Cameron Masiello, and Zachary R. Michael. North Atlantic Tropical Cyclone Intensification: Regional Drivers and

- Trends. *Geophysical Research Letters*, 50(17):e2023GL104803, 2023b. ISSN 1944-8007. doi: 10.1029/2023GL104803. <https://onlinelibrary.wiley.com/doi/pdf/10.1029/2023GL104803>.
- Joanne S. Malkus. On the structure and maintenance of the mature hurricane eye. *Journal of the Atmospheric Sciences*, 15(4):337–349, 1958. ISSN 1520-0469. doi: 10.1175/1520-0469(1958)015<0337:OTSAMO>2.0.CO;2. URL https://journals.ametsoc.org/view/journals/atsc/15/4/1520-0469_1958_015_0337_otsamo_2_0_co_2.xml. Publisher: American Meteorological Society Section: Journal of the Atmospheric Sciences.
- Timothy Marchok. Important Factors in the Tracking of Tropical Cyclones in Operational Models. *Journal of Applied Meteorology and Climatology*, 2021. doi: 10.1175/JAMC-D-20-0175.1. URL <https://journals.ametsoc.org/view/journals/apme/60/9/JAMC-D-20-0175.1.xml>.
- Frank D. Marks, Peter G. Black, Michael T. Montgomery, and Robert W. Burpee. Structure of the Eye and Eyewall of Hurricane Hugo (1989). *Monthly Weather Review*, 136(4):1237–1259, 2008. ISSN 1520-0493, 0027-0644. doi: 10.1175/2007MWR2073.1.
- Jonathan Martinez, Michael M. Bell, Jonathan L. Vigh, and Robert F. Rogers. Examining Tropical Cyclone Structure and Intensification with the FLIGHT+ Dataset from 1999 to 2012. *Monthly Weather Review*, 145(11):4401–4421, 2017. ISSN 1520-0493, 0027-0644. doi: 10.1175/MWR-D-17-0011.1.
- Corene J. Matyas, Stephanie E. Zick, and Kimberly M. Wood. Comparing Reflectivity from Space-Based and Ground-Based Radars During Detection of Rainbands in Two Tropical Cyclones. *Atmosphere*, 16(3):307, 2025. ISSN 2073-4433. doi: 10.3390/atmos16030307.
- Joshua May, Liang Hu, Elizabeth A. Ritchie, Mehrtash Harandi, and J. Scott Tyo. Automated Segmentation of tropical cyclone clouds in geostationary infrared images. *IEEE Geoscience and Remote Sensing Letters*, pages 1–1, 2024. ISSN 1558-0571. doi: 10.1109/LGRS.2024.3358733.
- George L. Mellor and Tetsuji Yamada. Development of a turbulence closure model for geophysical fluid problems. *Reviews of Geophysics*, 20(4):851–875, 1982. ISSN 1944-9208. doi: 10.1029/RG020i004p00851. eprint: <https://onlinelibrary.wiley.com/doi/pdf/10.1029/RG020i004p00851>.
- Robert Mendelsohn, Kerry Emanuel, Shun Chonabayashi, and Laura Bakkensen. The impact of climate change on global tropical cyclone damage. *Nature Climate Change*, 2(3):205–209, 2012. ISSN 1758-6798. doi: 10.1038/nclimate1357.
- Andrew E. Mercer, Alexandria D. Grimes, and Kimberly M. Wood. Application of Unsupervised Learning Techniques to Identify Atlantic Tropical Cyclone Rapid Intensification Environments. *Journal of Applied Meteorology and Climatology*, 60(1):119–138, 2021. ISSN 1558-8424, 1558-8432. doi: 10.1175/JAMC-D-20-0105.1.
- Jie Ming and Jun A. Zhang. Effects of surface flux parameterization on the numerically simulated intensity and structure of Typhoon Morakot (2009). *Advances in Atmospheric Sciences*, 33(1): 58–72, 2016. ISSN 1861-9533. doi: 10.1007/s00376-015-4202-z.
- Michael T. Montgomery and Randall J. Kallenbach. A theory for vortex rossby-waves and its application to spiral bands and intensity changes in hurricanes. *Quarterly Journal of the Royal Meteorological Society*, 123(538):435–465, 1997. ISSN 1477-870X. doi: 10.1002/qj.49712353810. URL <https://onlinelibrary.wiley.com/doi/10.1002/qj.49712353810>.

Michael T. Montgomery, Jun A. Zhang, and Roger K. Smith. An analysis of the observed low-level structure of rapidly intensifying and mature hurricane Earl (2010). *Quarterly Journal of the Royal Meteorological Society*, 140(684):2132–2146, 2014. ISSN 1477-870X. doi: 10.1002/qj.2283. eprint: <https://onlinelibrary.wiley.com/doi/pdf/10.1002/qj.2283>.

Kimberly J. Mueller, Mark DeMaria, John Knaff, James P. Kossin, and Thomas H. Vonder Haar. Objective Estimation of Tropical Cyclone Wind Structure from Infrared Satellite Data. *Weather and Forecasting*, 2006. doi: 10.1175/WAF955.1. URL https://journals.ametsoc.org/view/journals/wefo/21/6/waf955_1.xml.

Joanne Muller, Kaylee Mooney, Steven G. Bowen, Philip J. Klotzbach, Tynisha Martin, Tom J. Philp, Bhatt Dhruvkumar, Richard S. Dixon, and Senthil B. Girimurugan. Normalized Hurricane Damage in the United States: 1900–2022. *Bulletin of the American Meteorological Society*, 2025. doi: 10.1175/BAMS-D-23-0280.1. URL <https://journals.ametsoc.org/view/journals/bams/106/1/BAMS-D-23-0280.1.xml>.

Ethan Murray and Zhien Wang. Supporting data: Cloud height distributions and the role of vertical mixing in the tropical cyclone eye derived from compact raman lidar observations [dataset], 2024. URL <https://doi.org/10.5281/zenodo.10570351>.

Ethan J. Murray, Jason Dunion, Kristopher B. Karnauskas, Zhien Wang, and Jun A. Zhang. Cloud height distributions and the role of vertical mixing in the tropical cyclone eye derived from compact raman lidar observations. *Geophysical Research Letters*, 51(14):e2024GL108515, 2024. doi: 10.1029/2024GL108515. URL <https://onlinelibrary.wiley.com/doi/abs/10.1029/2024GL108515>.

Ethan J. Murray, Kristopher B. Karnauskas, Zhien Wang, and Jun A. Zhang. Novel observations of convective-scale cloud and precipitation distributions in the tropical cyclone rainbands. *In Preparation*, 2025a.

Ethan J. Murray, Jon Moskaitis, James Doyle, Kristopher B. Karnauskas, Zhien Wang, and Jun A. Zhang. An observation-model intercomparison framework for diagnosing tropical cyclone thermodynamic change: Application to hurricane sam (2021). *Monthly Weather Review*, in revision, 2025b.

Hal F. Needham, Barry D. Keim, and David Sathiari. A review of tropical cyclone-generated storm surges: Global data sources, observations, and impacts. *Reviews of Geophysics*, 53(2): 545–591, 2015. ISSN 1944-9208. doi: 10.1002/2014RG000477. URL <https://onlinelibrary.wiley.com/doi/pdf/10.1002/2014RG000477>.

Leon T. Nguyen, Robert Rogers, Jonathan Zawislak, and Jun A. Zhang. Assessing the Influence of Convective Downdrafts and Surface Enthalpy Fluxes on Tropical Cyclone Intensity Change in Moderate Vertical Wind Shear. *Monthly Weather Review*, 147(10):3519–3534, 2019. ISSN 1520-0493, 0027-0644. doi: 10.1175/MWR-D-18-0461.1.

David S. Nolan, Daniel P. Stern, and Jun A. Zhang. Evaluation of Planetary Boundary Layer Parameterizations in Tropical Cyclones by Comparison of In Situ Observations and High-Resolution Simulations of Hurricane Isabel (2003). Part II: Inner-Core Boundary Layer and Eyewall Structure. *Monthly Weather Review*, 2009a. doi: 10.1175/2009MWR2786.1. URL <https://journals.ametsoc.org/view/journals/mwre/137/11/2009mwr2786.1.xml>.

David S. Nolan, Jun A. Zhang, and Daniel P. Stern. Evaluation of Planetary Boundary Layer Parameterizations in Tropical Cyclones by Comparison of In Situ Observations and High-Resolution Simulations of Hurricane Isabel (2003). Part I: Initialization, Maximum Winds, and the Outer-Core Boundary Layer. *Monthly Weather Review*, 137(11):3651–3674, 2009b. ISSN 1520-0493, 0027-0644. doi: 10.1175/2009MWR2785.1. publisher: American Meteorological Society section: Monthly Weather Review.

Christopher J. Nowotarski, Justin Spotts, Roger Edwards, Scott Overpeck, and Gary R. Woodall. Tornadoes in Hurricane Harvey. *Weather and Forecasting*, 2021. doi: 10.1175/WAF-D-20-0196.1. URL <https://journals.ametsoc.org/view/journals/wefo/36/5/WAF-D-20-0196.1.xml>. section: Weather and Forecasting.

Chibueze N. Oguejiofor, George H. Bryan, Richard Rotunno, Peter P. Sullivan, and David H. Richter. The Role of Turbulence in an Intense Tropical Cyclone: Momentum Diffusion, Eddy Viscosities, and Mixing Lengths. *Journal of the Atmospheric Sciences*, 2024. doi: 10.1175/JAS-D-23-0209.1. URL <https://journals.ametsoc.org/view/journals/atsc/81/8/JAS-D-23-0209.1.xml>. section: Journal of the Atmospheric Sciences.

Richard Pasch and David Roberts. Tropical Cyclone Report: Hurricane Sam (AL182021). National Hurricane Center Special Report, mar 18 2022.

John Persing and Michael T. Montgomery. Hurricane Superintensity. *Journal of the Atmospheric Sciences*, 60(19):2349–2371, 2003. ISSN 0022-4928, 1520-0469. doi: 10.1175/1520-0469(2003)060<2349:HS>2.0.CO;2.

Roger A. Pielke and Christopher W. Landsea. Normalized Hurricane Damages in the United States: 1925–95. *Weather and Forecasting*, 13(3):621–631, 1998. ISSN 1520-0434, 0882-8156. doi: 10.1175/1520-0434(1998)013<0621:NHDITU>2.0.CO;2.

Miguel F. Pineros, Elizabeth A. Ritchie, and J. Scott Tyo. Objective Measures of Tropical Cyclone Structure and Intensity Change From Remotely Sensed Infrared Image Data. *IEEE Transactions on Geoscience and Remote Sensing*, 46(11):3574–3580, 2008. ISSN 1558-0644. doi: 10.1109/TGRS.2008.2000819.

Melissa A. Piper and Ryan D. Torn. Comparison of 2018–2022 Tropical Cyclone Track Forecasts Before and After NOAA G-IV Missions. *Weather and Forecasting*, 2025. doi: 10.1175/WAF-D-24-0114.1. URL <https://journals.ametsoc.org/view/journals/wefo/aop/WAF-D-24-0114.1/WAF-D-24-0114.1.xml>.

Mark D. Powell. Boundary Layer Structure and Dynamics in Outer Hurricane Rainbands. Part II: Downdraft Modification and Mixed Layer Recovery. *Monthly Weather Review*, 118(4):918–938, 1990. ISSN 1520-0493, 0027-0644. doi: 10.1175/1520-0493(1990)118<0918:BLSADI>2.0.CO;2.

Edward N. Rappaport. Fatalities in the United States from Atlantic Tropical Cyclones: New Data and Interpretation. *Bulletin of the American Meteorological Society*, 2014. doi: 10.1175/BAMS-D-12-00074.1. URL <https://journals.ametsoc.org/view/journals/bams/95/3/bams-d-12-00074.1.xml>.

Paul D. Reasor, Michael T. Montgomery, Frank D. Marks, and John F. Gamache. Low-Wavenumber Structure and Evolution of the Hurricane Inner Core Observed by Airborne Dual-Doppler Radar.

Monthly Weather Review, 2000. ISSN 1520-0493. URL https://journals.ametsoc.org/view/journals/mwre/128/6/1520-0493_2000_128_1653_lwsaeo_2.0.co_2.xml. section: Monthly Weather Review.

Paul D. Reasor, Matthew D. Eastin, and John F. Gamache. Rapidly Intensifying Hurricane Guillermo (1997). Part I: Low-Wavenumber Structure and Evolution. Monthly Weather Review, 2009. doi: 10.1175/2008MWR2487.1. URL <https://journals.ametsoc.org/view/journals/mwre/137/2/2008mwr2487.1.xml>. section: Monthly Weather Review.

Paul D. Reasor, Robert Rogers, and Sylvie Lorsolo. Environmental Flow Impacts on Tropical Cyclone Structure Diagnosed from Airborne Doppler Radar Composites. Monthly Weather Review, 141(9):2949–2969, sep 1 2013. ISSN 1520-0493, 0027-0644. doi: 10.1175/MWR-D-12-00334.1. publisher: American Meteorological Society section: Monthly Weather Review.

Lucrezia Ricciardulli, Brian Howell, Christopher R. Jackson, Jeff Hawkins, Joe Courtney, Ad Stofelen, Sebastian Langlade, Chris Fogarty, Alexis Mouche, William Blackwell, Thomas Meissner, Julian Heming, Brett Candy, Tony McNally, Masahiro Kazumori, Chinmay Khadke, and Maria Ana Glaiza Escullar. Remote sensing and analysis of tropical cyclones: Current and emerging satellite sensors. Tropical Cyclone Research and Review, 12(4):267–293, 2023. ISSN 2225-6032. doi: 10.1016/j.tcrr.2023.12.003.

David H. Richter, Rachel Bohac, and Daniel P. Stern. An Assessment of the Flux Profile Method for Determining Air–Sea Momentum and Enthalpy Fluxes from Dropsonde Data in Tropical Cyclones. Journal of the Atmospheric Sciences, 2016. doi: 10.1175/JAS-D-15-0331.1. URL <https://journals.ametsoc.org/view/journals/atsc/73/7/jas-d-15-0331.1.xml>.

Rosimar Rios-Berrios and Ryan D. Torn. Climatological Analysis of Tropical Cyclone Intensity Changes under Moderate Vertical Wind Shear. Monthly Weather Review, may 1 2017. doi: 10.1175/MWR-D-16-0350.1. URL <https://journals.ametsoc.org/view/journals/mwre/145/5/mwr-d-16-0350.1.xml>. section: Monthly Weather Review.

Rosimar Rios-Berrios, Peter M. Finocchio, Joshua J. Alland, Xiaomin Chen, Michael S. Fischer, Stephanie N. Stevenson, and Dandan Tao. A Review of the Interactions between Tropical Cyclones and Environmental Vertical Wind Shear. Journal of the Atmospheric Sciences, 81(4): 713–741, 2024. ISSN 0022-4928, 1520-0469. doi: 10.1175/JAS-D-23-0022.1.

Robert Rogers and Jun A Zhang. Airborne Doppler Radar Observations of Tropical Cyclone Boundary Layer Kinematic Structure and Evolution During Landfall. Geophysical Research Letters, 50(23), 2023. doi: 10.1029/2023GL105548.

Robert Rogers, Shuyi Chen, Joseph Tenerelli, and Hugh Willoughby. A Numerical Study of the Impact of Vertical Shear on the Distribution of Rainfall in Hurricane Bonnie (1998). Monthly Weather Review, 2003. doi: 10.1175//2546.1. URL https://journals.ametsoc.org/view/journals/mwre/131/8/_2546.1.xml.

Robert Rogers, Sylvie Lorsolo, Paul Reasor, John Gamache, and Frank Marks. Multiscale Analysis of Tropical Cyclone Kinematic Structure from Airborne Doppler Radar Composites. Monthly Weather Review, 140(1):77–99, 2012. ISSN 1520-0493, 0027-0644. doi: 10.1175/MWR-D-10-05075.1.

Robert Rogers, Sim Aberson, Altug Aksoy, Bachir Annane, Michael Black, Joseph Cione, Neal Dorst, Jason Dunion, John Gamache, Stan Goldenberg, Sundararaman Gopalakrishnan, John Kaplan, Bradley Klotz, Sylvie Lorsolo, Frank Marks, Shirley Murillo, Mark Powell, Paul Reasor, Kathryn Sellwood, Eric Uhlhorn, Tomislava Vukicevic, Jun Zhang, and Xuejin Zhang. Noaa'S Hurricane Intensity Forecasting Experiment: A Progress Report. *Bulletin of the American Meteorological Society*, 2013a. doi: 10.1175/BAMS-D-12-00089.1. URL <https://journals.ametsoc.org/view/journals/bams/94/6/bams-d-12-00089.1.xml>.

Robert Rogers, Paul Reasor, and Sylvie Lorsolo. Airborne doppler observations of the inner-core structural differences between intensifying and steady-state tropical cyclones. *Monthly Weather Review*, 141(9):2970–2991, 2013b. ISSN 1520-0493, 0027-0644. doi: 10.1175/MWR-D-12-00357.1. URL <https://journals.ametsoc.org/view/journals/mwre/141/9/mwr-d-12-00357.1.xml>. Publisher: American Meteorological Society Section: Monthly Weather Review.

Robert F. Rogers. Recent Advances in Our Understanding of Tropical Cyclone Intensity Change Processes from Airborne Observations. *Atmosphere*, 12(5):650, 2021. ISSN 2073-4433. doi: 10.3390/atmos12050650.

Robert F. Rogers, Michael L. Black, Shuyi S. Chen, and Robert A. Black. An Evaluation of Microphysics Fields from Mesoscale Model Simulations of Tropical Cyclones. Part I: Comparisons with Observations. *Journal of the Atmospheric Sciences*, 64(6):1811–1834, 2007. ISSN 0022-4928, 1520-0469. doi: 10.1175/JAS3932.1. publisher: American Meteorological Society section: Journal of the Atmospheric Sciences.

Robert F. Rogers, Paul D. Reasor, and Jun A. Zhang. Multiscale Structure and Evolution of Hurricane Earl (2010) during Rapid Intensification. *Monthly Weather Review*, 143(2):536–562, 2015. ISSN 1520-0493, 0027-0644. doi: 10.1175/MWR-D-14-00175.1.

Robert F. Rogers, Paul D. Reasor, Jonathan A. Zawislak, and Leon T. Nguyen. Precipitation Processes and Vortex Alignment during the Intensification of a Weak Tropical Cyclone in Moderate Vertical Shear. *Monthly Weather Review*, 148(5):1899–1929, 2020. ISSN 1520-0493, 0027-0644. doi: 10.1175/MWR-D-19-0315.1. publisher: American Meteorological Society section: Monthly Weather Review.

Kelly Ryan, Lisa Bucci, Javier Delgado, Robert Atlas, and Shirley Murillo. Impact of Gulfstream-IV Dropsondes on Tropical Cyclone Prediction in a Regional OSSE System. *Monthly Weather Review*, 2019. doi: 10.1175/MWR-D-18-0157.1. URL <https://journals.ametsoc.org/view/journals/mwre/147/8/mwr-d-18-0157.1.xml>.

Christopher E. Samsury and Edward J. Zipser. Secondary Wind Maxima in Hurricanes: Airflow and Relationship to Rainbands. *Monthly Weather Review*, 123(12):3502–3517, 1995. ISSN 1520-0493, 0027-0644. doi: 10.1175/1520-0493(1995)123<3502:SWMIA>2.0.CO;2. publisher: American Meteorological Society section: Monthly Weather Review.

Benjamin A. Schenkel, Kristin M. Calhoun, Thea N. Sandmæl, Zachary R. Fruits, Isaiah Schick, Marcus C. Ake, and Benjamin F. Kassel. Lightning and Radar Characteristics of Tornadic Cells in Landfalling Tropical Cyclones. *Journal of Geophysical Research: Atmospheres*, 128(16):e2023JD038685, 2023. ISSN 2169-8996. doi: 10.1029/2023JD038685. eprint: <https://onlinelibrary.wiley.com/doi/pdf/10.1029/2023JD038685>.

Wayne H. Schubert, Michael T. Montgomery, Richard K. Taft, Thomas A. Guinn, Scott R. Fulton, James P. Kossin, and James P. Edwards. Polygonal eyewalls, asymmetric eye contraction, and potential vorticity mixing in hurricanes. *Journal of the Atmospheric Sciences*, 56(9):1197–1223, 1999. ISSN 0022-4928, 1520-0469. doi: 10.1175/1520-0469(1999)056<1197:PEAECA>2.0.CO;2. URL https://journals.ametsoc.org/view/journals/atsc/56/9/1520-0469_1999_056_1197_peaeca_2.0.co_2.xml. Publisher: American Meteorological Society Section: Journal of the Atmospheric Sciences.

Wayne H. Schubert, Christopher M. Rozoff, Jonathan L. Vigh, Brian D. McNoldy, and James P. Kossin. On the distribution of subsidence in the hurricane eye. *Quarterly Journal of the Royal Meteorological Society*, 133(624):595–605, 2007a. ISSN 1477-870X. doi: 10.1002/qj.49. URL <https://onlinelibrary.wiley.com/doi/abs/10.1002/qj.49>. eprint: <https://onlinelibrary.wiley.com/doi/pdf/10.1002/qj.49>.

Wayne H. Schubert, Christopher M. Rozoff, Jonathan L. Vigh, Brian D. McNoldy, and James P. Kossin. On the distribution of subsidence in the hurricane eye. *Quarterly Journal of the Royal Meteorological Society*, 133(624):595–605, 2007b. ISSN 1477-870X. doi: 10.1002/qj.49. URL <https://onlinelibrary.wiley.com/doi/abs/10.1002/qj.49>.

Kathryn J. Sellwood, Jason A. Sippel, and Altug Aksoy. Assimilation of Coyote Small Unmanned Aircraft System Observations in Hurricane Maria (2017) Using Operational HWRF. *Weather and Forecasting*, 2023. doi: 10.1175/WAF-D-22-0214.1. URL <https://journals.ametsoc.org/view/journals/wefo/38/6/WAF-D-22-0214.1.xml>.

Udai Shimada, Paul D. Reasor, Robert F. Rogers, Michael S. Fischer, Frank D. Marks, Jonathan A. Zawislak, and Jun A. Zhang. Shear-Relative Asymmetric Kinematic Characteristics of Intensifying Hurricanes as Observed by Airborne Doppler Radar. *Monthly Weather Review*, 152(2):491–512, 2024. ISSN 1520-0493, 0027-0644. doi: 10.1175/MWR-D-22-0340.1.

R. H. Simpson. Exploring eye of typhoon “marge,” 1951. *Bulletin of the American Meteorological Society*, 33(7):286–298, 1952. ISSN 0003-0007, 1520-0477. doi: 10.1175/1520-0477-33-7-286. URL https://journals.ametsoc.org/view/journals/bams/33/7/1520-0477-33_7_286.xml. Publisher: American Meteorological Society Section: Bulletin of the American Meteorological Society.

R. H. Simpson and L. G. Starrett. Further Studies of Hurricane Structure by Aircraft Reconnaissance. *Bulletin of the American Meteorological Society*, 36(9):459–468, 1955. ISSN 0003-0007.

Jason A. Sippel, Xingren Wu, Sarah D. Ditcheck, Vijay Tallapragada, and Daryl T. Kleist. Impacts of Assimilating Additional Reconnaissance Data on Operational GFS Tropical Cyclone Forecasts. *Weather and Forecasting*, 37(9):1615–1639, 2022. ISSN 1520-0434, 0882-8156. doi: 10.1175/WAF-D-22-0058.1.

Jason A. Sippel, Sarah D. Ditcheck, Kelly Ryan, and Christopher W. Landsea. The G-IV Inner Circumnavigation: A Story of Successful Organic Interactions Between Research and Operations at NOAA. *Bulletin of the American Meteorological Society*, 2024. doi: 10.1175/BAMS-D-23-0084.1. URL <https://journals.ametsoc.org/view/journals/bams/105/1/BAMS-D-23-0084.1.xml>.

Matthew Sitkowski, James P. Kossin, and Christopher M. Rozoff. Intensity and Structure Changes during Hurricane Eyewall Replacement Cycles. *Monthly Weather Review*, 139(12):3829–3847, 2011. ISSN 1520-0493, 0027-0644. doi: 10.1175/MWR-D-11-00034.1.

William C Skamarock, Joseph B Klemp, Jimy Dudhia, David O Gill, Zhiqian Liu, Judith Berner, Wei Wang, Jordan G Powers, Michael G Duda, Dale M Barker, and Xiang-Yu Huang. A Description of the Advanced Research WRF Model Version 4. *NCAR Tech. Note*, 556 + STR, 2019.

Roger K. Smith, Jun A. Zhang, and Michael T. Montgomery. The dynamics of intensification in a hurricane weather research and forecasting simulation of hurricane earl (2010). *Quarterly Journal of the Royal Meteorological Society*, 143(702):293–308, 2017. ISSN 1477-870X. doi: 10.1002/qj.2922. URL <https://onlinelibrary.wiley.com/doi/abs/10.1002/qj.2922>. eprint: <https://onlinelibrary.wiley.com/doi/pdf/10.1002/qj.2922>.

Matthias Steiner, Robert A. Houze, and Sandra E. Yuter. Climatological Characterization of Three-Dimensional Storm Structure from Operational Radar and Rain Gauge Data. *Journal of Applied Meteorology and Climatology*, 34(9):1978–2007, sep 1 1995. ISSN 1520-0450, 0894-8763. doi: 10.1175/1520-0450(1995)034<1978:CCOTDS>2.0.CO;2. publisher: American Meteorological Society section: Journal of Applied Meteorology and Climatology.

Daniel P. Stern and George H. Bryan. Using Simulated Dropsondes to Understand Extreme Updrafts and Wind Speeds in Tropical Cyclones. *Monthly Weather Review*, 146(11):3901–3925, 2018. ISSN 1520-0493, 0027-0644. doi: 10.1175/MWR-D-18-0041.1.

Roland B. Stull. *Mean Boundary Layer Characteristics*, pages 1–27. Springer Netherlands, Dordrecht, 1988. ISBN 978-90-277-2769-5. URL http://link.springer.com/10.1007/978-94-009-3027-8_1. DOI: 10.1007/978-94-009-3027-8_1.

Hui Su, Longtao Wu, Jonathan H. Jiang, Raksha Pai, Alex Liu, Albert J. Zhai, Peyman Tavallali, and Mark DeMaria. Applying Satellite Observations of Tropical Cyclone Internal Structures to Rapid Intensification Forecast With Machine Learning. *Geophysical Research Letters*, 47(17):e2020GL089102, 2020. ISSN 1944-8007. doi: 10.1029/2020GL089102. URL <https://onlinelibrary.wiley.com/doi/pdf/10.1029/2020GL089102>.

Takuya Takahashi, David S. Nolan, and Brian D. McNoldy. The vortex structure and near-surface winds of Typhoon Faxai (2019) during landfall. Part II: Evaluation of WRF simulations. *Quarterly Journal of the Royal Meteorological Society*, 150(760):1643–1667, 2024. ISSN 1477-870X. doi: 10.1002/qj.4663. eprint: <https://onlinelibrary.wiley.com/doi/10.1002/qj.4663>.

Brian Tang and Kerry Emanuel. Midlevel Ventilation’s Constraint on Tropical Cyclone Intensity. *Journal of the Atmospheric Sciences*, 67(6):1817–1830, 2010. ISSN 0022-4928, 1520-0469. doi: 10.1175/2010JAS3318.1. publisher: American Meteorological Society section: Journal of the Atmospheric Sciences.

Brian H. Tang, Rosimar Rios-Berrios, and Jun A. Zhang. Diagnosing Radial Ventilation in Dropsonde Observations of Hurricane Sam (2021). *Monthly Weather Review*, -1:203–225, 2024. ISSN 1520-0493, 0027-0644. doi: 10.1175/MWR-D-23-0224.1. URL <https://journals.ametsoc.org/view/journals/mwre/aop/MWR-D-23-0224.1/MWR-D-23-0224.1.xml>.

Xiaowen Tang, Wen-Chau Lee, and Michael Bell. A Squall-Line-Like Principal Rainband in Typhoon Hagupit (2008) Observed by Airborne Doppler Radar. *Journal of the Atmospheric Sciences*, 71(7):2733–2746, 2014. ISSN 0022-4928, 1520-0469. doi: 10.1175/JAS-D-13-0307.1. publisher: American Meteorological Society section: Journal of the Atmospheric Sciences.

Xiaowen Tang, Wen-Chau Lee, and Michael Bell. Subrainband Structure and Dynamic Characteristics in the Principal Rainband of Typhoon Hagupit (2008). *Monthly Weather Review*, 146(1): 157–173, 2018. ISSN 1520-0493, 0027-0644. doi: 10.1175/MWR-D-17-0178.1.

Cheng Tao and Haiyan Jiang. Distributions of Shallow to Very Deep Precipitation-Convection in Rapidly Intensifying Tropical Cyclones. *Journal of Climate*, 2015. doi: 10.1175/JCLI-D-14-00448.1. URL <https://journals.ametsoc.org/view/journals/clim/28/22/jcli-d-14-00448.1.xml>. section: Journal of Climate.

Cheng Tao, Haiyan Jiang, and Jonathan Zawislak. The Relative Importance of Stratiform and Convective Rainfall in Rapidly Intensifying Tropical Cyclones. *Monthly Weather Review*, 145 (3):795–809, 2017. ISSN 1520-0493, 0027-0644. doi: 10.1175/MWR-D-16-0316.1.

M. Tiedtke. A Comprehensive Mass Flux Scheme for Cumulus Parameterization in Large-Scale Models. *Monthly Weather Review*, 1989. ISSN 1520-0493. URL https://journals.ametsoc.org/view/journals/mwre/117/8/1520-0493_1989_117_1779_acmfsf_2_0_co_2.xml.

Mingfang Ting, James P. Kossin, Suzana J. Camargo, and Cuihua Li. Past and Future Hurricane Intensity Change along the U.S. East Coast. *Scientific Reports*, 9(1):7795, 2019. ISSN 2045-2322. doi: 10.1038/s41598-019-44252-w.

Biao Tong, Jiyang Fu, Yaxue Deng, Yongjun Huang, Pakwai Chan, and Yuncheng He. Estimation of Tropical Cyclone Intensity via Deep Learning Techniques from Satellite Cloud Images. *Remote Sensing*, 15(17):4188, 2023. ISSN 2072-4292. doi: 10.3390/rs15174188.

Gina Tonn and Jeffrey Czajkowski. Us tropical cyclone flood risk: Storm surge versus freshwater. *Risk Analysis*, 42(12):2748–2764, 2022. ISSN 1539-6924. doi: 10.1111/risa.13890. URL <https://onlinelibrary.wiley.com/doi/pdf/10.1111/risa.13890>.

William Stanley Torgerson, Juliane Schwendike, Andrew Ross, and Chris Short. Comparing short term intensity fluctuations and an Eyewall replacement cycle in Hurricane Irma (2017) during a period of rapid intensification. preprint, Dynamical processes in the tropics, incl. tropical-extratropical interactions, 2023. URL <https://egusphere.copernicus.org/preprints/2023/egusphere-2023-1272/>. DOI: 10.5194/egusphere-2023-1272.

Jonathan L. Vigh and Wayne H. Schubert. Rapid Development of the Tropical Cyclone Warm Core. *Journal of the Atmospheric Sciences*, 66(11):3335–3350, 2009. ISSN 0022-4928, 1520-0469. doi: 10.1175/2009JAS3092.1.

Jonathan L. Vigh, John A. Knaff, and Wayne H. Schubert. A Climatology of Hurricane Eye Formation. *Monthly Weather Review*, 140(5):1405–1426, 2012. ISSN 1520-0493, 0027-0644. doi: 10.1175/MWR-D-11-00108.1.

Joshua B. Wadler, Robert F. Rogers, and Paul D. Reasor. The Relationship between Spatial Variations in the Structure of Convective Bursts and Tropical Cyclone Intensification as Determined by Airborne Doppler Radar. *Monthly Weather Review*, 146(3):761–780, 2018a. ISSN 1520-0493, 0027-0644. doi: 10.1175/MWR-D-17-0213.1.

Joshua B. Wadler, Jun A. Zhang, Benjamin Jaimes, and Lynn K. Shay. Downdrafts and the Evolution of Boundary Layer Thermodynamics in Hurricane Earl (2010) before and during Rapid Intensification. *Monthly Weather Review*, 146(11):3545–3565, 2018b. ISSN 1520-0493, 0027-0644.

doi: 10.1175/MWR-D-18-0090.1. publisher: American Meteorological Society section: Monthly Weather Review.

Joshua B. Wadler, David S. Nolan, Jun A. Zhang, and Lynn K. Shay. Thermodynamic Characteristics of Downdrafts in Tropical Cyclones as Seen in Idealized Simulations of Different Intensities. *Journal of the Atmospheric Sciences*, 78(11):3503–3524, 2021. ISSN 0022-4928, 1520-0469. doi: 10.1175/JAS-D-21-0006.1. publisher: American Meteorological Society section: Journal of the Atmospheric Sciences.

Joshua B. Wadler, Joseph J. Cione, Jun A. Zhang, Evan A. Kalina, and John Kaplan. The Effects of Environmental Wind Shear Direction on Tropical Cyclone Boundary Layer Thermodynamics and Intensity Change from Multiple Observational Datasets. *Monthly Weather Review*, 150(1): 115–134, 2022. ISSN 1520-0493, 0027-0644. doi: 10.1175/MWR-D-21-0022.1.

Joshua B. Wadler, Joseph J. Cione, Robert F. Rogers, and Michael S. Fischer. On the Distribution of Convective and Stratiform Precipitation in Tropical Cyclones from Airborne Doppler Radar and Its Relationship to Intensity Change and Environmental Wind Shear Direction. *Monthly Weather Review*, 151(12):3209–3233, 2023a. ISSN 1520-0493, 0027-0644. doi: 10.1175/MWR-D-23-0048.1. publisher: American Meteorological Society section: Monthly Weather Review.

Joshua B. Wadler, Johna E. Rudzin, Benjamin Jaimes de la Cruz, Jie Chen, Michael Fischer, Guanghua Chen, Nannan Qin, Brian Tang, and Qingqing Li. A review of recent research progress on the effect of external influences on tropical cyclone intensity change. *Tropical Cyclone Research and Review*, 12(3):200–215, 2023b. ISSN 2225-6032. doi: 10.1016/j.tctr.2023.09.001.

Joshua B. Wadler, Lauren Villafane, Joseph J. Cione, Kevin Adkins, and George R. Alvey. What was the Bumpiest Flight Ever on NOAA’s WP-3d Hurricane Hunter Aircraft? *Bulletin of the American Meteorological Society*, mar 28 2025. doi: 10.1175/BAMS-D-24-0065.1. URL <https://journals.ametsoc.org/view/journals/bams/aop/BAMS-D-24-0065.1/BAMS-D-24-0065.1.xml>. section: Bulletin of the American Meteorological Society.

Thomas Wahl, Shaleen Jain, Jens Bender, Steven D. Meyers, and Mark E. Luther. Increasing risk of compound flooding from storm surge and rainfall for major US cities. *Nature Climate Change*, 5(12):1093–1097, 2015. ISSN 1758-6798. doi: 10.1038/nclimate2736.

Roger M. Wakimoto and Peter G. Black. Damage Survey of Hurricane Andrew and Its Relationship to the Eyewall. *Bulletin of the American Meteorological Society*, 1994. ISSN 1520-0477. URL https://journals.ametsoc.org/view/journals/bams/75/2/1520-0477_1994_075_0189_dsohaa_2_0_co_2.xml.

Le-Yi Wang and Zhe-Min Tan. Deep learning parameterization of the tropical cyclone boundary layer. *Journal of Advances in Modeling Earth Systems*, 15, 2023. doi: 10.1029/2022MS003034. URL <https://onlinelibrary.wiley.com/doi/abs/10.1029/2022MS003034>.

Weiguo Wang, Jongil Han, Fanglin Yang, John Steffen, Bin Liu, Zhan Zhang, Avichal Mehra, and Vijay Tallapragada. Improving the intensity forecast of Tropical Cyclones in Hurricane Analysis and Forecast System. *Weather and Forecasting*, -1, 2023a. ISSN 1520-0434, 0882-8156. doi: 10.1175/WAF-D-23-0041.1. URL <https://journals.ametsoc.org/view/journals/wefo/aop/WAF-D-23-0041.1/WAF-D-23-0041.1.xml>.

Weiguo Wang, Zhan Zhang, John P. Cangialosi, Michael Brennan, Levi Cowan, Peter Clegg, Takuya Hosomi, Ikegami Masaaki, Ananda Kumar Das, Mrutyunjay Mohapatra, Monica Sharma, John Knaff, John Kaplan, Thomas Birchard, James Doyle, Julian Heming, Jon Moskaitis, Will Komaromi, Suhong Ma, Charles Sampson, Liguang Wu, and Eric Blake. A review of recent advances (2018–2021) on tropical cyclone intensity change from operational perspectives, Part 2: Forecasts by Operational Centers. *Tropical Cyclone Research and Review*, 2023b. ISSN 2225-6032. doi: 10.1016/j.tcrr.2023.05.003. URL <https://www.sciencedirect.com/science/article/pii/S2225603223000140>. [Online; accessed 2023-05-14].

Weiguo Wang, Jongil Han, Junghoon Shin, Xiaomin Chen, Andrew Hazelton, Lin Zhu, Hyun-Sook Kim, Xu Li, Bin Liu, Qingfu Liu, John Steffen, Ruiyu Sun, Weizhong Zheng, Zhan Zhang, and Fanglin Yang. Physics schemes in the first version of NCEP operational hurricane analysis and forecast system (HAFS). *Frontiers in Earth Science*, 12, 2024. ISSN 2296-6463. doi: 10.3389/feart.2024.1379069. URL <https://www.frontiersin.org/journals/earth-science/articles/10.3389/feart.2024.1379069/full>.

Xiang Wang and Haiyan Jiang. A 13-Year Global Climatology of Tropical Cyclone Warm-Core Structures from AIRS Data. *Monthly Weather Review*, 147(3):773–790, 2019. ISSN 0027-0644, 1520-0493. doi: 10.1175/MWR-D-18-0276.1.

Ying Wang and Zhaoxia Pu. Assimilation of Radial Velocity from Coastal NEXRAD into HWRF for Improved Forecasts of Landfalling Hurricanes. *Weather and Forecasting*, 2021. doi: 10.1175/WAF-D-20-0163.1. URL <https://journals.ametsoc.org/view/journals/wefo/36/2/WAF-D-20-0163.1.xml>.

Yuqing Wang and Junyao Heng. Contribution of eye excess energy to the intensification rate of tropical cyclones: A numerical study. *Journal of Advances in Modeling Earth Systems*, 8(4):1953–1968, 2016. ISSN 1942-2466. doi: 10.1002/2016MS000709. URL <https://onlinelibrary.wiley.com/doi/pdf/10.1002/2016MS000709>.

Zhen Wang, Jun Zhao, Hong Huang, and Xuezhong Wang. A Review on the Application of Machine Learning Methods in Tropical Cyclone Forecasting. *Frontiers in Earth Science*, 10, 2022. ISSN 2296-6463. doi: 10.3389/feart.2022.902596. URL <https://www.frontiersin.org/journals/earth-science/articles/10.3389/feart.2022.902596/full>.

Zhien Wang and Kenneth Sassen. Cloud type and macrophysical property retrieval using multiple remote sensors. *Journal of Applied Meteorology and Climatology*, 40(10):1665–1682, 2001. ISSN 1520-0450, 0894-8763. doi: 10.1175/1520-0450(2001)040<1665:CTAMPR>2.0.CO;2. URL https://journals.ametsoc.org/view/journals/apme/40/10/1520-0450_2001_040_1665_ctampr_2.0.co_2.xml.

Zhuo Wang. Role of Cumulus Congestus in Tropical Cyclone Formation in a High-Resolution Numerical Model Simulation. *Journal of the Atmospheric Sciences*, may 1 2014. doi: 10.1175/JAS-D-13-0257.1. URL <https://journals.ametsoc.org/view/journals/atsc/71/5/jas-d-13-0257.1.xml>. section: Journal of the Atmospheric Sciences.

Yonghui Weng and Fuqing Zhang. Advances in Convection-Permitting Tropical Cyclone Analysis and Prediction through EnKF Assimilation of Reconnaissance Aircraft Observations. *Journal of the Meteorological Society of Japan. Ser. II*, 94(4):345–358, 2016. doi: 10.2151/jmsj.2016-018.

- H. E. Willoughby. Tropical Cyclone Eye Thermodynamics. *Monthly Weather Review*, 126(12):3053–3067, 1998. ISSN 1520-0493, 0027-0644. doi: 10.1175/1520-0493(1998)126<3053:TCET>2.0.CO;2.
- Hugh E. Willoughby and Marcy B. Chelmow. Objective Determination of Hurricane Tracks from Aircraft Observations. *Monthly Weather Review*, 110(9):1298–1305, 1982. ISSN 1520-0493, 0027-0644. doi: 10.1175/1520-0493(1982)110<1298:ODOHTF>2.0.CO;2. publisher: American Meteorological Society section: Monthly Weather Review.
- Hugh E. Willoughby, Frank D. Marks, and Robert J. Feinberg. Stationary and Moving Convective Bands in Hurricanes. *Journal of the Atmospheric Sciences*, 41(22):3189–3211, 1984. ISSN 0022-4928, 1520-0469. doi: 10.1175/1520-0469(1984)041<3189:SAMCBI>2.0.CO;2.
- Matthew T. Wingo and Daniel J. Cecil. Effects of Vertical Wind Shear on Tropical Cyclone Precipitation. *Monthly Weather Review*, 2010. doi: 10.1175/2009MWR2921.1. URL <https://journals.ametsoc.org/view/journals/mwre/138/3/2009mwr2921.1.xml>.
- Rochelle P. Worsnop, Julie K. Lundquist, George H. Bryan, Rick Damiani, and Walt Muisal. Gusts and shear within hurricane eyewalls can exceed offshore wind turbine design standards. *Geophysical Research Letters*, 44(12):6413–6420, 2017. ISSN 1944-8007. doi: 10.1002/2017GL073537. URL <https://onlinelibrary.wiley.com/doi/10.1002/2017GL073537>.
- Decheng Wu, Zhien Wang, Perry Wechsler, Nick Mahon, Min Deng, Brent Glover, Matthew Burkhardt, William Kuestner, and Ben Heesen. Airborne compact rotational raman lidar for temperature measurement. *Optics Express*, 24(18):A1210–A1223, 2016. ISSN 1094-4087. doi: 10.1364/OE.24.0A1210. URL <https://www.osapublishing-org.colorado.idm.oclc.org/oe/abstract.cfm?uri=oe-24-18-A1210>. Publisher: Optical Society of America.
- Katharine E. D. Wunsch and Anthony C. Didlake. Analyzing Tropical Cyclone Structures during Secondary Eyewall Formation Using Aircraft In Situ Observations. *Monthly Weather Review*, dec 1 2018. doi: 10.1175/MWR-D-18-0197.1. URL <https://journals.ametsoc.org/view/journals/mwre/146/12/mwr-d-18-0197.1.xml>. section: Monthly Weather Review.
- Joshua Wurman and Karen Kosiba. The Role of Small-Scale Vortices in Enhancing Surface Winds and Damage in Hurricane Harvey (2017). *Monthly Weather Review*, 2018. doi: 10.1175/MWR-D-17-0327.1. URL <https://journals.ametsoc.org/view/journals/mwre/146/3/mwr-d-17-0327.1.xml>.
- Dongmei Xu, Jiajun Chen, Hong Li, Feifei Shen, and Zhixin He. The impact of radar radial velocity data assimilation using variational and EnKF systems on the forecast of Super Typhoon Hato (2017) with Rapid Intensification. *Atmospheric Research*, page 107748, 2024. ISSN 0169-8095. doi: 10.1016/j.atmosres.2024.107748.
- Hongxiong Xu and Yuqing Wang. Sensitivity of fine-scale structure in tropical cyclone boundary layer to model horizontal resolution at sub-kilometer grid spacing. *Frontiers in Earth Science*, 9, 2021. ISSN 2296-6463. URL <https://www.frontiersin.org/articles/10.3389/feart.2021.707274>.
- Hongxiong Xu and Dajun Zhao. Effect of the Vertical Diffusion of Moisture in the Planetary Boundary Layer on an Idealized Tropical Cyclone. *Advances in Atmospheric Sciences*, 38(11):1889–1904, 2021. ISSN 1861-9533. doi: 10.1007/s00376-021-1016-z.

John Xun Yang, Yong-Keun Lee, Christopher Grassotti, Kevin Garrett, Quanhua Liu, William Blackwell, R. Vincent Leslie, Tom Greenwald, Ralf Bennartz, and Scott Braun. Atmospheric humidity and temperature sounding from the CubeSat TROPICS mission: Early performance evaluation with MiRS. *Remote Sensing of Environment*, 287:113479, 2023. ISSN 0034-4257. doi: 10.1016/j.rse.2023.113479.

Song Yang, Richard Bankert, and Joshua Cossuth. Tropical Cyclone Climatology from Satellite Passive Microwave Measurements. *Remote Sensing*, 12(21):3610, 2020. ISSN 2072-4292. doi: 10.3390/rs12213610.

Jianjun Yin. Rapid Decadal Acceleration of Sea Level Rise along the U.S. East and Gulf Coasts during 2010–22 and Its Impact on Hurricane-Induced Storm Surge. *Journal of Climate*, 36(13): 4511–4529, 2023. ISSN 0894-8755, 1520-0442. doi: 10.1175/JCLI-D-22-0670.1.

Rachel Young and Solomon Hsiang. Mortality caused by tropical cyclones in the United States. *Nature*, 635(8037):121–128, 2024. ISSN 1476-4687. doi: 10.1038/s41586-024-07945-5.

Cheng-Ku Yu and Chia-Lun Tsai. Structural and Surface Features of Arc-Shaped Radar Echoes along an Outer Tropical Cyclone Rainband. *Journal of the Atmospheric Sciences*, 70(1):56–72, 2013. ISSN 0022-4928, 1520-0469. doi: 10.1175/JAS-D-12-090.1. publisher: American Meteorological Society section: Journal of the Atmospheric Sciences.

Cheng-Ku Yu, Che-Yu Lin, Lin-Wen Cheng, Jhang-Shuo Luo, Chun-Chieh Wu, and Ying Chen. The degree of prevalence of similarity between outer tropical cyclone rainbands and squall lines. *Scientific Reports*, 8(1):8247, 2018. ISSN 2045-2322. doi: 10.1038/s41598-018-26553-8. number: 1.

Cheng-Ku Yu, Che-Yu Lin, and Jhang-Shuo Luo. Tracking a Long-Lasting Outer Tropical Cyclone Rainband: Origin and Convective Transformation. *Journal of the Atmospheric Sciences*, 76(10): 3267–3283, 2019. ISSN 0022-4928, 1520-0469. doi: 10.1175/JAS-D-19-0126.1.

Sandra E. Yuter and Robert A. Houze. Three-Dimensional Kinematic and Microphysical Evolution of Florida Cumulonimbus. Part I: Spatial Distribution of Updrafts, Downdrafts, and Precipitation. *Monthly Weather Review*, 1995. ISSN 1520-0493. URL https://journals.ametsoc.org/view/journals/mwre/123/7/1520-0493_1995_123_1921_tdkame_2_0_co_2.xml. section: Monthly Weather Review.

Jonathan Zawislak and Edward J. Zipser. Analysis of the Thermodynamic Properties of Developing and Nondeveloping Tropical Disturbances Using a Comprehensive Dropsonde Dataset. *Monthly Weather Review*, 142(3):1250–1264, 2014. ISSN 1520-0493, 0027-0644. doi: 10.1175/MWR-D-13-00253.1.

Jonathan Zawislak, Haiyan Jiang, George R. Alvey, Edward J. Zipser, Robert F. Rogers, Jun A. Zhang, and Stephanie N. Stevenson. Observations of the Structure and Evolution of Hurricane Edouard (2014) during Intensity Change. Part I: Relationship between the Thermodynamic Structure and Precipitation. *Monthly Weather Review*, 144(9):3333–3354, 2016. ISSN 1520-0493, 0027-0644. doi: 10.1175/MWR-D-16-0018.1.

Jonathan Zawislak, Robert F. Rogers, Sim D. Aberson, Ghassan J. Alaka, George R. Alvey, Altug Aksoy, Lisa Bucci, Joseph Cione, Neal Dorst, Jason Dunion, Michael Fischer, John Gamache,

Sundararaman Gopalakrishnan, Andrew Hazelton, Heather M. Holbach, John Kaplan, Hua Leighton, Frank Marks, Shirley T. Murillo, Paul Reasor, Kelly Ryan, Kathryn Sellwood, Jason A. Sippel, and Jun A. Zhang. Accomplishments of NOAA's Airborne Hurricane Field Program and a Broader Future Approach to Forecast Improvement. *Bulletin of the American Meteorological Society*, 103(2):E311–E338, 2022. ISSN 0003-0007, 1520-0477. doi: 10.1175/BAMS-D-20-0174.1.

Alice R Zhai and Jonathan H Jiang. Dependence of US hurricane economic loss on maximum wind speed and storm size. *Environmental Research Letters*, 9(6):064019, 2014. ISSN 1748-9326. doi: 10.1088/1748-9326/9/6/064019. publisher: IOP Publishing.

Biao Zhang and W. Perrie. Remote Sensing of Tropical Cyclones by Spaceborne Synthetic Aperture Radar: Past, Present and Future. *IEEE Geoscience and Remote Sensing Magazine*, 2024.

Chang-Jiang Zhang, Yu Wang, Xiao-Qin Lu, and Feng-Yuan Sun. Rapid Weakening Tropical Cyclone Intensity Estimation Based on Deep Learning Using Infrared Satellite Images and Reanalysis Data. *IEEE Journal of Selected Topics in Applied Earth Observations and Remote Sensing*, pages 1–16, 2024. ISSN 2151-1535. doi: 10.1109/JSTARS.2024.3465829.

Fuqing Zhang, Yonghui Weng, John F. Gamache, and Frank D. Marks. Performance of convection-permitting hurricane initialization and prediction during 2008–2010 with ensemble data assimilation of inner-core airborne Doppler radar observations. *Geophysical Research Letters*, 38(15), 2011a. ISSN 1944-8007. doi: 10.1029/2011GL048469. URL <https://onlinelibrary.wiley.com/doi/10.1029/2011GL048469>.

Jun A. Zhang and Robert F. Rogers. Effects of parameterized boundary layer structure on hurricane rapid intensification in shear. *Monthly Weather Review*, 147(3):853–871, 2019. ISSN 1520-0493, 0027-0644. doi: 10.1175/MWR-D-18-0010.1. URL <https://journals.ametsoc.org/view/journals/mwre/147/3/mwr-d-18-0010.1.xml>. Publisher: American Meteorological Society Section: Monthly Weather Review.

Jun A. Zhang, William M. Drennan, Peter G. Black, and Jeffrey R. French. Turbulence Structure of the Hurricane Boundary Layer between the Outer Rainbands. *Journal of the Atmospheric Sciences*, 66(8):2455–2467, 2009. ISSN 0022-4928, 1520-0469. doi: 10.1175/2009JAS2954.1. publisher: American Meteorological Society section: Journal of the Atmospheric Sciences.

Jun A. Zhang, Robert F. Rogers, David S. Nolan, and Frank D. Marks. On the Characteristic Height Scales of the Hurricane Boundary Layer. *Monthly Weather Review*, 139(8):2523–2535, aug 1 2011b. ISSN 1520-0493, 0027-0644. doi: 10.1175/MWR-D-10-05017.1. publisher: American Meteorological Society section: Monthly Weather Review.

Jun A. Zhang, Sundararaman Gopalakrishnan, Frank D. Marks, Robert F. Rogers, and Vijay Tallapragada. A Developmental Framework for Improving Hurricane Model Physical Parameterizations Using Aircraft Observations. *Tropical Cyclone Research and Review*, 1(4):419–429, 2012. ISSN 2225-6032. doi: 10.6057/2012TCRR04.01.

Jun A. Zhang, Robert F. Rogers, Paul D. Reasor, Eric W. Uhlhorn, and Frank D. Marks. Asymmetric Hurricane Boundary Layer Structure from Dropsonde Composites in Relation to the Environmental Vertical Wind Shear. *Monthly Weather Review*, 141(11):3968–3984, 2013. ISSN 1520-0493, 0027-0644. doi: 10.1175/MWR-D-12-00335.1.

Jun A. Zhang, David S. Nolan, Robert F. Rogers, and Vijay Tallapragada. Evaluating the Impact of Improvements in the Boundary Layer Parameterization on Hurricane Intensity and Structure Forecasts in HWRF. *Monthly Weather Review*, 2015. doi: 10.1175/MWR-D-14-00339.1. URL <https://journals.ametsoc.org/view/journals/mwre/143/8/mwr-d-14-00339.1.xml>.

Jun A. Zhang, Joseph J. Cione, Evan A. Kalina, Eric W. Uhlhorn, Terry Hock, and Jeffrey A. Smith. Observations of infrared sea surface temperature and air-sea interaction in hurricane edouard (2014) using GPS dropsondes. *Journal of Atmospheric and Oceanic Technology*, 34(6):1333–1349, 2017a. ISSN 0739-0572, 1520-0426. doi: 10.1175/JTECH-D-16-0211.1. URL <https://journals.ametsoc.org/view/journals/atot/34/6/jtech-d-16-0211.1.xml>. Publisher: American Meteorological Society Section: Journal of Atmospheric and Oceanic Technology.

Jun A. Zhang, Robert F. Rogers, and Vijay Tallapragada. Impact of Parameterized Boundary Layer Structure on Tropical Cyclone Rapid Intensification Forecasts in HWRF. *Monthly Weather Review*, 145(4):1413–1426, 2017b. ISSN 1520-0493, 0027-0644. doi: 10.1175/MWR-D-16-0129.1. publisher: American Meteorological Society section: Monthly Weather Review.

Jun A. Zhang, Robert Atlas, G. David Emmitt, Lisa Bucci, and Kelly Ryan. Airborne Doppler Wind Lidar Observations of the Tropical Cyclone Boundary Layer. *Remote Sensing*, 10(6):825, 2018. doi: 10.3390/rs10060825. number: 6 publisher: Multidisciplinary Digital Publishing Institute.

Jun A. Zhang, Evan A. Kalina, Mrinal K. Biswas, Robert F. Rogers, Ping Zhu, and Frank D. Marks. A Review and Evaluation of Planetary Boundary Layer Parameterizations in Hurricane Weather Research and Forecasting Model Using Idealized Simulations and Observations. *Atmosphere*, 11(10):1091, 2020. ISSN 2073-4433. doi: 10.3390/atmos11101091.

Jun A. Zhang, Robert F. Rogers, Paul D. Reasor, and John Gamache. The Mean Kinematic Structure of the Tropical Cyclone Boundary Layer and Its Relationship to Intensity Change. *Monthly Weather Review*, 151(1):63–84, 2022a. ISSN 1520-0493, 0027-0644. doi: 10.1175/MWR-D-21-0335.1. publisher: American Meteorological Society section: Monthly Weather Review.

Jun A. Zhang, Robert F. Rogers, Paul D. Reasor, and John Gamache. The mean kinematic structure of the tropical cyclone boundary layer and its relationship to intensity change. *Monthly Weather Review*, 151(1):63–84, 2022b. ISSN 1520-0493, 0027-0644. doi: 10.1175/MWR-D-21-0335.1. URL <https://journals.ametsoc.org/view/journals/mwre/151/1/MWR-D-21-0335.1.xml>. Publisher: American Meteorological Society Section: Monthly Weather Review.

Zhan Zhang, Vijay Tallapragada, Chanh Kieu, Samuel Trahan, and Weiguo Wang. Hwrf Based Ensemble Prediction System Using Perturbations from GEFS and Stochastic Convective Trigger Function. *Tropical Cyclone Research and Review*, 3(3):145–161, 2014. ISSN 2225-6032. doi: 10.6057/2014TCRR03.02.

Zhan Zhang, Weiguo Wang, James Doyle, Jon Moskaitis, Will Komaromi, Julian Heming, Linus Magnusson, John P. Cangialosi, Levi Cowan, Michael Brennan, Suhong Ma, Ananda Kumar Das, Takuya Hosomi, Peter Clegg, Thomas Birchard, John Knaff, John Kaplan, Mrutyunjay Mohapatra, Monica Sharma, Ikegami Masaaki, Liguang Wu, and Eric Blake. A review

of recent advances (2018-2021) on tropical cyclone intensity change from operational perspectives, Part 1: Dynamical model guidance. Tropical Cyclone Research and Review, 2023. ISSN 2225-6032. doi: 10.1016/j.tcrr.2023.05.004. URL <https://www.sciencedirect.com/science/article/pii/S2225603223000152>. [Online; accessed 2023-05-16].

Gang Zheng, Han Jiang, Liang Wu, Xiaofeng Li, Lizhang Zhou, Qiaoyan Wu, Peng Chen, and Lin Ren. Rainband-Occurrence Probability in Northern Hemisphere Tropical Cyclones by Synthetic Aperture Radar Imagery. Geophysical Research Letters, 51(10):e2023GL107555, 2024. ISSN 1944-8007. doi: 10.1029/2023GL107555. URL <https://onlinelibrary.wiley.com/doi/pdf/10.1029/2023GL107555>.

Xingyang Zhou, Liguang Wu, Qingyuan Liu, and Yan Zheng. Influence of Low-Level, High-Entropy Air in the Eye on Tropical Cyclone Intensity: A Trajectory Analysis. Journal of the Meteorological Society of Japan. Ser. II, 98(6):1231–1243, 2020. ISSN 0026-1165, 2186-9057. doi: 10.2151/jmsj.2020-063.

Yao Zhou and Corene J. Matyas. Spatial characteristics of storm-total rainfall swaths associated with tropical cyclones over the Eastern United States. International Journal of Climatology, 37(S1):557–569, 2017. ISSN 1097-0088. doi: 10.1002/joc.5021. eprint: <https://onlinelibrary.wiley.com/doi/pdf/10.1002/joc.5021>.

Appendix A

SUPPLEMENTAL INFORMATION FOR CHAPTER 2

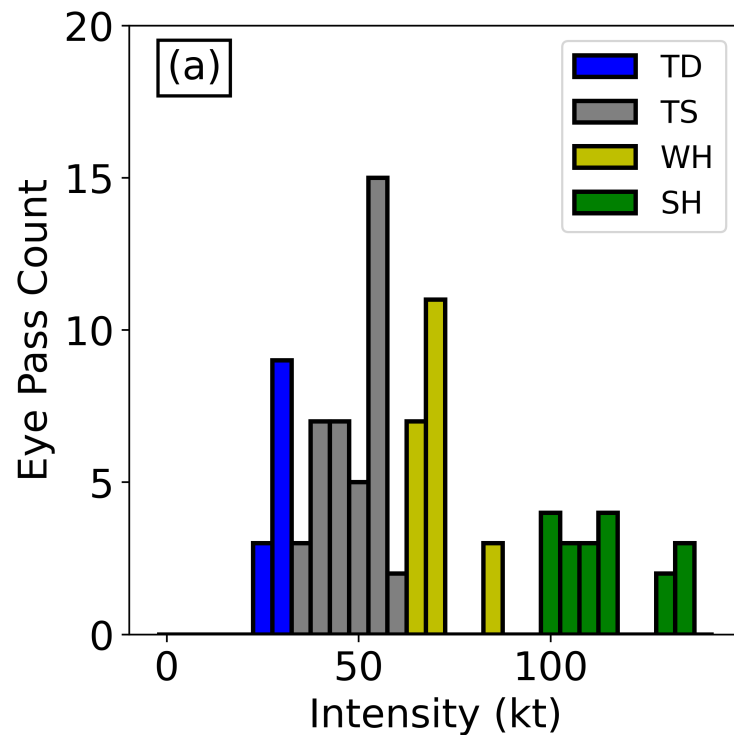


Figure A.1: Tropical cyclone (TC) intensity distributions across all compact Raman lidar (CRL) eye passes. The four intensity categories specified above are used to divide CRL cloud height data for Figures 3 and 4. 91 total eye passes were conducted using the CRL.

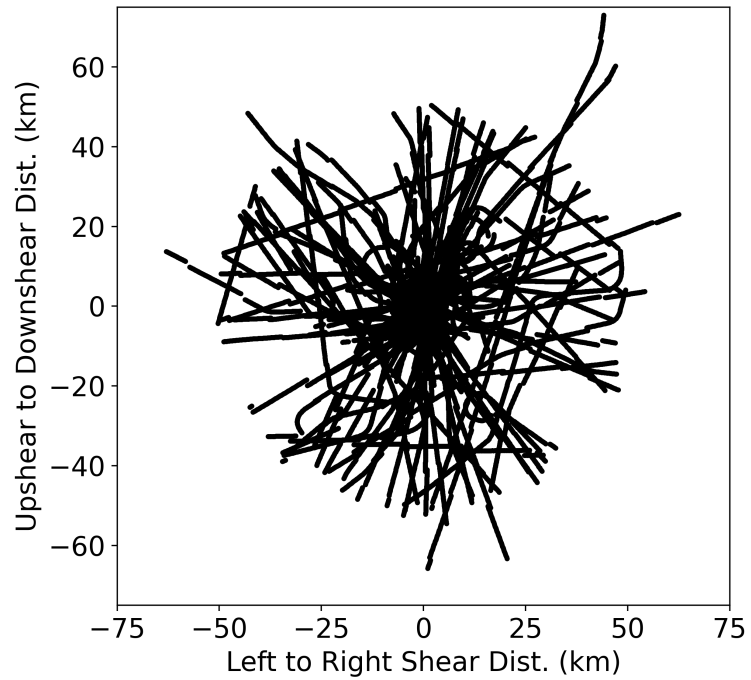


Figure A.2: Distribution of CRL eye passes in a shear relative framework. Note that the eye is defined differently for weak versus strong systems; see the main article text for TC eye definitions. The ample amount of eye passes ensures that there is adequate spatial coverage for statistical tests.

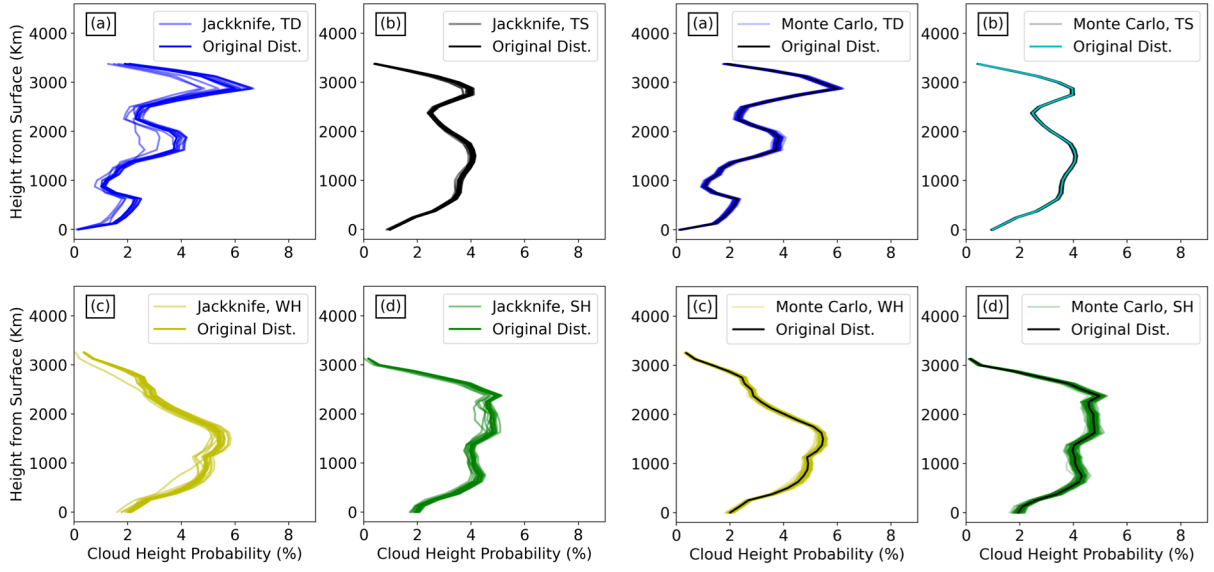


Figure A.3: Error analysis using Jackknife (left) and Monte Carlo (right) tests for cloud height distributions for each TC intensity category. The Jackknife test checks the importance of individual eye passes by removing one eye pass and recreating the distribution, for every eye pass. The Monte Carlo test randomly samples half the cloud heights and recalculates the distribution 100 times. Both statistical tests show little variation from the original distribution, suggesting that the cloud height probability distributions are robust. See main text for additional analysis.

Storm Name	Date	Number of CRL Passes	Intensity (kt)	Intensity Change (kt/24h)	Shear Magnitude (m/s)	Shear Direction (degrees)
Fred	12 Aug 21	5	30	5	18.7	109
Fred	13 Aug 21	2	30	0	17.9	97
Grace	16 Aug 21	2	30	5	16	154
Grace	17 Aug 21	3	45	15	10.7	142
Grace	18 Aug 21	3	70	-5	10.5	135
Grace	19 Aug 21	3	55	15	8.1	169
Henri	20 Aug 21	2	60	10	12.8	179
Henri	21 Aug 21	3	65	-10	6.0	240
Ida	27 Aug 21	4	70	15	11.5	61
Ida	28 Aug 21	1	85	60	12.5	105
Ida	29 Aug 21	1	130	-50	11.2	127
Sam	25 Sept 21	1	130	45	8.6	65
Sam	26 Sept 21	3	135	-25	9.0	64
Sam	27 Sept 21	3	105	10	8.5	44
Sam	29 Sept 21	4	115	10	10.3	57
All 2021 Passes:		40				
Earl	1 Sept 22	3	25	NA	NA	NA
Earl	3 Sept 22	5	40	5	13.9	67
Earl	4 Sept 22	1	45	5	17.3	75
Earl	5 Sept 22	4	55	10	19.7	80
Earl	6 Sept 22	3	55	10	27.3	78
Earl	8 Sept 22	2	85	-10	9.4	108
Fiona	16 Sept 22	3	50	0	13.2	103
Fiona	17 Sept 22	2	50	0	15.4	94
Fiona	18 Sept 22	5	55	25	19.1	80
Fiona	20 Sept 22	4	100	15	22.6	97
Ian	24 Sept 22	3	35	5	11.8	182
Ian	25 Sept 22	2	40	10	10.6	151
Ian	26 Sept 22	4	70	35	6.5	88
Ian	27 Sept 22	3	110	20	17.0	32
Julia	7 Oct 22	3	45	20	11.0	122
Julia	8 Oct 22	4	65	10	5.7	194
All 2022 Passes		51				
Total Passes		91				

Table A.1: A list of all CRL eye passes from TC aircraft missions from 2021 to 2022. The TC name and sampling date, along with the number of eye passes, TC intensity, intensification rate, and shear, are provided for all flights.

Appendix B

SUPPLEMENTAL INFORMATION FOR CHAPTER 3

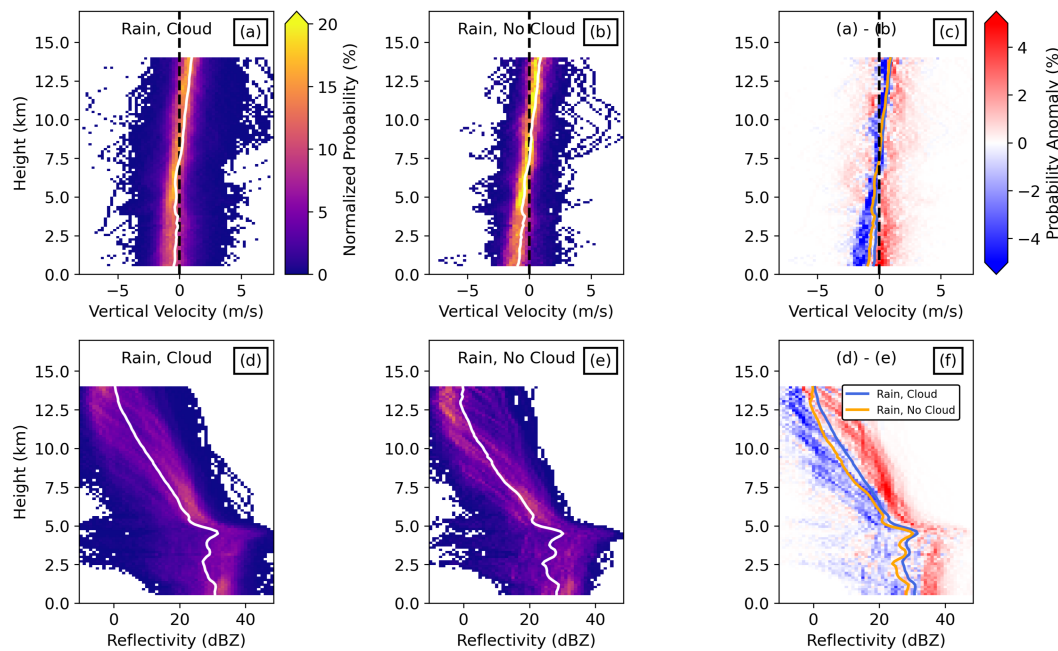


Figure B.1: As in Figure 4, but the stratiform rain classification is split into two categories: stratiform rain with a shallow cloud below, and stratiform rain with no shallow cloud below.

TC Name	Flight	Intensity (kt)	Intensity Change (kt/Day, -12h to 12h)	Surface Pressure (hPa)	Intensity Change (hPa/Day, -12h to 12h)	Shear Magnitude (kt)	Shear Direction (Degrees)	Number of Legs	Hurricane Strength Legs	Shear Quadrants Used
Fred	20210812H1	30	4	1010	1	19	109	6	0	
Fred	20210812H2	34	1	1010	0	18	93	4	0	
Fred	20210813H1	31		1010		19	98	4	0	
Grace	20210816H1	34	5	1008	-5	16	153	4	0	
Grace	20210817H1	45	15	1005	-6	11	142	6	0	
Grace	20210818H1	70	-2	988	-1	10	136	6	6	1 DR, 1 DL, 2 UL, 1 UR
Grace	20210819H1	53	11	995	-9	9	171	6	0	
Henri	20210820H1	60	9	993	-4	13	181	6	0	
Henri	20210821H2	65	-10	988	-5	6	240	6	6	1 DR, 1 DL, 2 UL, 1 UR
Ida	20210827H1	70	15	989	-10	12	62	8	8	1 DR, 1 DL, 2 UL, 2 UR
Ida	20210828H1	85	52	972	-47	12	107	2	2	1 DL, 1 UR
Ida	20210829H1	118	-63	936	40	12	121	2	2	1 DL, 1 UR
Sam	20210925H1	127	27	944	-23	9	69	1	1	1 UL
Sam	20210926H1	130	-25	940	16	9	64	6	6	1 DR, 1 DL, 2 UL, 1 UR
Sam	20210927H1	105	9	955	-2	8	45	5	5	2 DL, 1 UL, 1 UR
Sam	20210929H2	125	10	940	-15	10	58	7	7	2 DR, 2 DL, 2 UL, 1 UR
Earl	20220901H1	35		1006		9	35	6	0	
Earl	20220903H1	40	6	1002	-6	14	65	10	0	
Earl	20220904H1	45	5	999	-1	17	75	2	0	
Earl	20220905H1	55	10	998	-6	20	80	6	0	
Earl	20220906H1	55	10	996	-6	27	78	8	0	
Earl	20220908H1	85	-10	962	-6	9	108	5	5	1 DR, 1 DL, 1 UL, 1 UR
Fiona	20220916H1	45	0	1005	-3	13	102	6	0	
Fiona	20220917H1	50	1	1000	-5	16	93	4	0	
Fiona	20220918H1	65	25	990	-13	19	80	8	8	3 DR, 2 DL, 1 UL, 2 UR
Fiona	20220920H1	100	15	961	-23	22	97	8	8	1 DR, 4 DL, 1 UL, 2 UR
Ian	20220924H1	39	6	1003	-2	11	186	2	0	
Ian	20220925H1	40	10	1003	-12	11	151	4	0	
Ian	20220926H1	69	36	982	-26	6	88	6	6	1 DR, 1 DL, 1 UL, 1 UR
Ian	20220927H1	100	21	962	-19	17	32	6	6	3 DL, 1 UL
Julia	20221007H1	45	20	999	-8	11	125	6	0	
Julia	20221008H1	65	11	989	-10	6	192	4	4	1 DL, 3 UR

Table B.1: A list of all flight legs with CRL data and their associated vortex and environmental information used in this analysis.